This is to certify that the

dissertation entitled

Electrical and Magneto-resistivity Measurements on Amorphous CuTi Alloys at Low Temperatures

presented by

Renyong Fan

has been accepted towards fulfillment
of the requirements for

Ph.D degree in Physics

William P. Pratt
Major professor

Date Oct. 7, 1992

ELECTRICAL AND MAGNETO-RESISTIVITY MEASUREMENTS ON AMORPHOUS CuTi ALLOYS AT LOW TEMPERATURES

By

Renyong Fan

A DISSERTATION

Submitted to
Michigan State University
in partial fulfillment of the requirements
for the degree of

DOCTOR OF PHILOSOPHY

Department of Physics and Astronomy

1992

ABSTRACT

ELECTRICAL AND MAGNETO-RESISTIVITY MEASUREMENTS ON AMORPHOUS CuTi ALLOYS AT LOW TEMPERATURES

By

Renyong Fan

The anomalous transport properties of highly disordered metallic glasses, which require corrections to the classical Boltzmann theory, are due to quantum interference effects of the scattered electron waves. These corrections provide new contributions to the resistivity: "weak localization" and "electron-electron interaction". To study these quantum interference effects, we have made the highest-precision measurements, so far, of the resistances of the amorphous $Cu_{50}Ti_{50}$ and $Cu_{60}Ti_{40}$ ribbons at much lower temperatures than before (15mK$< T <$6K) and in small magnetic fields (0T$<$ B $<$0.2T). To measure the resistance and temperature accurately, we developed a novel method: measuring the resistance perpendicular to the ribbons with potassium as the non-superconducting glue between the CuTi ribbons and two Cu electrodes in order to make excellent electrical and thermal contact. With this method, we were able to measure the resistances with a relative precision of $\Delta\rho/\rho = 10^{-7} - 10^{-8}$ and temperatures reliably down to 15mK with an error of less than 1mK.

The zero field resistances and magnetoresistances were analyzed using weak localization theories that include the Zeeman splitting and electron-electron interaction theories. Possible background contributions from the K layers, the Cu electrodes, and their boundaries are quantified in the analysis. In zero field, these background contributions were negligible for $T < 3$K. At zero magnetic field and $T < 0.15$K, we found that electron-electron interaction dominates the resistance, while weak localization makes a nontrivial contribution to the resistance for $T > 0.15$K. In contrast, at the lowest temperatures, the magnetoresistances were dominated by weak localiza-

tion with Zeeman splitting and Maki-Thompson superconducting fluctuations. For higher magnetic fields and lowest temperatures ($B/T > 1$ T/K), we find discrepancies between our data and the theoretical calculations.

We found that most of the parameters of the theoretical fits to the data were similar for both $Cu_{50}Ti_{50}$ and $Cu_{60}Ti_{40}$ alloys. The two important exceptions were the inelastic and spin-orbit lifetimes: their zero-field values were about an order of magnitude smaller than those from the magnetoresistances. Also the inelastic lifetimes tend to saturate for $T < 0.1$K in non-zero magnetic fields.

Finally, we were also able to estimate the expected superconducting transition temperatures of both $Cu_{50}Ti_{50}$ and $Cu_{60}Ti_{40}$ alloys: less than 15mK and 5mK, respectively.

Our novel technique can, in principle, be used to make high precision resistance measurements down to 15mK on any ribbon or film-like high resistivity metal.

DEDICATION

This thesis is dedicated to my mother, mother in law, especially to my wife, Zhenli, and my son, Dan, whose assistance and encouragement were greatly appreciated.

ACKNOWLEDGEMENTS

My sincere thanks go to Dr. William P. Pratt, Jr. for his supervision and invaluable aid and suggestions throughout the writing of the thesis. I am very grateful for his help during many late-nights measurements.

I would also like to express my thanks to Dr. Dennis Greig for his cooperation and advice. I wish to thank Dr. Peter A. Schroeder for his help in taking data. Special thanks to Dr. Reza Loloee for his help in the ion milling and sputtering, and to Thomas Palazzolo, Jim Muns, and Tom Hudson for their help in the construction of the apparatus. I wish to thank Dr. Zhao Liang and Yang Qing for their friendship and encouragement.

I acknowledge the financial support of the National Science Foundation.

Contents

3 Experimental Techniques 29

List of Tables

List of Figures

Chapter 1

Introduction

Disordered metals and alloys have the following unusual transport properties:

(1) The residual resistivity ρ is much higher than in the crystalline phase.

(2) The temperature coefficients of the resistivity are very small and usually positive for $\rho < 150\mu\Omega\text{cm}$ and negative for $\rho > 150\mu\Omega\text{cm}$.

(3) Magnetoresistance may be positive or negative, depending on chemical composition of a material.

The classical Boltzmann theory has been very successful in explaining the transport properties of the crystalline metals. However, this theory failed when it was applied to disordered conductors. Obviously, the structural difference between the two systems is a major reason. Why does the structure of the system strongly affect its transport properties? In 1958, Anderson [And 58] pointed out that, in a strongly disordered system, an electron wave function is localized and therefore the system becomes an insulator. For a weakly disordered system, Abrahams *et al.* [Abr 79] first introduced the concept of quantum interference effects that become important if the electron mean free path is of the order of inter-atomic distances. This interference effect in which electron-electron interactions are ignored is called weak localization (WL). In addition, quantum interference causes an enhanced electron-electron interaction (EEI) that also makes an anomalous contribution to the resistivity. There have been a number of review articles [Alt 85, Fuk 85, Ber 84] which deal with WL and EEI using the diagrammatic Green's function method. Bergmann [Ber 82, Ber 83, Ber 87] has presented excellent reviews with very clear physical pictures of these quantum interference effects.

Since quantum interference changes the scattering probability of electrons, which is proportional to the resistivity, it is natural to calculate and measure the resistance of the system in order to study these quantum interference effects.

Two dimensional disordered systems have been under extensive study since the quantum corrections to the resistivities are relatively large and thus easier to measure. In contrast, much less work has been done in three dimensional systems since the quantum corrections produce a temperature dependence of only $\Delta\rho/\rho \sim 10^{-5}$ for a temperature change of 0.1K at $T \leq 1$K, which can be very difficult to measure accurately.

Among the three dimensional amorphous systems that have been studied, CuTi alloy is one of the most extensively studied systems because of its stable structure and properties. Most experiments were done at low temperatures where weak localization and electron-electron interaction contributions are most significant.

Three major groups have studied the CuTi alloys extensively. The English group (Greig, Howson, Hickey et al.) [Hic 86, Hic 87, How 86, How 88] studied a series of Cu_xTi_{1-x} ribbons at temperatures between about 0.1K and 300K and in magnetic fields up to 30 Tesla. The relative precision of their resistance measurement was about 10^{-5}. Schulte et al. (German group) [Sch 86, Sch 90] took their data at $T = 1.5-60$K and for $B < 40$T with about the same relative precision. Lindqvist and Rapp[Lin 88] is the only group (Swedish) that attempted to make measurements down to 20mK with similar precision and $B < 5$T. However their thermometry was not good for $T < 0.3$K because of poor heat conduction between their samples and refrigerator.

Although these three groups did obtain very useful data, further work is needed for the following reasons:

As this thesis will show, much lower temperature and magnetic fields are required in order to clearly disentangle the WL and EEI contributions to the resistivity. Relative precision of about 10^{-5} is not high enough for useful measurements at very low temperatures and with small magnetic fields. As clearly observed by Lindqvist and Rapp, use of an insulator as thermal contact agent between the samples and the refrigerator leads to unreliable thermometry below about 0.3K.

To overcome these problems, we have developed a novel method for measuring the resistance of the amorphous $Cu_{50}Ti_{50}$ and $Cu_{60}Ti_{40}$ ribbons:

(1) By using the high precision current comparator with a superconducting quantum interference device (SQUID) as a null detector, we could measure the resistance to a relative precision of about $10^{-7} - 10^{-8}$ for $B < 0.2$T.

(2) We measure the resistances of CuTi alloys by applying a current perpendicular to the ribbons. We use potassium as a non-superconducting glue between the ribbons and the refrigerator, so that excellent thermal contact is obtained at all temperatures. The error in the temperature is much less than 1mK at $T \approx 15$mK.

(3) With the above improvements, we have obtained very precise measurements of the resistances of the CuTi alloys at very low temperatures (15mK< T <6K) and small magnetic fields (0T< B <0.2T).

In this thesis, we are going to present our zero field resistance and magnetoresistance measurements, compare our results with those of other workers, and analyze the data using appropriate theoretical models. Since our new measurements show that both $Cu_{50}Ti_{50}$ and $Cu_{60}Ti_{40}$ are superconductors with transition temperatures below 15mK and 5mK, respectively, we will also briefly discuss the paraconductivity due to superconducting fluctuations when T is close to, but above, the transition temperature (T_c).

Chapter 2

Quantum Interference Theories

In this chapter, we will describe the quantum interference effect (QIE) of electrons in disordered three dimensional systems. A brief description of the classical Boltzmann transport theory will also be given.

2.1 Classical Transport Theories

2.1.1 Definition of Resistivity

When an electrical field is applied to a metal, a current proportional to the electrical field will flow.

$$\mathbf{J} = \sigma \mathbf{E} \ . \tag{2.1}$$

In general, the conductivity σ is a tensor, but for a metal with cubic symmetry, it reduces to a diagonal tensor in which all the elements along the diagonal are equal. Because of this reduction, σ can be represented as a scalar. The electrical resistivity ρ, defined as the inverse of the conductivity, is given by

$$\rho = \frac{1}{\sigma} = \frac{|\mathbf{E}|}{|\mathbf{J}|} \ . \tag{2.2}$$

If we also apply a magnetic field to a metal, the resistivity, given by the above formula, is called magnetoresistivity.

2.1.2 Electrical Resistivity

In Boltzmann transport theory, an electron is described as a quasiparticle with wave vector **k** and energy $E = \hbar^2 k^2/2m^*$. Electrons are scattered by impurities and lattice defects. Between collisions, the electrons are assumed to move in a classical trajectory. For $k_F l \gg 1$, where l is the electron mean free path, the interferences between electron waves can be neglected. In a simple metal with only s or p electrons, the conductivity or resistivity due to electron scattering is given by

$$\sigma = \frac{ne^2\tau}{m^*} \ , \tag{2.3}$$

$$\rho = \frac{1}{\sigma} = \frac{m^*}{ne^2\tau} \ , \tag{2.4}$$

where m^* is the electron effective mass, n is the electron number density, e is the electron charge, and τ is the relaxation time, which is inversely proportional to the scattering probability of the electrons. If there are more than one scattering mechanisms such as electron-impurity, electron-phonon, and electron-electron scattering, then according to Matthiessen's rule [Bla 68], the total resistivity can be written as a sum of the different scattering terms, that is

$$\rho = \rho_o + \rho_{ee} + \rho_{ep} \ , \tag{2.5}$$

where ρ_o is the temperature independent resistivity due to electron impurity or defect scattering. ρ_{ee} and ρ_{ep} are due to electron electron and electron phonon scattering, respectively. At low temperature, for a simple metal, ρ_{ee} is proportional to T^2 [Zim 60], and ρ_{ep} has a stronger temperature dependence. There are two kinds of electron-phonon scattering, which are called normal and Umklapp processes. Theoretically, the resistivities are proportional to T^5 for the normal process and $\exp(-\Theta/T)$ for the Umklapp process [Zim 60]. The resistivity at low temperature for a typical simple metal is shown in Figure 2.1.

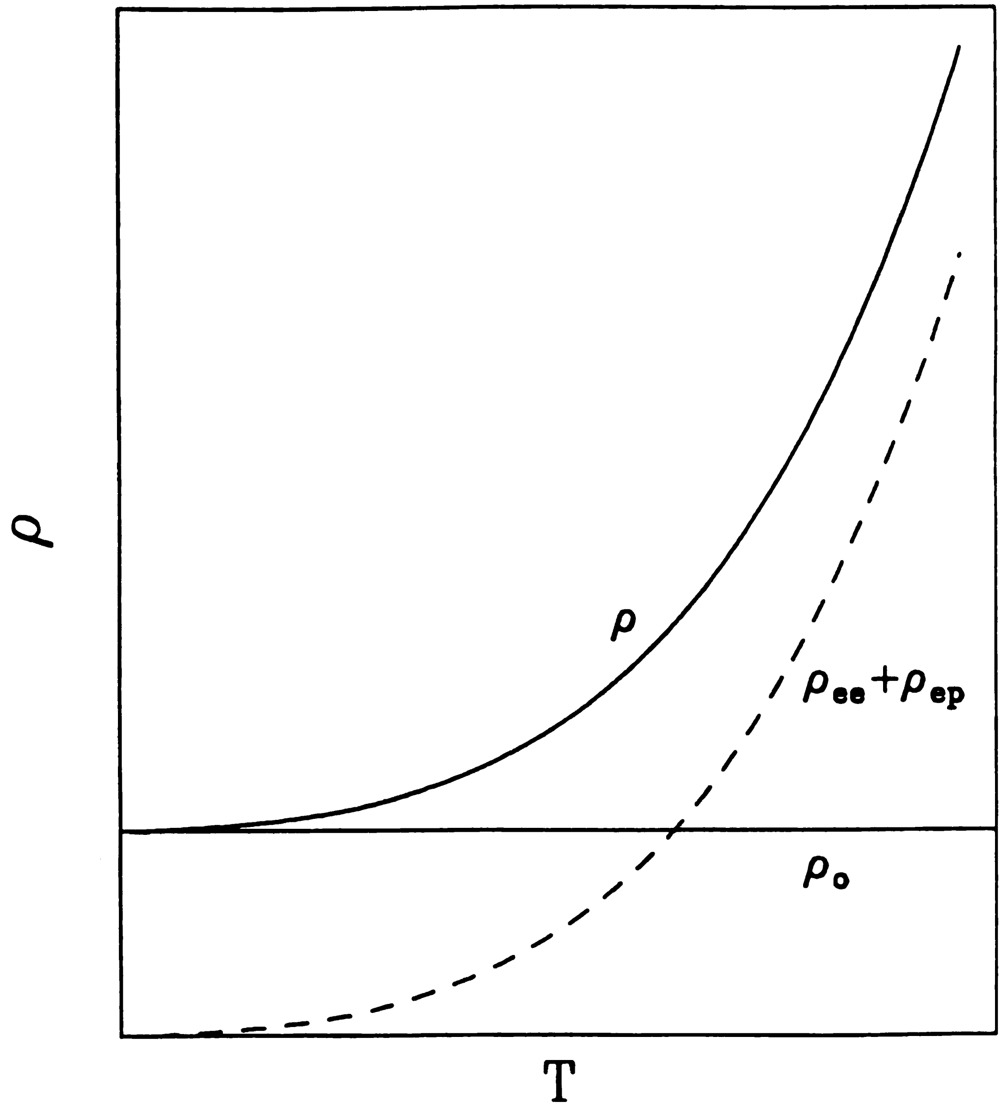

Figure 2.1: Low temperature resistivity for a typical simple metal

2.1.3 Magnetoresistivity

When we apply a magnetic field, because of the Lorentz forces on electrons, the electrons will deflect and travel a longer path before arriving at a destination, so one would naively expect the resistivity to always rise. But the theory is not that simple. Details have been given in many texts [Zim 60, Bla 68]. For a simple metal with a spherical Fermi surface and with the magnetic field parallel to the current, the Lorentz force, $\mathbf{F}=q\mathbf{V}\times\mathbf{B}$, is zero. So there is no magnetoresistivity. For the magnetic field perpendicular to the current, electrons will be diverted from their paths along the specimen and accumulate along the specimen sides (Hall Effect). Thus the charges created on the specimen sides will exert forces on the moving electrons and cancel the Lorentz forces. Therefore the electrons will continue to travel down the specimen along the original paths, and the resistivity is not affected. However for a metal with two or more electron energy bands, since the electrons in these two bands have different effective masses, their drift speeds in an electrical field will be different. Thus the Lorentz forces on the two carrier types differ and the electrical forces due to the Hall electrical field will not cancel the Lorentz forces exactly. Therefore a transverse magnetoresistivity can exist [Bla 68]. Ziman showed that this magnetoresistivity is proportional to B^2 for a small magnetic field. But for the parallel magnetic field, experiments show that the (longitudinal) magnetoresistances are of the same order as the transverse magnetoresistances in many metals. Theorists have found that this longitudinal magnetoresistivity is due to non-spherical Fermi surfaces. For K and Cu, a B^2 law is approximately obeyed at low magnetic fields [Pip 89].

2.2 Quantum Interference Effects

For the amorphous systems such as liquid metals, since $k_F l \gg 1$ (e.g. $k_F l \sim 100$ for liquid potassium), the Boltzmann assumption is still valid. With some modifications, their transport properties have been explained by the Ziman liquid model [How 88]. However for systems such as metallic glasses, the conventional theory is not adequate due to the shortness of the electron mean free path.

The metallic glasses show some unusual properties:

(1) Resistivity is very high at all temperatures, typically on the order of 100$\mu\Omega$cm to 300$\mu\Omega$cm.

(2) The temperature dependent resistivity is very small, typically on the order of a few percent in a temperature range from 4.2K to 300K. When $\rho < 150\mu\Omega$cm, the temperature coefficients are usually positive. For $\rho > 150\mu\Omega$cm, they are often negative at low temperatures.

(3) The positive and negative magnetoresistances are observed depending on the materials chosen. They are usually proportional to $\sqrt{B}$ at high magnetic fields.

The conventional Boltzmann theory failed to explain these properties. The basic reason is that the Boltzmann assumption is invalid. Electrons after scattering do not move in classical trajectories, but travel like waves. So quantum interference between the scattered electrons must be considered.

2.2.1 Weak Localization

In this section, we consider only non interacting electrons. In a highly disordered metal, an electron is scattered at almost every lattice site. Its mean free path is of the order of an atomic distance which is not very large in comparison to its wave length. Thus the quantum interference of scattering amplitudes for different scattering sites become important.

Now let us consider an electron in a conductor, which can move along paths 1, 2, 3, and 4 from A to B as shown in the top part of Figure 2.2 [Alt 85]. The total transferring probability w for the electron moving from A to B is the square of the sum of all the amplitudes along all possible paths:

$$w = \left|\sum_i A_i\right|^2 = \sum_i |A_i|^2 + \sum_{i \neq j} A_i A_j^* \ , \tag{2.6}$$

where the first summation is the classical probability, and the second one is due to interference between the different paths. For paths 1, 2, and 3, because their path lengths differ significantly, the phases of the electron wave functions also differ substantially along these paths. Therefore in summing over all the paths, the mean value of interference terms vanishes because of its oscillating nature. These paths are called incoherent paths. However there is a special kind of path, namely self-intersecting path as shown path 4 in Figure 2.2. It is phase coherent. Because an electron moves diffusively in the disordered metal, there is finite probability for the electron to be scattered back to its original position such as in path 4. In order to examine this specific kind of path, path 4 is enlarged and detailed in the bottom of Figure 2.2 [Ber 83]. Assuming an electron with the wave vector $\mathbf{k}$ has a wave function $e^{i(\mathbf{k}\cdot\mathbf{r}-\omega t)}$, then an electron at position 0 with wave vector $\mathbf{k_0}$ is scattered into two partial waves, which travel in clockwise (solid lines) and counterclockwise (dashed lines) directions on the loop. Bergmann claims that there is finite probability these two waves are scattered back to the position 0 with the wave vector $-\mathbf{k_0}$.

To examine the interference of the two partial waves after going around the loop, we must find the phases of the two back-scattered partial waves. Since the scattering is elastic, for the wave traveling in clockwise direction with initial wave vector $\mathbf{k}_0$, the phase change due to the direction change of the wave vector $\mathbf{k}$ at the ith center is $(\mathbf{k}_{i+1} - \mathbf{k}_i) \cdot \mathbf{r}_i$. The phase change due to the propagation between center i and center $(i+1)$ is $\mathbf{k}_{i+1} \cdot (\mathbf{r}_{i+1} - \mathbf{r}_i)$. The total phase change after sequence scattering $0 \rightarrow 1 \rightarrow \cdots \rightarrow 8 \rightarrow 0$ is

$$\begin{aligned}\Delta\phi \ = \ & (\mathbf{k}_1 - \mathbf{k}_0)\cdot\mathbf{r}_0 + \mathbf{k}_1\cdot(\mathbf{r}_1 - \mathbf{r}_0) + (\mathbf{k}_2 - \mathbf{k}_1)\cdot\mathbf{r}_1 + \mathbf{k}_2\cdot(\mathbf{r}_2 - \mathbf{r}_1) + \cdots + \\ & (\mathbf{k}_8 - \mathbf{k}_7)\cdot\mathbf{r}_7 + \mathbf{k}_8\cdot(\mathbf{r}_0 - \mathbf{r}_7) + (-\mathbf{k}_0 - \mathbf{k}_8)\cdot\mathbf{r}_0 = -2\mathbf{k}_0\cdot\mathbf{r}_0 \ ,\end{aligned} \tag{2.7}$$

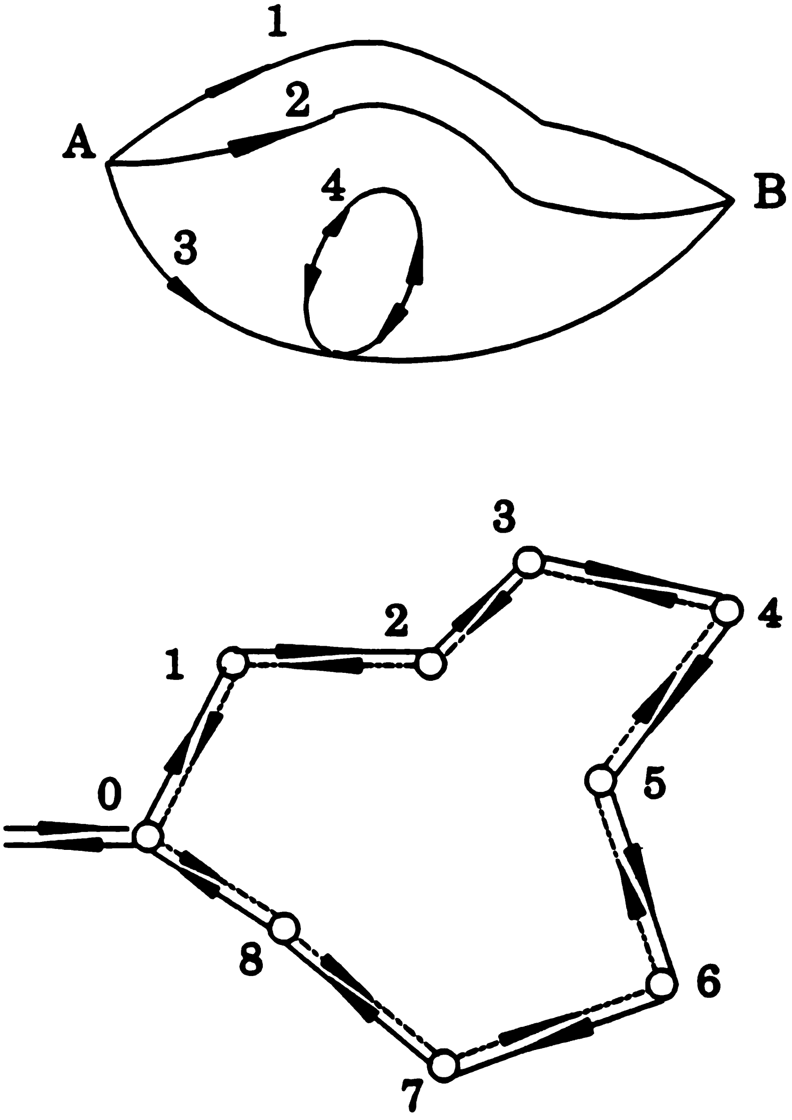

Figure 2.2: Electron scattering

where the final wave vector of the first partial wave is $-\mathbf{k}_0$. Similarly the other partial wave propagating in the opposite direction also from $\mathbf{k}_0$ to $-\mathbf{k}_0$ suffers the same phase change. These two partial waves have the scattering amplitude, where $|A_1| = |A_2|$ because of symmetry. Thus the total probability of finding the electron at position 0 is $|A_1 + A_2|^2 = 4|A|^2$, which is twice as much as the incoherent (classical) values. So the electron tends to be weakly localized at its origin, and this phenomenon is called weak localization. Since the phase difference between the two partial waves of an electron can be changed by phonons, magnetic fields, and spin impurities, etc, anything dephasing the partial waves will reduce the probability of the electron returning to its origin. Because the scattering probability is directly related to the resistivity ($\rho \sim 1/\tau$ =scattering probability), the quantum interference effects can be detected by measuring resistance vs temperature, magnetic field, and spin impurities etc. All these will be discussed in Section 2.3 and 2.4.

2.2.2 Spin-Orbit Interaction

In Section 2.2.1, the spins of two partial electron waves were not considered. But if there is an interaction with the electron spins such as the spin-orbit interaction between the electron spin and its orbit, the weak localization correction to resistivity could be changed dramatically or even reversed [Hik 80, Mae 81]. Bergmann [Ber 82] gave a vivid picture of how the spin-orbit interaction changes the sign of the quantum interference effect. Assume that an electron with spin up is scattered into two partial waves, then in the absence of spin-orbit coupling, these two scattered waves are in phase and interfere constructively and the probability of the electron returning to its original position is twice as much as the classical value. When there is a spin-orbit coupling, which depends on the angle between the electron spin and its momentum or velocity, the spins of the two partial electron waves will be rotated. Since two partial waves with parallel spins have opposite velocity, the spin-orbit interactions on the two waves have different signs. Thus their spins are rotated in the opposite direction. If we assign a matrix R for the spin rotation, when one partial wave reaches its original position after going round a closed loop, its spin state $|\chi\rangle$ will be rotated to $R|\chi\rangle$ while the other partial wave with the same initial spin state will reach a spin state $R^{-1}|\chi\rangle$ after going round the same loop. The interference of the two final states at their origin position gives a factor $\langle\chi|R^2|\chi\rangle$ before the interference terms in Equation 2.6. When the spin-orbit coupling is weak, this factor is close to one. For the case of dominating spin-orbit coupling, the electron spin completely loses its original orientation and its final orientation is statistical. From quantum mechanics, the 1/2 spin rotation matrix R, in three dimensions expressed in Euler angles, is

$$R = \begin{bmatrix} \cos(\theta/2)e^{[i(\phi+\psi)/2]} & i\sin(\theta/2)e^{[i(\phi-\psi)/2]} \\ i\sin(\theta/2)e^{[-i(\phi-\psi)/2]} & \cos(\theta/2)e^{[-i(\phi+\psi)/2]} \end{bmatrix} . \qquad (2.8)$$

Taking the square, we get

$$R^2 = \begin{bmatrix} \cos^2(\theta/2)e^{[i(\phi+\psi)]} - \sin^2(\theta/2) & \frac{i}{2}\sin(\theta)(e^{-i\phi} + e^{i\psi}) \\ \frac{i}{2}\sin(\theta)(e^{i\phi} + e^{-i\psi}) & \cos^2(\theta/2)e^{[-i(\phi+\psi)]} - \sin^2(\theta/2) \end{bmatrix} . \qquad (2.9)$$

If for the initial spin state $|\chi\rangle$=[a,b] and $|a|^2 + |b|^2 = 1$, then the expectation value of R^2 is

$$\begin{aligned} \langle\chi|R^2|\chi\rangle &= \cos^2(\frac{\theta}{2})\left\{|a|^2e^{[i(\phi+\psi)]} + |b|^2e^{[-i(\phi+\psi)]}\right\} \\ &\quad - \sin^2(\frac{\theta}{2}) + (i/2)\sin(\theta)[ab^*(e^{i\phi} + e^{-i\psi}) + c.c.] \ . \qquad (2.10) \end{aligned}$$

If there is no spin-orbit coupling, there are no spin flips. So all the angles are zeros, and the factor $\langle\chi|R^2|\chi\rangle$ is 1. Thus total probability of returning remains twice as much as the classical values. If the spin-orbit coupling is strong, final spin states are statistical. The statistical average of the factor $\langle\chi|R^2|\chi\rangle$ is $-1/2$. Thus the interference reduces the total probability of returning to the half of its classical value. An important effect on the quantum interference effect due to the strong spin-orbit coupling is that anything which dephases the scattering will increase the probability of an electron returning to its origin, and therefore increase the resistivity. Some of these dephasing mechanisms are electron-phonon interactions, spin scattering, and magnetic fields, which will be described in Sections 2.3 and 2.4.

2.2.3 Electron-electron Interactions

The weak localization effects that we have so far considered involve only single electrons and could take place even if electrons do not interact each other. For the case of electron-electron interactions, the interference between two electrons, which may have different energies, should be also considered.

How do electrons interact with each other in the presence of the weak localization? The answer is very complicated. Much work has been done in terms of the diagrammatic Green function method [Fuk 85]. A comprehensive review paper was published by Altshuler and Aronov [Alt 85]. In general, electrons interact in two different ways: called the diffusion channel and Cooper channel. In the diffusion channel, the two interacting electrons have parallel momenta, while in the Cooper channel, their momenta are antiparallel. If the interaction between two electrons in the Cooper channel is attractive due to exchange of virtual phonons, the system will cross over to the superconducting state. Even in the normal metallic state ($T > T_c$) or in the case of net electron repulsion, this electron-electron interaction still results in a nontrivial contribution to the resistivity.

In order to obtain a physical picture of the Coulomb interaction, Bergmann [Ber 87] has given a highly simplified interpretation. Beginning with the diffusion channel, Figure 2.3 shows how electrons interact in the presence of quantum interference effects. An electron wave which propagates from C is scattered by scattering centers (impurities, defects, or phonon, etc) and travels a loop: C$\rightarrow 1'' \rightarrow 2'' \rightarrow \cdots \rightarrow$C. At C the electron interferes with itself and forms a charge pattern. This charge pattern depends on the total phase shift that the electron suffered in going around the

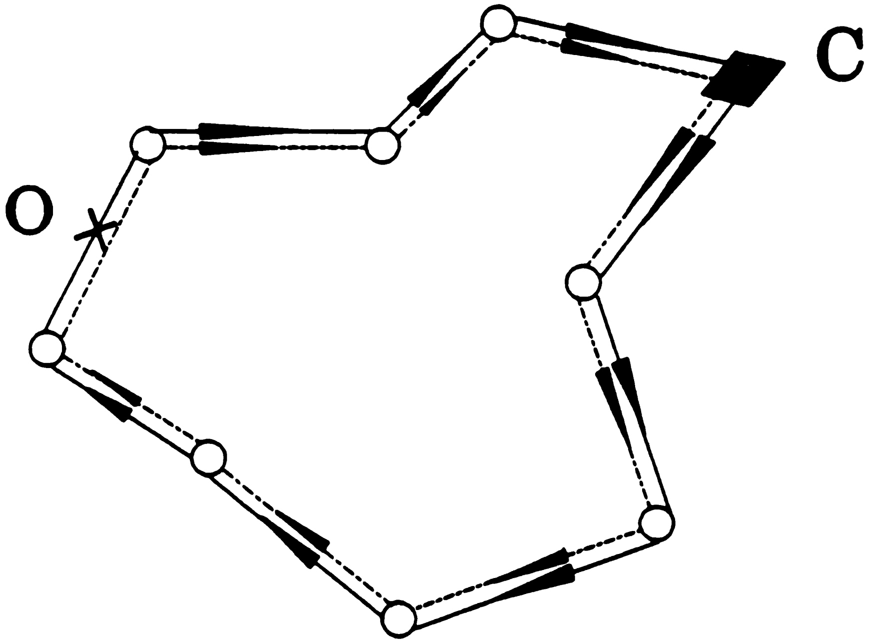

Figure 2.3: Interactions of two diffusion-channel electrons through the hologram at C

closed path, and it is called 'an electron hologram' by Bergmann. A second electron, starting from O, can go round the same path in same direction. During its trip, the second electron suffers the same phase change as the first electron from the scattering by impurities, phonon etc, but it also interacts with the charge hologram formed by the first electron. Bergmann claims that there is a finite probability that the phase change of the second electron on the closed loop can be precisely reversed by the interaction with the hologram so as to restore its original phase. So the phase difference of the two partial waves of the second electron at O is zero in comparison to the same electron without the electron-hologram interaction (which has nonzero phase difference due to inelastic scattering, etc.). Therefore waves of the second electron will interfere constructively at its original position O and enhance its backscattering probability.

For the Cooper channel, in which the two electrons travel in the opposite directions along the closed loop (Antiparallel momenta), the same conclusion is still valid.

Only electrons with energies within $k_B T$ of the Fermi energy are involved in an interaction. Because of this possible energy difference between the two electrons, the phase change of the second electron due to various scattering on the closed path will not be completely compensated by the hologram formed by the first electron on the same path. So as temperature goes higher, the dephasing of the second electron will grow. Therefore, the probability of finding the second electron at its original position (or resistivity) will decrease with increasing temperature. Since the electron energy difference is the order of $k_B T$, the thermal coherence time and related diffusion length are

$$\tau_{th} \sim \frac{\hbar}{\Delta E} \sim \frac{\hbar}{k_B T} \tag{2.11}$$

(2.12)

and

$$L_{th} = \sqrt{D\tau_{th}} \ , \qquad (2.13)$$

where D is the diffusion constant. Only electrons that return to their starting point within a coherence time can contribute to constructive interactions.

2.3 Zero Field Electrical Resistivity

The concepts given in Section 2.2 are correct for both two and three dimensional disordered systems. Since our sample dimension is above 20μm, which is much larger than thermal diffusion length L_{th}($< 0.02\mu$m for $T >$10mK), we can treat our sample as a three dimensional system for electron-electron interaction. We will show in section 4.4 that our samples are also three dimensional for weak localization. In this section, we will discuss the temperature dependence of the resistivity for three dimensional disordered conductors due to various dephasing mechanisms at zero magnetic field. The paraconductivities due the superconducting fluctuations will also be described.

2.3.1 Elastic Scattering and Dephasing

In disordered systems, electrons are scattered by the disordered lattice sites. At very low temperature and zero magnetic field, the scattering by these lattice sites gives the constructive or destructive interferences depending on the strength of spin-orbit coupling. Assuming no spin-orbit coupling, anything which dephases the scattering will reduces the probability of an electron returning to its original position. Therefore the resistivity will be lower. In order to estimate the effects of the dephasing on the resistivity, we assign two time constants τ_o and τ_d. τ_o is the minimum time for a scattering process and τ_d is a maximum time for coherence. Usually τ_o is called the elastic scattering time and τ_d is called the dephasing time. For an electron moving diffusively in a disordered metal (assuming that the electron at position $r = 0$ is scattered into two partial waves at $t = 0$), the probability of finding the electron at a distance between r and $r + dr$ at a time between t and $t + dt$ is given by the classical three dimensional diffusion Equation [Dug 87]:

$$p(r,t)drdt = \frac{1}{(4\pi Dt)^{3/2}} \exp(-r^2/4Dt)drdt \quad , \tag{2.14}$$

where D is the diffusion constant. The probability of the electron returning to a small fixed volume around the origin ($r = 0$) at a time between t and $t + dt$ is proportional to

$$p(r,t)dt \sim \frac{1}{(4\pi Dt)^{3/2}} dt \quad . \tag{2.15}$$

Since the two partial waves interfere constructively in the time interval $[\tau_o, \tau_d]$, the excess probability of the electron returning to the origin due to the interference (that is, the correction to the classical resistivity) can be obtained by integrating Equation 2.15 from τ_o to τ_d,

$$\frac{\Delta\rho}{\rho} \sim \int_{\tau_o}^{\tau_d} \frac{1}{(Dt)^{3/2}} \sim \frac{1}{\sqrt{\tau_o}} - \frac{1}{\sqrt{\tau_d}} \quad . \tag{2.16}$$

We see, first of all, that when dephasing is so strong that τ_d and elastic scattering τ_o are equal, no correction to the classical resistivity is required. If there is no dephasing($\tau_d^{-1} = 0$), the correction to the classical resistivity is positive and proportional to $1/\sqrt{\tau_o}$. Between the two extremes, the correction decreases with decreasing τ_d. Since τ_d is usually temperature dependent, we can observe and study the quantum interference effect by measuring the temperature dependence of the resistivity.

2.3.2 Inelastic and Spin Scattering

The electron phonon interaction can cause inelastic scattering. At a finite temperature, two partial waves of a scattered electron interact with phonons, so their energies are changed. This energy difference (ΔE) introduces a phase difference of an order $\Delta Et/\hbar$ for the two partial waves scattered back to the origin. When this phase change is the order of π, the dephasing time, which is called the inelastic scattering time, is

$$\tau_i \sim \frac{\pi\hbar}{\Delta E} \ . \tag{2.17}$$

Since the electron-phonon interaction energy (ΔE) increases with temperature, τ_i usually decreases with temperature. A simple power law $\tau_i = \tau_{io}T^{-p}$ has been suggested by some authors [Alt 85, Ber 84], and experiments have provided some evidence for such a power law [How 86, Sch 86].

The spin scattering is due to the magnetic impurities in the host metals. The spins of the partial waves of a scattered electron interact with those of the impurity atoms and change the relative phases of the two spin states. The dephasing time, when phase difference is π, is called spin scattering time (τ_s), which usually decreases with increasing the concentration of magnetic impurities.

2.3.3 Weak Localization with Spin Orbit Scattering

In Section 2.2.2, we learned that the spin-orbit coupling could reverse the sign of weak localization correction to the resistivity. If we consider all the scattering mechanisms such as elastic, inelastic, spin, and spin-orbit scattering, then we have for the dephasing probability $1/\tau \sim 1/\tau_{so} + 1/\tau_i + 1/\tau_s$. The detailed calculations were performed using the Green function method by many theorists [Alt 85, Fuk 85, Ber 84]. The correction to the resistivity is

$$\frac{\Delta\rho}{\rho^2} = \frac{e^2}{2\pi^2\hbar\sqrt{D}}\left(\sqrt{\frac{1}{4\tau_i}+\frac{1}{4\tau_s}} - 3\sqrt{\frac{1}{4\tau_i}+\frac{1}{\tau_s}+\frac{1}{\tau_{so}}}\right) \ , \tag{2.18}$$

where τ_i is inelastic relaxation time. τ_s and τ_{so} are spin and spin-orbit scattering lifetimes respectively. We see that when there is no spin-orbit coupling ($\tau_{so}^{-1} \sim 0$), the resistivity decreases with decreasing τ_i and τ_s (or increasing temperature and spin impurity concentration). If the spin-orbit coupling is very strong ($\tau_{so}^{-1} \gg \tau_{ie}^{-1}, \tau_s^{-1}$), the resistivity increases with temperature and spin impurity concentration.

2.3.4 Electron-electron Interactions

Since the electron-electron interaction involves two electrons near the Fermi surface, the energy difference of the electrons is the order of $k_B T$. So the dephasing time $\tau_{ee} \sim \hbar / k_B T$. From Equation 2.16, its correction to the resistivity is

$$\Delta\rho/\rho^2 \sim -\frac{1}{\sqrt{D\tau_{ee}}} \sim -\sqrt{\frac{k_B T}{\hbar D}} \ . \tag{2.19}$$

In fact, the electron-electron interactions are very complicated and different in the diffusion and Cooper channels. Equation 2.19 only gives the general feature of the electron-electron interactions. The quantitative calculations have been done using the Green's function methods.

In the diffusion channel, electrons have parallel momenta, but they may have parallel or antiparallel spins i.e the two electrons may be in either in singlet (spin =0) or triplet (spin=1) states. Including this spin splitting, Altshuler *et al* [Alt 85] calculated the Coulomb correction to the resistivity in the diffusion channel

$$\frac{\Delta\rho}{\rho^2} = -\frac{1.3e^2}{4\sqrt{2}\pi^2\hbar}\left[\frac{4}{3} - \frac{3}{2}\tilde{F}_\sigma)\right]\sqrt{\frac{k_B T}{\hbar D}} \ , \tag{2.20}$$

where $\tilde{F}_\sigma$ is, in Thomas-Fermi approximation, given by

$$\tilde{F}_\sigma = \frac{32}{3F}[(1+\frac{1}{2}F)^{3/2} - 1 - \frac{3}{4}F] \ , \tag{2.21}$$

$$F = \frac{\ln(1+\chi)}{\chi} , \qquad \chi = \left(\frac{2k_F}{k_s}\right)^2 \ ,$$

where k_F is the Fermi wave vector and k_s the Thomas-Fermi screening length. Here $0 \leq F \leq 1$ and $0 \leq \tilde{F}_\sigma \leq 0.93$. If the electron-phonon coupling is considered, the effective mass of an electron is then enhanced [How 88] by

$$m^* = (1 + \lambda_{ep})m_e \ , \tag{2.22}$$

where λ_{ep} is called the electron-phonon mass enhancement constant. Howson claims that $\tilde{F}_\sigma$ should be replaced by $(\tilde{F}_\sigma - \lambda_{ep})$ when the electron-phonon coupling is considered.

In the Cooper channel, the two electrons have antiparallel momenta. If the electrons attract each other via virtual phonon exchange, they will form Cooper pairs and the system will cross to a superconducting state. This interaction will enhance the conductivity. For $|\ln(T/T_c)| \gg 1$, the correction to the resistivity in the Cooper channel [Alt 85] is

$$\frac{\Delta\rho}{\rho^2} = -\frac{1.3e^2}{4\sqrt{2}\pi^2\hbar}\frac{2}{\ln(T/T_c)}\left(\frac{k_BT}{\hbar D}\right)^{1/2} , \tag{2.23}$$

where T_c is the superconducting transition temperature.

In the case of net electron repulsion, the system will not go to a superconducting state, but the Cooper channel interaction still results in a nontrivial contribution to the resistivity. For the non-superconducting case, T_c is replaced by T_F, the Fermi temperature, in Equation 2.23.

2.3.5 Superconducting Fluctuations

If the disordered metals or alloys are superconductors, the superconducting fluctuations will change temperature dependence of the resistivity especially near T_c[Sko 75].

For the temperature above T_c, the superconducting fluctuations will contribute excess conductivity, especially at $T \sim T_c$. In general there are two kinds of contributions from the superconducting fluctuations: Aslamazov-Larkin (direct) and Maki-Thompson (indirect).

Aslamazov-Larkin contribution was firstly derived by Aslamazov and Larkin in 1968 [Asl 68]. This excess conductivity is due to the direct acceleration of the fluctuation-induced superconducting pairs in an electric field. Since the superconducting pairs decay very rapidly at $T > T_c$, this contribution is important only at T

close to T_c. In terms of the Ginzburg-Landau theory [Sko 75], this contribution to the conductivity in three dimension for T very close to T_c is

$$\Delta\sigma_{AL}(T) = \frac{e^2}{32\hbar\xi_{GL}(0)}\left(\frac{T-T_c}{T_c}\right)^{-1/2} , \tag{2.24}$$

where $\xi_{GL}(T)$ is the coherence length of Cooper pairs at temperature T. In the disordered ("dirty") superconductors [Sch 90], it reduces to

$$\xi_{GL}(T) = 0.85[\xi_o(0)l]^{1/2}\left(\frac{T_c-T}{T_c}\right)^{-1/2} . \tag{2.25}$$

At $T = 0$K, we have

$$\begin{aligned} \xi_{GL}(0) &= 0.85(\xi_o(0)l)^{1/2} \\ &= 0.85\sqrt{\frac{0.18\pi}{2}\frac{\hbar v_F}{k_B T_c}l} \\ &= 0.783\sqrt{\frac{\hbar D}{k_B T_c}} , \end{aligned} \tag{2.26}$$

where $\xi_o(0)$ is the coherence length in the clean crystalline case, l is the mean free path, and v_F is the Fermi velocity. We see from Equation 2.24 and 2.26 that $\Delta\sigma_{AL} \propto T_c$. Thus for our samples with $T_c < 15$mK, $\Delta\sigma_{AL}$ will be intrinsically small.

In addition, for $\epsilon = (T - T_c)/T_c > 0.1$, experiments [Toy 84, Joh 78] show that the Aslamazov-Larkin fluctuation contribution to the conductivity decays much more rapidly with increasing ϵ than the Equation 2.24 indicates. Johnson *et al.* [Joh 78] interpreted this behavior as being due to a breakdown of the slow-variation approximation in the Ginzburg-Landau theory, and they introduced a short wavelength cutoff $Q_c \sim \xi^{-1}(0)$ in the fluctuation spectrum. With this assumption, the effective Aslamazov-Larkin contribution σ' for $\epsilon > 0.1$ is given by

$$\frac{\sigma'}{\sigma_{AL}} = \frac{2}{3\pi}\left[\frac{2x_c}{(1+x_c^2)^2} - \frac{5x_c}{(1+x_c^2)} + 3\tan^{-1}(x_c)\right] , \tag{2.27}$$

where σ_{AL} is given by Equation 2.24 and $x_c \sim 1/\sqrt{\epsilon}$ for dirty superconductors. For example, with $T/T_c = 2$, Equation 2.27 gives that $\sigma'/\sigma_{AL} \simeq 0.08$. Thus if T is kept sufficiently larger than T_c, the Aslamazov-Larkin term can be neglected.

The Maki-Thompson (MT) contribution is an indirect effect. The direct acceleration of the fluctuation-induced superconducting pairs leads to the Aslamazov-Larkin contribution. These superconducting fluctuations then decay into pairs of quasiparticles which remain in a state of small total momentum even after scattering from an impurity potential and continue to be accelerated as much as they were while they were a superconducting fluctuation. The quasiparticle life time, limited by the scattering from impurities and decaying back into a superconducting fluctuation, can be much longer than that of the superconducting pairs. So the Maki-Thompson contribution can persist to temperatures much higher than T_c. Maki [Mak 68a, Mak 68b] first calculated this contribution, but there was a divergence in two or lower dimensions. To remove the divergence, Thompson [Tho 70] introduced a pair breaking parameter α. For $T \sim T_c$, the Maki-Thompson contribution is

$$\Delta\sigma_{MT}(T) = \frac{4\alpha e^2}{32\hbar\xi_{GL}(0)}\left(\frac{T - T_c}{T_c}\right)^{-1/2} , \tag{2.28}$$

where α is related to the inelastic scattering time [Pat 74, San 85] by

$$\alpha = \frac{\hbar}{8k_BT\tau_i} = \frac{eD}{2k_BT}B_i(T) , \tag{2.29}$$

and $B_i = \hbar/4eD\tau_i$, is called dephasing or scattering field.

Some experiments [Joh 78, Toy 84] indicates that the Maki-Thompson contribution for $T > T_c$ is absent due to a strong pair breaking effect. In our case, the pair breaking parameter $\alpha \sim 0.03T^{p-1}$ with $p > 1.6$. Thus for $T > T_c \sim 10$mK, the Maki-Thompson contribution is very small.

In summary, at zero magnetic field and for $\ln(T/T_c) \gg 1$, where Aslamazov-Larkin and Maki-Thompson fluctuation contributions are negligible, the corrections to resistivity due to the weak localization and the electron-electron interaction, assuming that they are additive, are

$$\frac{\Delta\rho}{\rho^2} = -\frac{1.3e^2}{4\sqrt{2}\pi^2\hbar}\left[\frac{4}{3} + \frac{3}{2}(\lambda_{ep} - \tilde{F}_\sigma) + \frac{2}{\ln(T/T_c)}\right]\left(\frac{k_BT}{\hbar D}\right)^{1/2}$$

$$+\frac{e^2}{2\pi^2\hbar\sqrt{D}}\left(\sqrt{\frac{1}{4\tau_i}+\frac{1}{\tau_s}}-3\sqrt{\frac{1}{4\tau_i}+\frac{1}{\tau_s}+\frac{1}{\tau_{so}}}\right) \ . \tag{2.30}$$

2.4 Magnetoresistivity

2.4.1 Weak localization with magnetic fields

As we know from the previous discussions, anything which dephases the closed loop scattering will change interference pattern of the two back-scattered waves. If we apply a magnetic field, the phase change on a wave function going around a closed loop is

$$\Delta\phi = 2\pi\frac{2e}{h}\oint \mathbf{A}\cdot d\mathbf{l} = \frac{2eBS}{\hbar} \ , \tag{2.31}$$

where $h/2e$ is one flux quanta and S is the area of the closed loop. Since electrons move diffusively in a disordered metal, we have $S \sim Dt$. Because the two partial waves of an scattered electron travel in opposite direction, the phase changes for the two partial waves are $\pm 2eBDt/\hbar$ respectively. Thus the phase difference between these two waves is $4eBDt/\hbar$. When the phase difference is $\sim \pi$, the magnetic dephasing time is given by

$$\tau_B \sim \frac{\hbar}{4eDB} \ . \tag{2.32}$$

Including also the spin-orbit coupling, the weak localization correction to the magnetoresistivity is

$$\frac{\Delta\rho(B)}{\rho^2} \sim \mp\sqrt{\frac{1}{\tau_B}} \sim \mp\sqrt{B} \ , \tag{2.33}$$

where '$-$' sign corresponds to weak or no spin-orbit coupling and '$+$' sign to the strong spin-orbit coupling (see Equation 2.18).

Another dephasing mechanism is called the Zeeman splitting effect. In the presence of the spin-orbit interaction, the spins of the two back-scattered partial waves of an electron are no longer parallel. An external magnetic field introduces an energy difference between the two waves with different spin orientation, which then produces a phase difference. If there is no spin-orbit coupling, there is no Zeeman splitting. The general formula, including weak localization, spin-orbit coupling, and Zeeman splitting, was given by Fukuyama [Fuk 81]:

$$\begin{aligned}\left(\frac{\Delta\rho}{\rho^2}\right)_{WL} &= \frac{e^2}{2\pi^2\hbar}\sqrt{\frac{eB}{\hbar}}\left\{-f_3\left(\frac{B}{B_\phi}\right)+\frac{1}{2\sqrt{1-\gamma}}\left[f_3\left(\frac{B}{B_-}\right)-f_3\left(\frac{B}{B_+}\right)\right]\right\} \\ &\quad +\frac{e^2}{2\pi^2\hbar}\sqrt{\frac{4eB_{so}}{\hbar}}\left[\sqrt{t+1}-\sqrt{t}-\frac{1}{\sqrt{1-\gamma}}(\sqrt{t_+}-\sqrt{t_-})\right] \quad , \qquad (2.34)\end{aligned}$$

where B is the magnetic field, $t = \tau_{so}/(4\tau_i)$, $\gamma = (g\mu_B\tau_{so}B/2\hbar)^2$, $t_\pm = t + 0.5(1 \pm \sqrt{1-\gamma})$, $B_x = \hbar/(4eD\tau_x), B_\phi = B_i + 4B_{so}, B_\pm = 4B_{so}t_\pm$, and

$$f_3(x) = \sum_{n=0}^{\infty}\Bigg[2\left(n+1+\frac{1}{x}\right)]^{1/2} - 2\left(n+\frac{1}{x}\right)^{1/2} - \left(n+\frac{1}{2}+\frac{1}{x}\right)^{-1/2}\Bigg] \quad . \qquad (2.35)$$

The first term (inside the curly brackets) is the weak localization contribution in the presence of spin-orbit coupling and Zeeman effect. The second term (inside the square bracket) is due to the Zeeman splitting in the presence of the spin-orbit coupling. Please note that the above expression is independent of the magnetic field orientation with respect to the measuring current in three dimensions [Alt 85, Kaw 80a, Kaw 80b, Kaw 81].

2.4.2 Electron-electron Interaction

In the presence of a magnetic field, electrons interact with each other also through both the diffusion and the Cooper channels as in zero field, but the interactions act differently in non-zero field. First, the energies of the two interacting electrons are split due to the magnetic field–Zeeman effect. Second, the magnetic field directly introduces a dephasing for the two electron orbits. Note that " two electron interaction" means that the second electron interacts with the hologram formed by the first electron on the same loop, as shown in Figure 2.3.

For the diffusion channel, the momenta of the two interacting electrons are parallel. In a magnetic field, if their spins are also parallel, the magnetic flux through the closed loop that electrons traveled are same for both electrons. So there is no phase difference between the two electrons. The magnetoresistivity is not affected by this part of the interaction. If the spins of the two electrons are antiparallel, the energy difference of the two electrons is about $(\mu_B B)$. Thus the hologram of the spin up electron does not perfectly compensate the phase shift of the spin down electron and vice versa. This effect is also called Zeeman splitting effect. The correction to the resistivity due to the Zeeman splitting is given by Lee *et al* [Lee 82]

$$\left(\frac{\Delta\rho}{\rho^2}\right)_{DC} = \tilde{F}_\sigma \frac{e^2}{4\pi^2\hbar}\sqrt{\frac{k_B T}{2D\hbar}}\, g_3\left(\frac{g\mu_B B}{k_B T}\right) , \tag{2.36}$$

where $\tilde{F}_\sigma$ is given in Equation 2.21, g is the Lande g-factor for electrons, μ_B is the Bohr magneton, and

$$g_3(x) = \int_0^\infty d\omega \left[\frac{d^2}{d\omega^2}\left(\frac{\omega}{e^\omega - 1}\right)\right]\left(\sqrt{\omega + x} + \sqrt{|\omega - x|} - 2\sqrt{\omega}\right) \tag{2.37}$$

In the Cooper channel, the momenta of the two interacting electrons are antiparallel; i.e., they travel around the same loop in opposite directions. The magnetic field introduces the phase difference of the order $4eBDt/\hbar$ between the two electron orbits, which dominates the dephasing. If the electron interaction is attractive via virtual phonons, the system crosses over to the superconducting state. The magnetic dephasing and the attractive interaction enhance the conductivity for $T > T_c$, and the correction due to the Cooper channel [Alt 81] is

$$\left(\frac{\Delta\rho}{\rho^2}\right)_{CC} = \alpha \frac{e^2}{2\pi^2\hbar}\sqrt{\frac{eB}{\hbar}}\, g(B,T)\phi_3\left(\frac{2DeB}{\pi k_B T}\right) , \tag{2.38}$$

where

$$\phi_3(x) = \left(\frac{\pi}{2x}\right)^{1/2}\int_0^\infty \frac{t^{1/2}}{\sinh^2(t)}\left(1 - \frac{xt}{\sinh(xt)}\right) dt , \tag{2.39}$$

α is a dimensionless constant, which equals 1 for weak spin-orbit coupling and 0.25 for the strong coupling, $1/g(B,T) = -\ln(T^*/T_c)$ with T^* =max$(T, 4DeB/k_B)$ for superconducting metals, and $1/g(B,T) = 1/\lambda_{ep} + \ln(\gamma T_F/\pi T^*)$ for normal metals [Bax 89]. In this last expression, T_F is the Fermi temperature, γ is the Euler's constant (0.577), and λ_{ep} is the electron phonon coupling constant.

The analytical approximations with 0.1% error for f_3, ϕ_3, and g_3 have been given by Ousset and Baxter *et al.* [Ous 85, Bax 89].

2.4.3 Superconducting Fluctuations

In the presence of a magnetic field, the superconducting transition temperature is depressed. Like impurities and defects, the external field is also a source for the decay of the superconducting fluctuations and the quasi-Cooper pairs. Therefore with increasing magnetic fields, the paraconductivity due to the superconducting fluctuations will be reduced. As in zero magnetic field, there are two kinds of superconducting fluctuations: Aslamazov-Larkin and Maki-Thompson fluctuations. These fluctuations usually depend on the relative direction between current and magnetic field.

Aslamazov-Larkin effect. This contribution is only important for T close to T_c. Many authors [Usa 69, Ber 69] have calculated this contribution for thin films and bulk material. For magnetic field parallel to the current, Usadel [Usa 69] derived

$$(\Delta\sigma_{\|})_{AL} = \frac{e^2}{16\hbar}\left(\frac{\pi D}{8\hbar k_B T}\right)^{1/2} \sum_{n=0}^{\infty} \frac{eB}{\left[\ln(\frac{T}{T_c}) + \frac{\pi e D B}{4k_B T}(2n+1)\right]^{3/2}} \quad . \tag{2.40}$$

The expression for the field perpendicular to the current can be found in the paper by Usadel [Usa 69]. Bergmann also calculated the same contribution, and he claimed that both transverse and longitudinal magnetoresistivity for three dimensional superconductors are same to the first order in small magnetic fields.

Maki-Thompson effect. As in the zero field, this effect can persist to temperatures much higher than T_c. For two dimensional systems, this contribution was first calculated by Larkin [Lar 80]. He showed that the Maki-Thompson contribution has the same magnetic field dependence as weak localization, but with the opposite sign and a coefficient $\beta(T)$ which diverges at T_c. Although a lot of theoretical work has been done for the two-dimensional magnetoresistance, little work has been done for the three dimensional case. In the limit of small magnetic field, the relation that Larkin obtained may be extended to three dimension [Alt 85, Bax 89]. From Bergmann's work on the Aslamazov-Larkin effect [Ber 69], we assume that the same relation is applicable to the longitudinal magnetoresistance, which is

$$\left(\frac{\Delta\rho}{\rho^2}\right)_{MT} = \beta(T)\frac{e^2}{2\pi^2\hbar}\sqrt{\frac{eB}{\hbar}}f_3\left(\frac{B}{B_i}\right) , \tag{2.41}$$

where $B_i = \hbar/4eD\tau_i$. f_3 is the same function given in Equation 2.35. $\beta(T)$ has been derived by Santos *et al* [San 85]:

$$\beta(T) = \frac{\pi^2}{4}\sum_{m=-\infty}^{\infty}(-1)^m\Gamma(|m|) - \sum_{n=0}^{\infty}\Gamma''(2n+1) , \tag{2.42}$$

where

$$\Gamma(|m|) = \left[-g^{-1} + \psi\left(\frac{1}{2} + \frac{|m|}{2}\right) - \psi(\frac{1}{2}) - \psi'\left(\frac{1}{2} + \frac{|m|}{2}\right)\frac{1}{4\pi k_B T\tau_i}\right]^{-1} . \tag{2.43}$$

In the case of small applied fields and inelastic fields

$$B, B_i \ll \frac{k_B T}{4De}\ln(\frac{T}{T_c}) , \tag{2.44}$$

$\beta(T)$ reduces the function given by Larkin, which is tabulated in Table 2.1 and will be used in the analysis for our magnetoresistances. From the table, we see that $\beta(T)$ decays very rapidly for $T \geq T_c$ and varies as $\ln^{-2}(T/T_c)$ for $T \gg T_c$.

Table 2.1: $\beta(T)$ vs T

T/T_c	4.5×10^{-5}	22000	148.4	28.0	7.38	3.49	2.72	1.65	1.22	1.11
$\ln^{-1}(\frac{T}{T_c})$	-0.1	0.1	0.2	0.3	0.5	0.8	1	2	5	10
$\beta(T)$	0.017	0.015	0.06	0.13	0.33	0.73	1.05	3.0	9.8	22

Chapter 3

Experimental Techniques

In this chapter, we will describe the major apparatus and experimental methods used in this study. Details will be given about the sample sandwich, magnet, sample preparation, thermometry, and measurement procedure. In addition, electrical and thermal contacts, residual and boundary resistance, and heat flow in the system will be discussed.

3.1 Main Apparatus

3.1.1 The Dilution Refrigerator

Since we are interested in the resistivity of amorphous CuTi alloys below 6K, a locally-built dilution refrigerator [Ime 74, Ime 75, Hei 83] was employed. It takes the refrigerator 12 hours to cool from room temperature to liquid nitrogen temperature (77K), and 2 hours from 77K to 4.2K with about 18 liters of liquid helium. The lowest temperature (about 13mK) can be reached after about 5 hours of continuous ^{3}He/^{4}He mixture circulation. A detailed description of a dilution refrigerator is given by O. Lounasmaa [Lou 74].

3.1.2 High Precision Resistance Bridge

For amorphous CuTi alloys at temperature below 6K, the relative change of the resistivity, $\Delta\rho/\rho$, is about 10^{-5} at 1K with ΔT=0.1K. Therefore a high precision current comparator system with SQUID (Superconducting Quantum Interference Device) null detector [Edm 80] was used. As you will see in Section 3.4.1, in the most interesting temperature range (T<6K), this system can resolve the quantity ($\Delta\rho/\rho$) to a precision of better than 0.1ppm.

3.1.3 Glove Box and Vacuum System

As you will see in Section 3.2.2, we used potassium as a non superconducting glue for making good electrical and thermal contact between CuTi ribbons and Cu electrodes. Since potassium reacts strongly with oxygen and water, a commercial argon-filled glove box, made by Vacuum Atmospheres Company, was used for making samples. The inert atmosphere inside the glove box was maintained by a locally built argon purification system. Although we have not directly measured the contamination due to water vapor and oxygen, we know that the water and oxygen concentration is less than 0.4ppm since potassium stays shiny for a few hours inside the glove box [Yin 87].

3.2 Sample Preparation

In this section, we will describe the techniques for sample preparation and for precision perpendicular resistance measurement on amorphous-metal ribbons with very reliable thermometry down to 15mK.

3.2.1 Preparation of CuTi Alloy Ribbons

CuTi alloys ribbons were prepared at University of Leeds, UK by the melt spinning method. High pure Copper(99.999%) and Titanium(99.98%), mixed in desired concentration, were melted and poured to a fast spinning copper wheel which was in an argon atmosphere. The CuTi liquid mixture, cooled at a rate of 10^6K/s, formed a amorphous alloy on the surface of the wheel. The amorphous structure of the alloy is confirmed by x-ray diffraction shown in Figure 3.1 ($\lambda_{\mathrm{Cu}} = 1.54\AA$). The alloys made by this method are ribbon-like with a width of 3–5mm and thickness around 40μm. Their resistivities are in the range of 180 to 220$\mu\Omega$cm, depending on the relative concentration of Cu and Ti.

3.2.2 Sample Sandwich

Our measurements take place at temperatures between 15mK and 6K. In order to cool the sample to very low temperature (15mK), the heat generated in the system should be as low as possible. The current through the sample from the high precision current comparator is about 20mA. In order to use the high precision current comparator and not to produce noticeable heat (<4nW) in the sample or its reference resistor, the resistances of both sample and reference must be less than 10$\mu\Omega$. Since the resistivity of the CuTi alloys is about 200$\mu\Omega$cm, the resistance of a CuTi ribbon is about 0.2Ω if measured parallel to the plane of the ribbons. The heat produced by this resistance with 20mA current is about 10^{-4} Watt and is high enough to warm the sample to well above 0.5K. To reduce the heat load, either current or resistances must be lowered. Lowering current will reduce the precision of our measurements. Therefore the resistance of the sample should be lowered dramatically. We have developed a novel method to reduce the resistance to about 10$\mu\Omega$ by measuring the resistance perpendicular to CuTi ribbons. A special sample sandwich was designed and built to achieve our goals. The sandwich is made of two cylindrically-shaped Oxygen Free High Conductivity (OFHC) Cu electrodes placed on the opposite sides of a CuTi ribbon. Figure 3.2 gives the reader a detailed view of the sample sandwich.

In order to passivate the magnetic impurities and thereby the Kondo effect, the

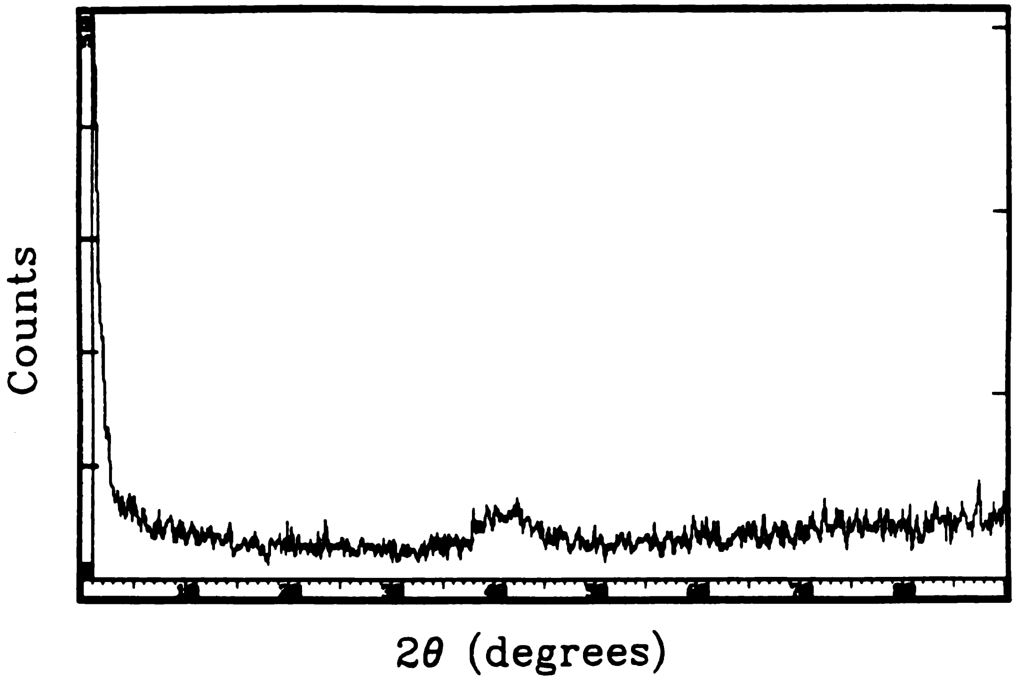

Figure 3.1: X-ray diffraction of amorphous CuTi ribbons

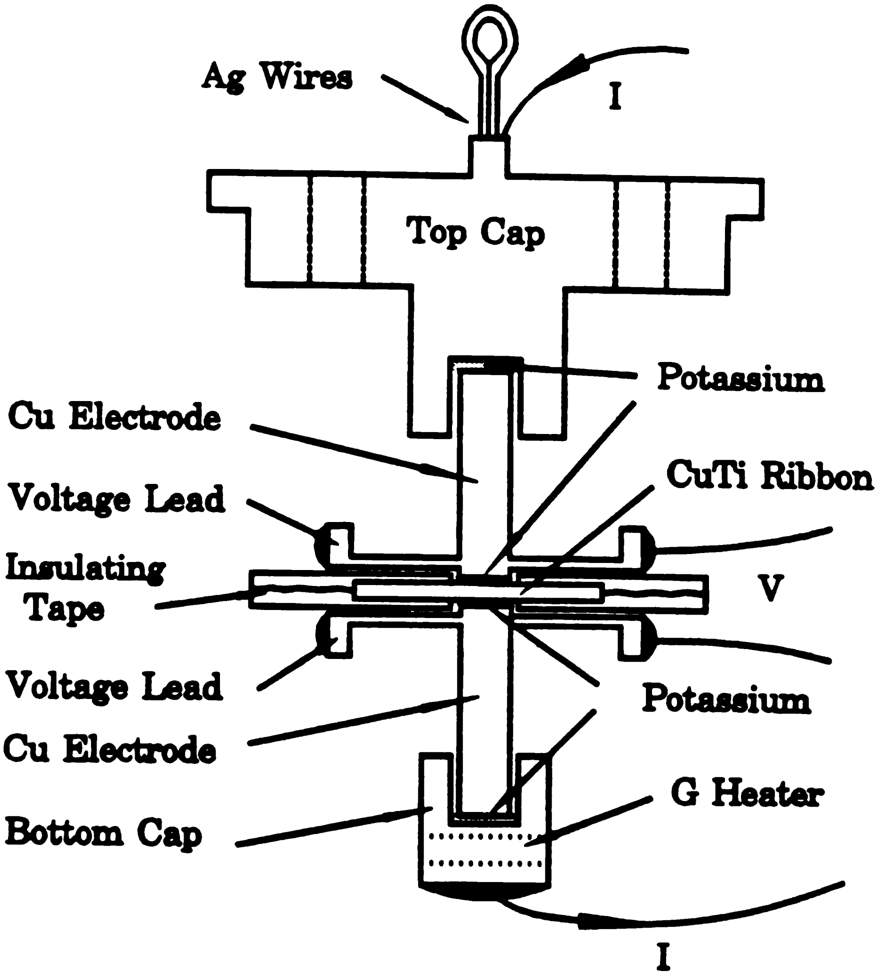

Figure 3.2: Sample sandwich. Solid black regions on voltage probes and bottom cap indicate presence of Pb(Sn) superconducting solder.

OFHC copper was annealed in oxygen atmosphere with a pressure 4.8×10^{-4}torr at 950°C for four days. The RRR (Residual Resistivity Ratio = $R(300\mathrm{K})/R(4.2\mathrm{K})$) of the annealed Cu was about 400 in comparison to 100 for unannealed Cu. The ratio of diameter to length of each copper electrode is less than 1/3 in order to reduce current convergence or divergence. The diameter of each voltage lead is much bigger than its thickness, so that currents flowing into voltage leads are negligible. The distance between a voltage lead and the nearby surface of the Cu electrode is about 0.13mm. The contribution from this layer of copper is less than 0.01% of the total resistance of the Cu/K/CuTi/K/Cu sandwich between the voltage probes. To eliminate the superconducting proximity effect in the Cu, the voltage leads were nickel plated before the superconducting Pb(Sn) solder was put on as discussed later in Section 4.1. The two outside ends of the Cu electrodes are attached to two Cu caps using potassium as a glue. The top cap, which also served as a current lead, was spot welded to a silver wire. The silver wire is used for making a connection to a silver mount at the bottom of the mixing chamber, so that excellent thermal conduction between the sandwich and the refrigerator is guaranteed. If required, the bottom cap, can be used to mount a G heater so that the thermoelectric G ratio (see Section 3.4.1) can be measured. The nylon insulating tape, glued on both sides of a CuTi ribbon, is used for preventing electrical shorting between the voltage leads. Potassium is used as non superconducting glue to make good electrical and thermal contacts at the interfaces.

The resistances of CuTi ribbons have been measured by many researchers. All of them used the parallel method by applying current parallel to the plane of a CuTi ribbon. The precision of $\Delta\rho/\rho$ in their measurements was about 10^{-5}. One of the disadvantages of their measurements is that they used varnish as an agent for non-electrical heat conduction. In the varnish, the heat is carried by phonons. At very low temperatures, the thermal conduction by phonons is poor, and their sample will not cool well. In comparison to the parallel method, our method has two unique features:

1) A high precision, $\Delta\rho/\rho = 10^{-7} - 10^{-8}$, has been achieved by using our high precision resistance bridge.

2) The direct contacts between CuTi and the Cu electrodes using potassium as a glue allow the thermometers, the CuTi sample, and the refrigerator to have excellent thermal contact each other. At very low temperature, where thermal conduction by phonons is poor, most of the heat is carried by electrons in a metal. Thus using a non-superconducting metallic glue assures excellent thermal contacts at temperatures below 0.25K. In principle, our method is applicable to any high resistivity metal or alloy in a ribbon or film form.

3.2.3 Electrical and Thermal Contact and Cu Sputtering

The contacts between CuTi ribbons and Cu electrodes are crucial to our measurements. Very good electrical and thermal contacts have been achieved with the following two methods.

(1) Direct Cleaning: Both the Cu electrodes and CuTi ribbon were cleaned in air with acetone and alcohol. Then they were put into the Ar filled glove box. After staying in the glove box for about 2 hours, the surface oxide layers of CuTi ribbon and Cu electrodes were removed with knives and files, and potassium was rubbed on the cleaned CuTi surface immediately.

(2) Cu Sputtering: A better way to clean the surface of the CuTi ribbons is to use an ion milling machine in a high vacuum. This was done in the follow way: The CuTi ribbons were first cleaned by ultrasonic waves in acetone, then they were mounted on a plate inside the vacuum chamber of the sputtering machine. The chamber was pumped to 10^{-8} torr and the ribbons were actively cooled to −20°C. The surface oxide layers of the CuTi ribbons were removed by bombarding the surface with an Ar ion beam for less than 60 seconds. The ion beam current was 2−6 mA and acceleration

voltage was 50V. Then, the high purity copper was sputtered onto the cleaned surface for about 4 minutes. The thickness of the Cu overlayer was about 3000Å. The above procedure was repeated for the other side of the CuTi ribbons. Finally, following steps in (1), good contacts between the Cu coated CuTi ribbons and potassium could be made.

One disadvantage of this method is the heating of the ribbons during the ion milling and Cu sputtering. By mounting a thermocouple directly on a CuTi ribbon, we observed that the temperature increase mainly due to the ion milling was $\leq 100°$C. By doing x-ray diffraction on these ribbons (with Cu etched away), we saw the same x-ray diffraction pattern as that of a bare CuTi ribbon (see Figure 3.1). Thus this heating does not anneal and recrystallize the amorphous CuTi ribbon.

3.2.4 Magnet and Current Supply

Magnetoresistance measurement at low temperatures and low fields is one of the most important measurements to make. In order to get stable magnetic fields below 6K, we designed and built a small superconducting magnet.

The magnet shown in Figure 3.3 is made of copper. It is a hollow cylinder, 3cm long by 1.0cm in diameter. About 1200 turns of single-filament NbTi superconducting wire were wound on the Cu cylinder in eight layers. Between the superconducting-wire layers, Apiezon-N-grease coated mylar was wrapped to prevent possible electrical shorting among the wires and to conduct away heat produced in the wires. The outermost layer was tied with threads and painted with a liquid insulating tape, made by GC Electronics. The sample sandwich can be inserted from one end of the magnet. Good thermal contact was achieved by pressing together the magnet and the upper Cu cap of the sandwich with three screws. The position of the CuTi ribbon between the Cu electrodes in the sample sandwich is very near the middle of the magnet. The magnetic fields produced by this magnet were measured by a low-field

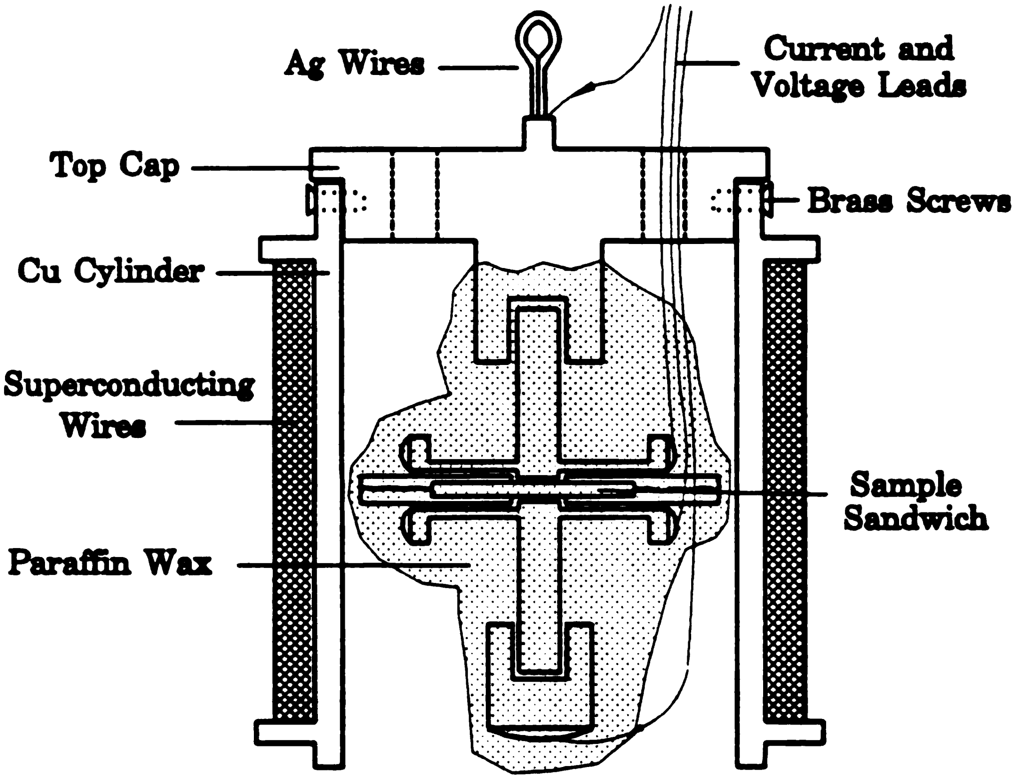

Figure 3.3: View of superconducting magnet with the sample sandwich.

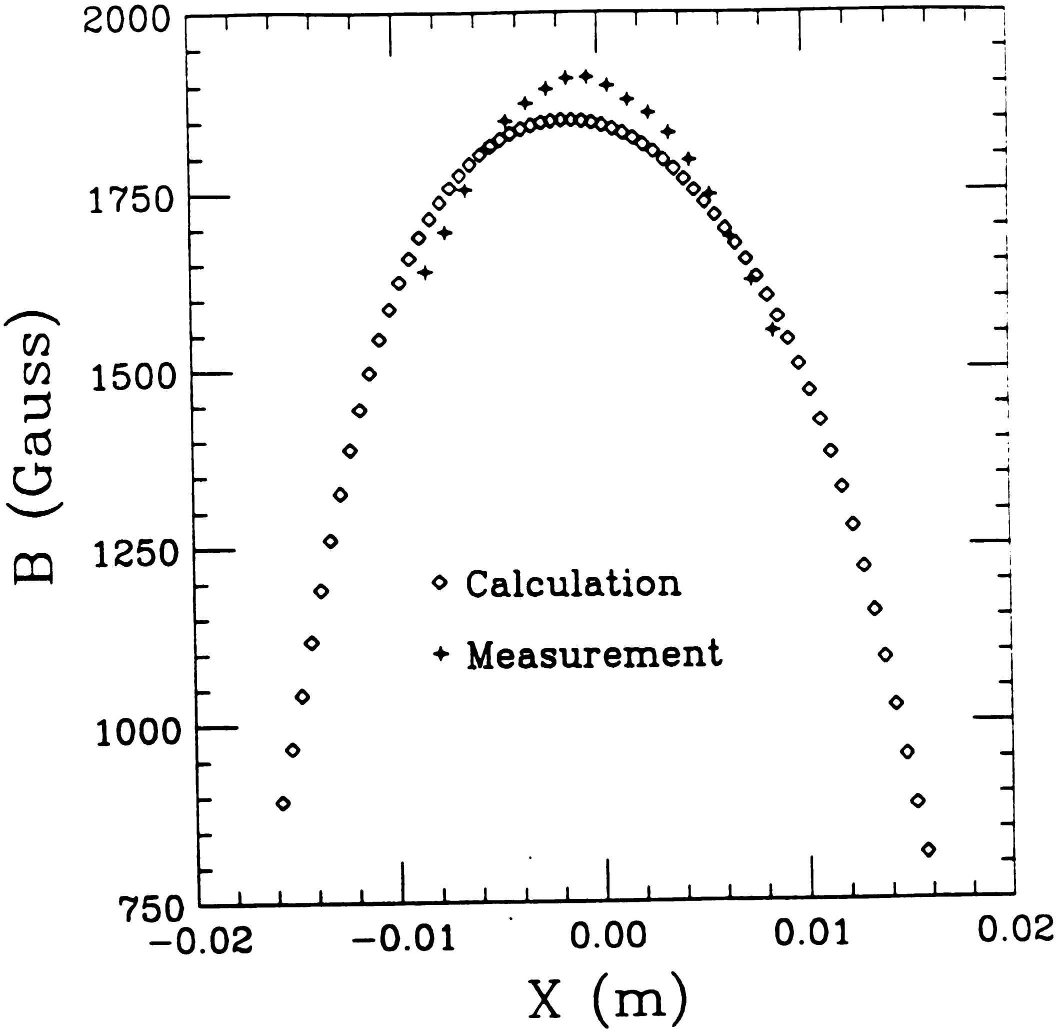

Figure 3.4: Magnetic fields produced by the magnet with I = 4A. X= 0 represents the center of symmetric axis of the Cu cylinder in Figure 3.3.

magnetometer. By applying 10mA of current, we measured the magnetic fields by inserting the probe of the magnetometer into the magnet. The scaled values of the measured magnetic field on the symmetric axis of the magnet cylinder are shown in Figure 3.4. The theoretical calculation is also shown in Figure 3.4, Good agreement is obtained, especially near the center of the magnet. Magnetic field (B) produced at the position of the CuTi ribbon is about 1900 Gauss with 4A of current.

3.2.5 Making and Mounting Samples

Sample preparation and mounting in our our experiment are pretty complicated and time consuming. It takes about 12 hours to make and mount a sample by hand. The procedure for making a sample is as follows:

1) The Cu electrodes, Cu caps, CuTi ribbon, press, and all other tools were cleaned in air with acetone and 200 proof alcohol. They were placed in a metal pan carpeted with a clean sheet of aluminum foil. Circular holes, with a diameter of 2.7mm, were cut in the centers of two pieces of square shaped insulating tape using a special drill. If necessary, the diameters of the holes could be changed by using different drills. With a specially designed press shown in Figure 3.5, the two pieces of the tape were aligned so that the two holes in their centers were exactly on opposite sides of the CuTi ribbon. Then they were stuck on each side of the CuTi ribbon, which also had a square shape. The size (3.5mm) of CuTi ribbon square was chosen to be smaller than that of insulating tape (6mm), so that the potassium on the both sides of the CuTi ribbon could not be electrically shorting

2) All the cleaned items and taped CuTi ribbon were now ready to be put into the Ar filled glove box. In order to outgas all these items, they were placed in the air lock of the glove box, then flushed with Ar, and pumped on for 2 hours. Before the sandwich was made, we waited another two hours to allow the purification system to remove any contamination brought with these items.

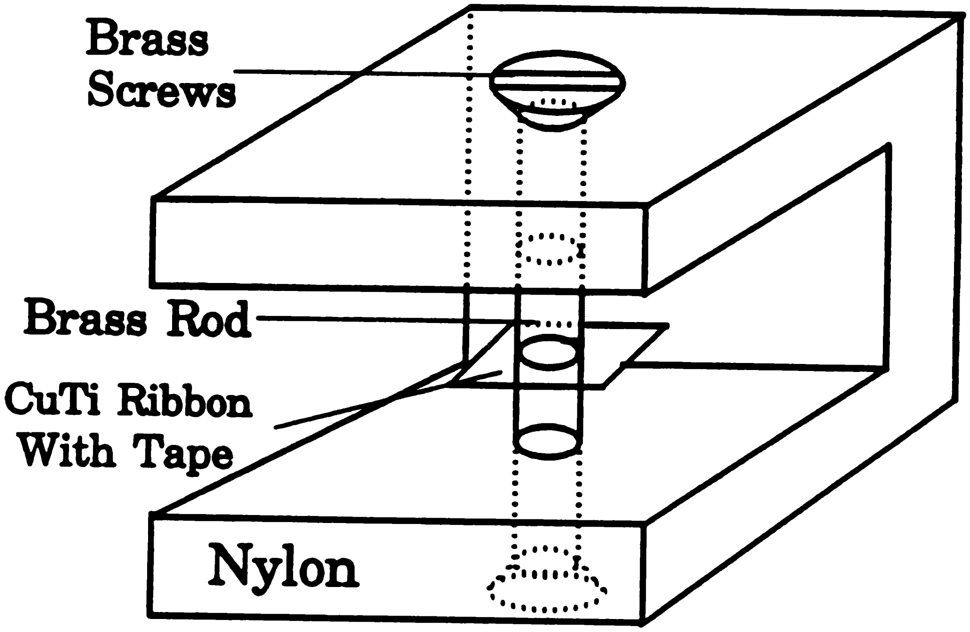

Figure 3.5: Press used for aligning holes and pressing the Cu electrodes

3) Surface oxide layers on the CuTi ribbon were removed with files for the naked CuTi ribbon and with knives for the Cu coated CuTi ribbon. The high purity potassium (RRR=1500), extruded from a stainless steel die, was immediately put on the cleaned surface. The same thing was done for the other side of the ribbon and for the Cu electrodes. Then the potassium coated Cu electrodes and CuTi ribbon were pressed together using the press. Next, the outside end of one electrode and the hole in the top cap were cleaned with knives, coated with potassium, and pressed together by hand. Because of the potassium inside the hole in the top cap, the electrode and the top cap were in excellent thermal and electrical contact. A similar procedure was used to mount the lower Cu cap onto the other Cu electrode. The total thickness of the potassium layers between the Cu electrodes and the CuTi ribbon, which contribute to the total resistance of the sandwich, is estimated to be less than 0.3mm. The sandwich was then dipped into melted paraffin wax and pulled out. After repeating this a few times, a layer of the paraffin wax with thickness of 1−2mm was formed around the sandwich. The paraffin layer will keep the potassium layers from oxidizing for a period of few hours while in the ambient atmosphere. The paraffin wax is a 1:4 mass-ratio mixture of standard paraffin wax and a special paraffin called n-Eicosane, made by Humphrey Chemical Company. This mixture has a melting point of 40°C, which is lower than that of potassium (65°C), so that potassium will not melt during the dipping. After the paraffin layer cooled down to room temperature (about 40 minutes), the sample sandwich was ready to be taken out from the glove box and tested.

4) The sample sandwich was tested with a stainless steel dip stick. A hollow nylon cylinder, attached to the bottom of the dip stick, was used for mounting the sandwich. The sample sandwich was placed into the hollow nylon cylinder, so that it was protected from accidently being hit. The cylinder with the sandwich was slowly dunked into liquid helium. The resistance of the sandwich at 4.2K was measured

using a current source and a nanovoltmeter. If the effective resistivity was about the same size as that of CuTi, the sample was declared good and was ready to be mounted on the dilution refrigerator. If the resistance was too small or too large in comparison to that of the CuTi, it indicated that either the Cu electrodes were electrically shorted by potassium or the contacts between CuTi, potassium, and Cu electrodes were bad. In either case, the sandwich was rebuilt.

The tested sample sandwich was warmed up slowly from 4.2K in a pure helium gas environment to prevent cracking of the paraffin. The magnet was attached to sandwich using three screws. Then the sample sandwich was mounted on the refrigerator as shown in Figure 3.6.

Since our SQUID null detector is very sensitive to voltage noise produced by a magnetic flux change in the circuit, relative vibrations of the sample, magnet and a superconducting shield on the inner vacuum can had to be minimized. In order to reduce these vibrations, the silver wire (spot welded on the top cap of the sample sandwich) was rigidly connected to the bottom mount of the dilution refrigerator. At the bottom of the magnet, the three stainless steel wires were tied to a stainless steel cylinder which was firmly connected to the refrigerator. Wires for the current and voltage leads were tied and varnished down to minimize vibrations. The inner vacuum can with μ metal and superconducting shield was mounted to minimize the external magnetic and electrical interference. This inner vacuum was rigidly attached to the still of the dilution refrigerator, which in turn was rigidly attached to the mixing chamber.

3.3 Thermometry

Since accurate temperature measurements are very critical in our experiment, several thermometers were used in the measurements. The temperatures of sample and

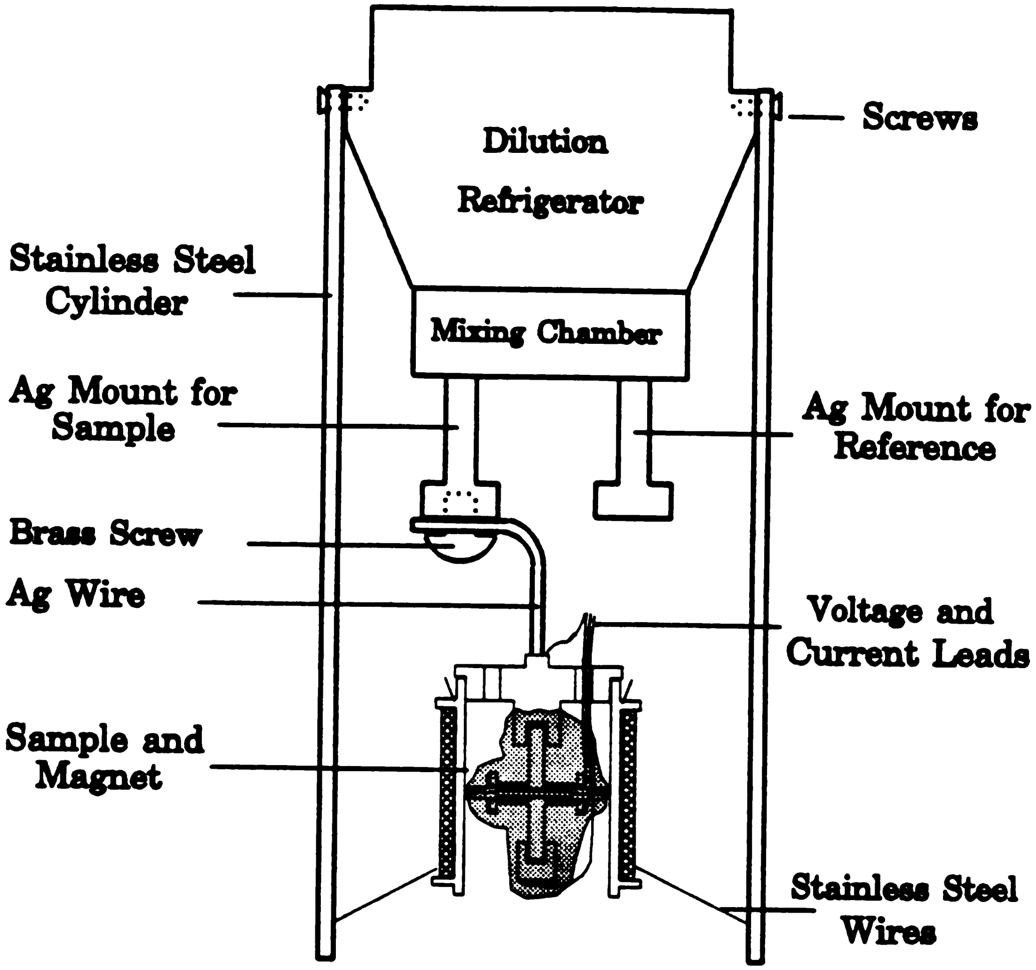

Figure 3.6: Mounting of sample

reference were measured by two germanium resistance thermometers, one carbon resistor, and two Cerrous Magnesium Nitrate(CMN) susceptibility thermometers (see Figure 3.8 and 3.6. The calibration of these thermometers was done by C. W. Lee and V. Heinen et al. [Hei 83]. The two germanium resistors were mounted in the holes of the bottom piece of the sample mount underneath the mixing chamber using Apiezon N grease for thermal contact. The susceptometers of the CMN thermometers were mounted against and thermally insulated from the plastic wall of the mixing chamber. Silver wires of 1-mm-diameter provide thermal contact between the bottom piece of the sample mount and both the CMN sensors and their susceptibility coils [Yin 87].

3.3.1 Sample Thermometers

Two germanium resistors called R_6, R_7, and a CMN thermometer called χ_{old} were used to measure the sample temperature. For temperature above approximately 1.5K, R_6 was used, which was a Lakeshore Cryotronics germanium resistor. For temperature between approximately 50mK and 1.5K, R_7, a Cryocal CR50 germanium resistor was used. The calibrations for R_6 and R_7 were done by Heinen [Hei 83]. Below approximately 50 mK, χ_{old} was used, which was a CMN thermometer [Hei 83, Yin 87]. For details, please see Heinen's thesis.

Since the susceptibility vs temperature for CMN obeys Curie's law, it follows a straight line on a plot χ vs $1/T$. Since χ_{old}, R_7, and R_6 are mounted in the same silver mount, they have the same temperature. Therefore χ_{old} was compared with R_7 and R_6 at the temperature above 50mK and calibrated as follows: χ_{old} and R_7, or χ_{old} and R_6 were recorded at the same temperature. The temperature was calculated from R_7 or R_6. Then we plotted χ_{old} vs $1/T$ and fitted Curie's law to the data using a least-square fitting program. The temperature below 50mK can be obtained by extrapolation of the fit of Curie's law. For more details, please see Appendix A.

3.3.2 Reference-Resistor Thermometers

As we discuss later, our high-precision resistance circuit requires a very stable reference resistor. A carbon resistor called R_{11} and a CMN thermometer called χ_{new}, were used for measuring reference-resistor temperature. Since the reference resistor has a resistance that is slightly temperature dependent, we needed to measure its temperature. At temperature above approximately 50mK, R_{11} was used, but its reciprocal, the conductance called C_{11}, was measured since we used an existing automatic conductance bridge for R_{11}.

For temperature below 50mK, χ_{new} was used since the CMN has a much better temperature response in this range. The calibration was done in exactly same way as for χ_{old}. A SQUID was employed to measure the susceptibilities of both χ_{old} and χ_{new} simultaneously. Details about the measurements can be found in V. Heinen and S. Yin theses [Hei 83, Yin 87].

The slight temperature dependence of the reference resistance can be calibrated as follows: Another resistor was installed as the new reference and was held at a constant temperature slightly above 4.2K. A germanium thermometer (R_5) was used to measure its temperature. Our old reference served as the "sample" and was measured as a function of C_{11} for $T \leq 4.2$K. The relation between R_{ref} and C_{11} is shown in Figure 3.7. The data were fitted using the empirical equation

$$R = R_0 + \frac{A_1}{(A_2 - C_{11})^N} \tag{3.1}$$

From the fit (solid curve in Figure 3.7), R_{ref} was corrected to an precision of $\Delta R/R \leq$ 0.6ppm. More details about the data and fitting parameters can be found in Appendix B.

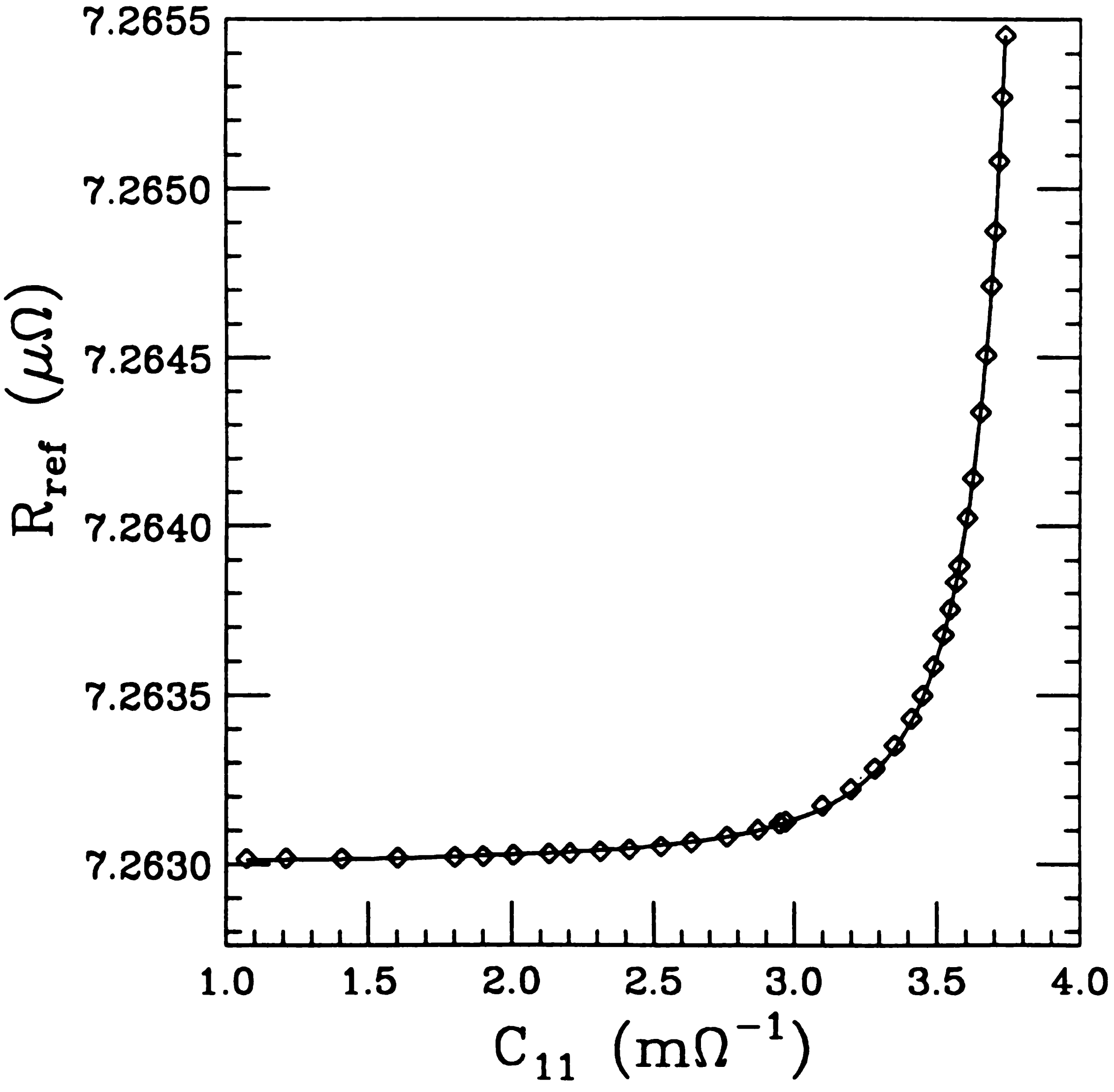

Figure 3.7: R_{ref} vs. C_{11}

3.4 Measurements

This section is intended to explain how the zero-field electrical resistance and magnetoresistances of the samples were measured.

3.4.1 Resistance Measurement ($B = 0$)

First, we measured the resistivities of CuTi ribbons at room and liquid He temperatures. The measurement was done by passing a current I parallel to the ribbons and measuring the voltage V across two points separated by a distance a. The length a, width b, and thickness t of the ribbon were measured with a micrometer (precision 0.0001 inch), giving for the resistivity of the CuTi ribbon

$$\rho = \frac{Rbt}{a} \tag{3.2}$$

Once the sample was mounted on the refrigerator and cooled to 4.2K or lower, the circuit shown in Figure 3.8 was used. This low temperature potentiometer circuit consists of the SQUID null detector and the two resistors, R_x and R_{ref}. R_x is the sample resistor to be measured and R_{ref} is a dilute Cu(Ag) alloy resistor mentioned in Section 3.3.2. The wires connecting these resistors are made of Niomax CN, a multi-filament Nb-Ti superconducting wire with Cu-Ni cladding made by Imperial Metal Industries. To minimize the noise introduced by stray magnetic fields, most of the wires except those near the sample were shielded in superconducting lead-tubing. The wires leading to the sample were all carefully tied or varnished down to reduce magnetically induced currents and heating due to vibrations.

In this experiment, we did not measure a sample resistance directly, but instead we measured its ratio with respect to a reference resistance in order to use our high precision current comparator. The reference resistor is made from a dilute Cu(Ag) alloy and has a 4.2K resistance of $7.26\mu\Omega$. The resistance ratio C was measured by

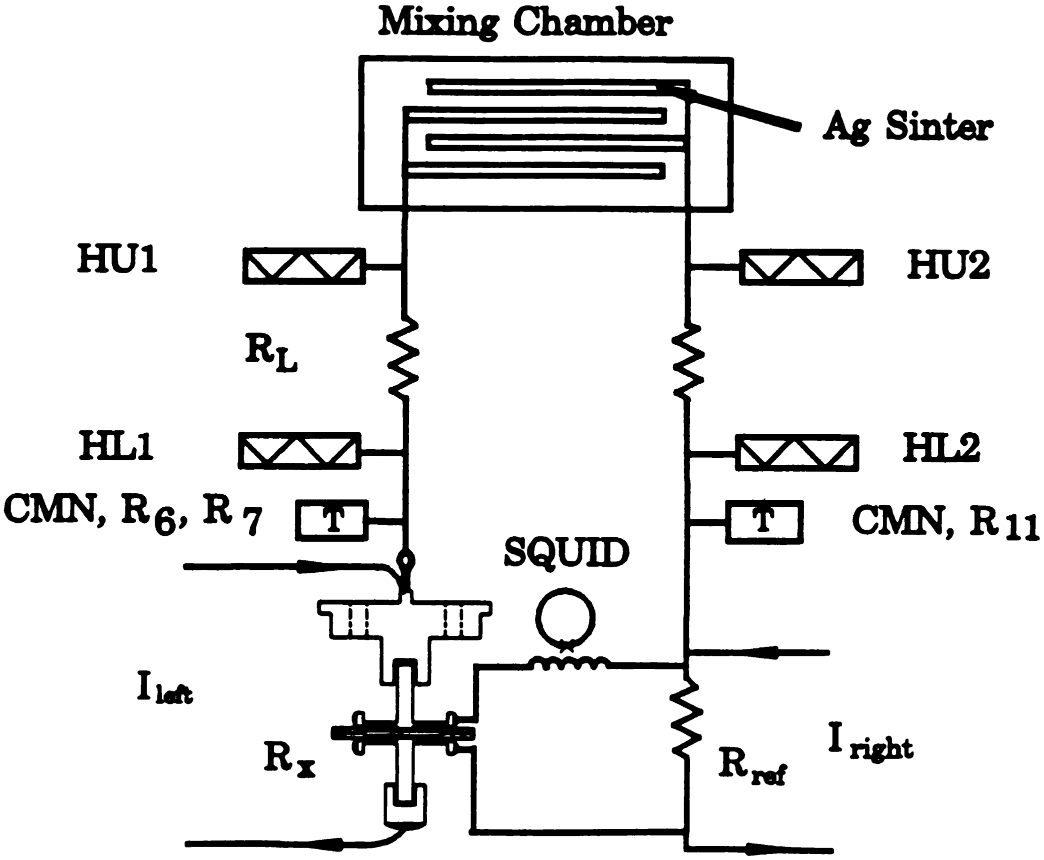

Figure 3.8: Low temperature circuit

using the current comparator together with the SQUID as the null detector mentioned in Section 3.1.2. The current comparator generates two currents I_m and I_s with the ratio $C = I_s/I_m$ being stable to better than 0.1ppm precision. When comparing resistances, one current I_m passes through the master side resistor R_m (either R_x or R_{ref}) and the other current I_s passes through the slave side resistor R_s. Since I_m is greater than I_s, R_m must be less than R_s. The master side current can be ramped slowly to a predetermined value. The slave side current is CI_m where C is the switch setting of current comparator. C is adjusted until the SQUID output signal indicates a null condition at its input.

Any thermal electro-motive forces (EMFs) generated in the circuit can be eliminated by the following procedure. Let V_s be a stray voltage in the circuit due to a thermal EMF. Then for the current going one direction, the SQUID measures

$$V(+) = I_sR_s - I_mR_m + V_s \quad . \tag{3.3}$$

When one reverses the current, one has

$$V(-) = -I_sR_s + I_mR_m + V_s \quad . \tag{3.4}$$

When C is adjusted until $V(+) = V(-)$, one gets

$$I_sR_s - I_mR_m + V_s = I_sR_s - I_mR_m + V_s \quad . \tag{3.5}$$

Finally one obtains

$$\frac{I_s}{I_m} = \frac{R_m}{R_s} = C \quad , \tag{3.6}$$

which is independent of V_s. Once we obtain C, the resistance of the sample can be calculated from the above equation, where $C = R_x/R_{ref}$ or its reciprocal.

The temperature dependent resistance was measured in the following ways: For temperatures above 1.5K, the sample temperature was regulated at a desired value by regulating on R_6 through the mixing chamber heater. When C_{11}, which indicated the reference temperature, reached a stable value, it was recorded; and C was obtained by balancing the SQUID. For temperature below 1.5K, we cooled the sample directly to the lowest possible temperature ($\approx$15mK). Then we took the measurements while warming up. For temperature below 50mK, χ_{new} (reference temperature) was regulated through the mixing chamber heater, and χ_{old} was used to measure the sample temperature. When χ_{old} was stable enough, χ_{new}, χ_{old}, and C were recorded. For temperatures above 50mK, C_{11} was used for the regulation, and R_7 was used for measuring the sample temperature. Following the same procedure, R_7, C_{11}, and C were obtained. Once we know C_{11}, the resistance of the reference resistor can be corrected using the fit given in Figure 3.7.

Since the reference resistance is temperature dependent, this problem can be solved by measuring the differential of the sample resistance with respect to its temperature while keeping the reference temperature constant. A thermal link (R_L) between the refrigerator and the silver mount was used to produced the temperature difference easily (see Figure 3.8). The procedure is as follows: We keep the reference temperature (T_{ref}) constant by regulating it through C_{11} for $T \geq 50$mK and χ_{new} for $T \leq 50$mK. Then we apply a steady current to the lower left heater (L1) in the sample side and measure C at that temperature. Next we increase the power to the L1 heater so the sample temperature rises to $T + \Delta T$ and C is adjusted to $C + \Delta C$ to balance the SQUID. Here C is defined as

$$C = \frac{R_x}{R_{ref}} \quad . \tag{3.7}$$

Because the reference temperature is kept at a constant temperature T_{ref}, we have

$$\Delta C = \frac{\Delta R_x}{R_{ref}} \quad . \tag{3.8}$$

Hence

$$\frac{\Delta C}{C \Delta T} = \frac{\Delta R_x}{R_x \Delta T} \quad . \tag{3.9}$$

If ΔT is small enough, this leads to

$$\frac{\Delta C}{C\Delta T} \Longrightarrow \frac{d\rho}{\rho dT} . \tag{3.10}$$

The thermoelectric ratio can be measured using the above circuit if we put a G heater onto the bottom of the sample sandwich (see Figure 3.2). For details, please see Yin's thesis [Yin 87].

3.4.2 Magnetoresistance Measurement

The magnetoresistance (MR) measurements were performed in the same way as for the zero-field resistance. Figure 3.9 shows the circuit for applying magnetic fields.

Since the sample was mounted at the bottom of the refrigerator, two single-filament NbTi superconducting wires connected the magnet via polyethylene tubing to a superconducting persistent switch (SPS) located at the top of the outer vacuum can. In order to prevent heat flow from the SPS near 4K to the 1K pot and from 1K pot to the sample, the Cu cladding on the superconducting wires connected between the SPS and the sample was etched away except in one place near the 1K pot where the electrical connection was made for applying current to the magnet from a external current source. The SPS is made of a single filament superconducting wire wound on a heater (called SPS heater) which has weak thermal connection to the 4K bath via a piece of brass. To make a superconducting connection, the wires from the SPS and the wires from the magnet were mechanically pressed onto two superconducting Nb strips with six screws.

At a fixed temperature, the procedure for a magnetoresistance measurement is as follows: First we apply 1.5 Volts to the SPS heater, so that the superconducting wires wound on the heater become normal. Then we slowly apply a current to the superconducting magnet. Once the desired current is reached, we turn off the power to SPS heater, and the SPS becomes "closed". Next we slowly reduce the source

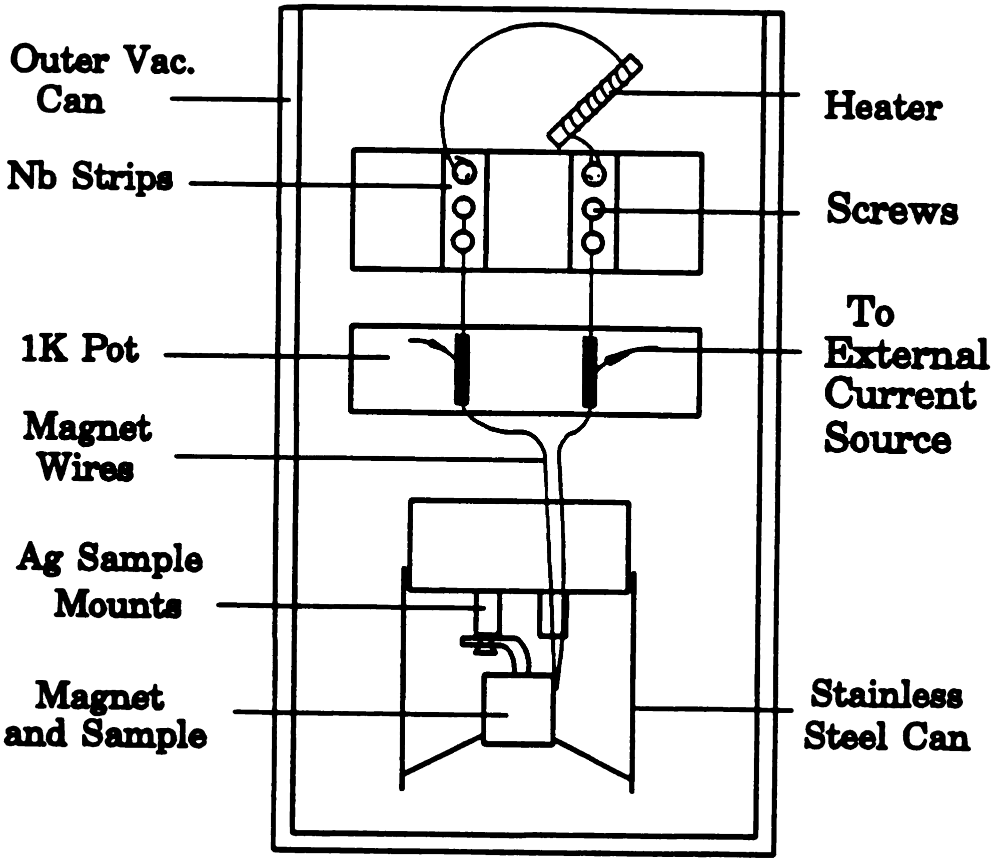

Figure 3.9: Circuit for MR measurement

current for the magnet to zero and turn off the power supply. The magnet and SPS are all in a superconducting state so a very stable persistent current flows through magnet coil. Then temperatures and resistance ratio C can be obtained using the procedures described in Section 3.4.1.

We made magnetoresistance measurements only at the following sample temperatures: 4.2K, 1K, 0.5K, 0.25K, 0.1K, 52mK, and 20mK.

The heat generated by eddy currents during energizing and de-energizing of the magnet is significant only at temperature below 50mK. In order not to heat the sample too much ($\Delta T < 1$mK), the time rate of change of the current was set to less than 10mA/s. A more detailed discussion of eddy currents will be given in Section 3.6.

3.5 Residual and Boundary Resistances

Both the Cu electrodes, the K glue, and various boundaries can contribute a background resistance to the total resistance of our CuTi sandwich that might mask the actual resistance of the CuTi sample. In Section 4.2.1, we will show that these background resistances are not a problem and in most circumstances can be ignored or at least corrected for.

3.6 Heat Generated in our Samples

A major heating problem during the measurements is caused by eddy currents during energizing and de-energizing the magnet. When the current in the magnet changes, currents are induced in Cu cylinder of the magnet and in the top cap of the sandwich, which then produce Joule heating. At $T < 50$mK, this heating might significantly warm up the sample, and it might take a long time to cool back down. To limit this cooling time to less than one minute, we restricted the temperature increase to

$\Delta T < 1\text{mK}$ at $T = 15\text{mK}$. Let $\dot{Q}$ be the heat flow through the thermal link R_L, then

$$\dot{Q} \leq \frac{\Delta T}{W} \,, \tag{3.11}$$

where W is the thermal resistance of R_L. According the Wiedemann-Franz law, we have

$$W = \frac{R_L}{LT} \,, \tag{3.12}$$

where L is Lorenz constant (2.45×10^{-8}). Since $R_L = 50\mu\Omega$, $\dot{Q}$ is 8nW. For the hollow Cu cylinder, the relationship between the change rate of B and the heat flow $\dot{Q}$ is given by

$$\frac{dB}{dt} = \left(\frac{2\rho \dot{Q}}{\pi l (b^4 - a^4)} \right)^{1/2} \,, \tag{3.13}$$

where l is the length of the Cu cylinder, a, b are the inner and outer radii of the cylinder, and ρ is the resistivity of Cu for $T < 4.2\text{K}$. We obtain $dB/dt \leq 5$ (Gauss/s). Since B is proportional to the magnet current I, we have $dI/dt \leq 10$ (mA/s).

Chapter 4

Experimental Results

In this chapter, we will present and discuss the measured electrical and magnetoresistances of the amorphous $Cu_{50}Ti_{50}$ and $Cu_{60}Ti_{40}$ ribbons at temperatures between 15mK and 6.0K and in magnetic fields up to 0.2 Tesla. Possible systematic errors in both zero field and $B \neq 0$ resistance measurements will be discussed and taken account of. The theoretical models given in Chapter 2 will be fitted to the data. The superconducting proximity effects at low temperatures and electron phonon Umklapp contributions to the resistivity at the temperature above 3K will also be discussed.

4.1 Sample Information

Since our samples are sandwich-like as shown in Figure 3.2, the total measured resistance of a sandwich includes the contributions from the K layers, the Cu electrodes, the CuTi ribbons, and their boundaries. The contributions from the K layers, Cu electrodes, and the boundaries are called background contributions. Even if they are very small in comparison to those of the CuTi ribbons in the sense of absolute resistance, they may affect the temperature or magnetic field dependences of the resistances dramatically because the resistances of the CuTi ribbons only change by less than about 0.2% between 4K and 15mK and by 0.02% between 0T and 0.15T. In order to measure the resistances of CuTi ribbons accurately, we have to quantify these background contributions and correct for them if necessary. Therefore, we have measured a series of $Cu_{50}Ti_{50}$ and $Cu_{60}Ti_{40}$ ribbons with different sample preparation conditions. A few sandwiches without CuTi ribbons were also measured. Table 4.1 lists the preparation conditions for the sandwiches with CuTi ribbons. The samples, which were originally about $30-40\mu m$ thick, were thinned to various thicknesses with sandpaper. The thicknesses were measured with a micrometer with an uncertainty of about $1\mu m$. The contact areas are the areas of the holes in the two pieces of insulating tape, which were used for the contacts between K and CuTi ribbons as described in Section 3.2.2. The actual areas may differ by a few percent, but this does not matter because only relative changes of resistances are important. The Ion Milling and Cu Sputtering columns in Table 4.1 indicate how the surface of each CuTi sample was prepared, as described in Section 3.2.3. Some of the samples used bare CuTi ribbons and they are listed as "No" under these columns.

Since two Cu electrodes, which are used as both current and voltage leads in our sandwich, were glued to both sides of the CuTi ribbons with K, the Cu electrodes and K layers do contribute to the total resistances. In our measurements, several Cu electrodes have been used. In order to study their contributions to both the zero field resistances and magnetoresistances, we made some Cu/K/Cu sandwiches by gluing only the Cu electrodes together with K.

Table 4.2 shows the preparation conditions for these sandwiches. The contact areas have the same meaning as in the Table 4.1. Samples KCu-3, 4, and 5 are made of unannealed OFHC copper, which has the RRR about 100 and exhibits a Kondo effect [Kon 64] below about 1K, as shown in Figure 4.2 and discussed later. Thus there are some magnetic impurities in the OFHC copper. To reduce the Kondo contributions, the OFHC copper was oxygen annealed at 950°C and 4.8×10^{-4} torr for four days before the Cu electrodes were machined. The RRR for the annealed Cu was 375. The Cu electrodes used in samples KCu-7, 9, and 10 were made from

Table 4.1: CuTi Sample Preparation Conditions

Samples	Thickness (μm)	Contact Area (cm^2)	Ion Milling Vb,Va,t [a]	Cu Sputtering Vt,D,t [b]
KCu$_{50}$Ti$_{50}$Cu-1	43	0.080	No	No
KCu$_{50}$Ti$_{50}$Cu-2	43	0.080	No	No
KCu$_{50}$Ti$_{50}$Cu-7	36	0.080	No	No
KCu$_{50}$Ti$_{50}$Cu-8	36	0.080	No	No
KCu$_{50}$Ti$_{50}$Cu-9	36	0.080	No	No
KCu$_{50}$Ti$_{50}$Cu-10	25	0.080	No	No
KCu$_{50}$Ti$_{50}$Cu-11	36	0.080	No	No
KCu$_{50}$Ti$_{50}$Cu-12	38	0.058	Vb=600V Va=60V t=10min Ib=6.0mA	Vt=400V t=400s D=5000Å
KCu$_{50}$Ti$_{50}$Cu-13	18	0.061	Vb=650V Va=50V t=30s Ib=10.0mA	Vt=400V t=240s D=3000Å
KCu$_{50}$Ti$_{50}$Cu-15	30	0.057	Vb=600V Va=50V t=80s Ib=4.0mA	Vt=400V t=240s D=3000Å
KCu$_{50}$Ti$_{50}$Cu-16	30	0.057	Vb=600V Va=50V t=80s Ib=4.0mA	Vt=400V t=240s D=3000Å
KCu$_{60}$Ti$_{40}$Cu-1	42	0.058	No	No
KCu$_{60}$Ti$_{40}$Cu-2	36	0.059	Vb=600V Va=50V t=4min Ib=6.0mA	Vt=400V t=180s D=2500Å
KCu$_{60}$Ti$_{40}$Cu-3	16	0.059	Vb=600V Va=50V t=4min Ib=6.0mA	Vt=400V t=180s D=2500Å
KCu$_{60}$Ti$_{40}$Cu-4	20	0.059	Vb=700V Va=57V t=4min Ib=5.0mA	Vt=00V t=260s D=3500Å
KCu$_{60}$Ti$_{40}$Cu-5	27	0.059	Vb=700V Va=57V t=4min Ib=5.0mA	Vt=400V t=260s D=3500Å
KCu$_{60}$Ti$_{40}$Cu-6	18	0.062	Vb=650V Va=50V t=30s Ib=10.0mA	Vt=400V t=240s D=3000Å
KCu$_{60}$Ti$_{40}$Cu-7	31	0.058	Vb=640V Va=50V t=80s Ib=4.1mA	Vt=400V t=220s D=3000Å

[a]) Vb: ion beam voltage, Ib: ion beam current, and t: time of the ion milling.

[b]) Vt: target voltage, t: time of Cu sputtering, and D: thickness of Cu overlayer.

Table 4.2: Cu/K/Cu Sandwich Preparation Conditions

Samples	Contact Area(cm^2)	O$_2$ Annealing	RRR	Ni Plating	used in Sandwiches
KCu-3	0.080	No	106	No	KCu$_{50}$Ti$_{50}$Cu-1,2,7
KCu-4	0.080	No	106	Yes	KCu$_{50}$Ti$_{50}$Cu-8
KCu-5	0.080	No	106	Yes	KCu$_{50}$Ti$_{50}$Cu-9,10
KCu-7	0.080	Yes	375	Yes	KCu$_{50}$Ti$_{50}$Cu-11,12,13 KCu$_{60}$Ti$_{40}$Cu-1,2,3,4,5,6
KCu-9	0.080	Yes	375	Yes	KCu$_{50}$Ti$_{50}$Cu-14,15,16 KCu$_{60}$Ti$_{40}$Cu-7,8
KCu-10 [a]	0.080	Yes	375	Yes	

[a]) Same Cu electrodes as KCu-9, but with much thicker layer (1 – 2mm) of K for checking its contribution to magnetoresistances.

the annealed Cu. No Kondo effects were observed in these sandwiches, as shown in Figure 4.2.

In order to obtain high sensitivity in our measurements, the resistance of the voltage leads should be minimized. So superconducting Pb(Sn) solder was put around the leads before the superconducting wires were soldered on (see Figure 3.2). Because of the superconducting proximity effect [Mot 89], part of these leads may become superconducting at very low temperature. Figure 4.1 shows the measured resistances of sample KCu-3 between 40mK and 6K with 10mA and 50mA currents. The very rapid drop of the resistances below 0.4K indicates that the KCu sandwich was becoming superconducting, which is due to the solder. The rather strong current dependences of the resistances in the same temperature range also indicate the presence of this proximity effect. To prevent this effect, the edges of the voltage leads of the Cu electrodes were plated with ferromagnetic nickel before solder was put on the leads. Note that the nickel plated KCu-4 sample in Figure 4.1 shows no proximity effect. The same is true for all the nickel plated sandwiches shown in Figure 4.2.

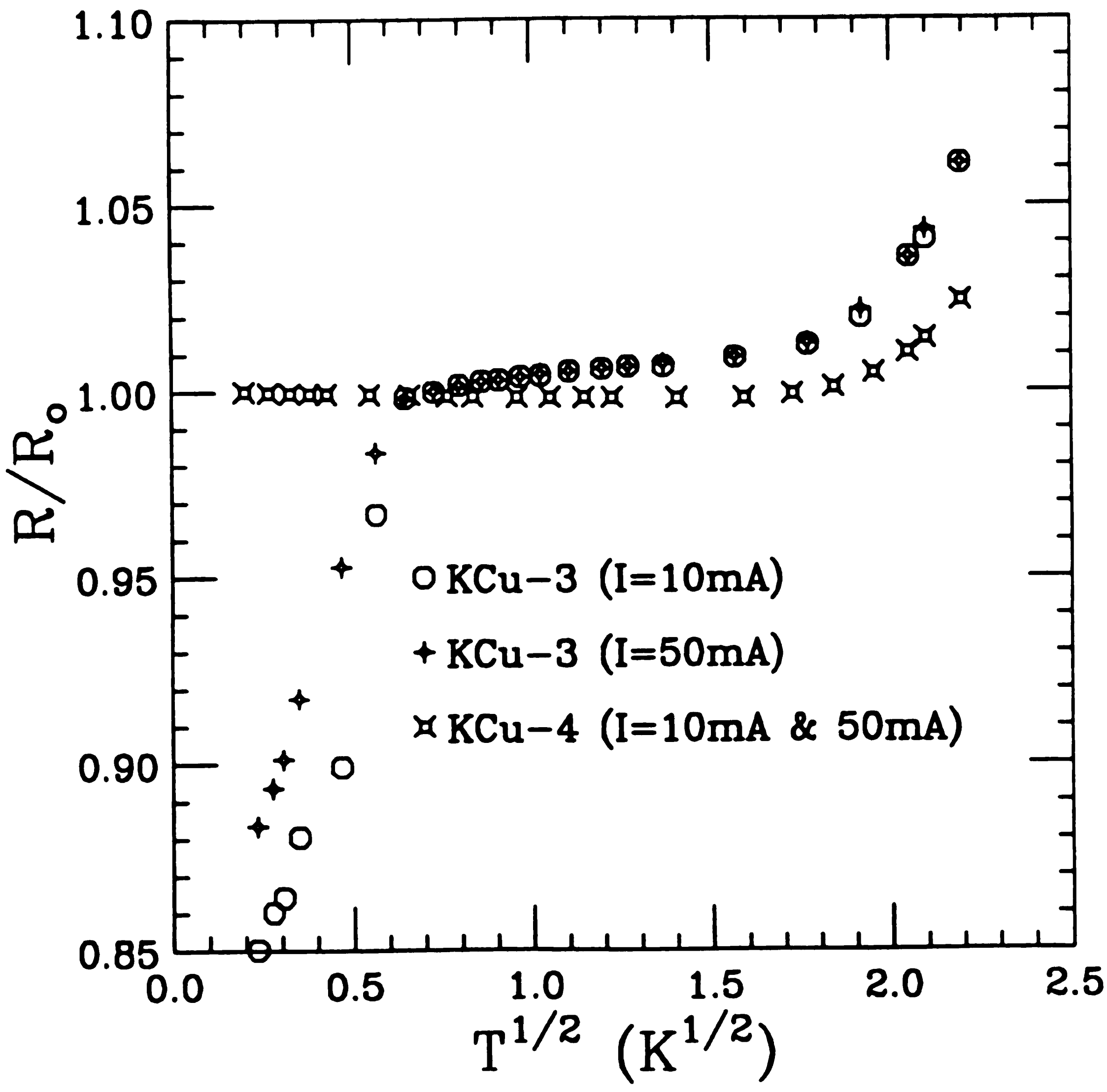

Figure 4.1: The superconducting proximity effects in the Cu electrodes.

4.2 Temperature Dependences of the Zero Field Resistivities

In this section, we will present and discuss the temperature dependences of the resistivities of CuTi ribbons at zero magnetic field. The temperature dependences of the resistivities at finite magnetic field will also be briefly described.

4.2.1 Background Resistances

As mentioned before, the background contributions to the resistance of a CuTi sandwich basically have two parts: Resistances of a Cu/K/Cu sandwich and of the boundaries between Cu and CuTi or K and CuTi. Although in this section we will analyse these background resistance in detail, we state at the outset that their magnitudes and temperature dependences are negligible in comparison to those of our CuTi ribbons for $T < 3\mathrm{K}$ in zero field.

As discussed in Chapter 2, the resistance of a crystalline metal is due to scattering of electrons from impurities, defects, other electrons, and phonons. Usually electron impurity scattering produces a temperature independent contribution. Electron-electron scattering gives a T^2 dependence, but it is usually very small in magnitude. Above about 1K, usually the most temperature dependent part of the resistivity comes from two electron-phonon scattering processes: normal and Umklapp. For pure K at temperature below 5K, its resistivity has the form [Hae 83].

$$\rho_{\mathrm{K}} = \rho_o + AT\exp(-\Theta_{\mathrm{K}}/T) \ , \tag{4.1}$$

where the last term on the right hand side is due to the electron phonon Umklapp process, Θ_{K} is an effective Debye-like temperature ($\simeq$20.3K), and ρ_o is the residual resistivity due to the electron impurity or defect scattering. For $T > 1\mathrm{K}$, the electron-electron interaction T^2 term is negligible in comparison to the Umklapp term.

For pure Cu, normal electron phonon scattering is significant. Theoretically it is proportional to T^5 for $T \ll \Theta_{\mathrm{Cu}} = 320\mathrm{K}$ [Zim 60, Ros 65], but experiments [Ste 81] show a T^4 dependence for 2K< T < 7K. That is, the resistivity of pure Cu obeys

$$\rho_{\mathrm{Cu}} = \rho_o + CT^4 \ . \tag{4.2}$$

The first part of the background contributions to the resistances of the CuTi sandwiches is determined from the Cu/K/Cu sandwich data shown in Figure 4.2. The data are taken between 15mK and 6K, and their ordinates are shifted by a constant value for clarity. The dotted line represents the resistivity of a pure K sample which has the same ρ_o as in our sandwiches. The resistances of the Cu/K/Cu sandwiches show similar behaviour to that of the pure K. For T < 3K, these resistances are nearly constant, as expected. The slight increases at very low temperature for KCu-4 and KCu-5 are due to the previously-mentioned Kondo effect. The Kondo contribution gives a resistance proportional to $-\ln(T)$ at low temperature. However, the sandwiches KCu-7 and KCu-10 show no resistance increase even at the lowest temperature since the Cu electrodes used in these two sandwiches were made of oxygen-annealed OFHC Cu. For T > 3K, the increases in resistance with increasing temperature are due to electron phonon interactions in the K and Cu. Since these sandwiches were Ni plated, there is no superconducting proximity effects even at 15mK. Finally, we will show in Figure 4.6 that the temperature dependence of the Cu/K/Cu sandwich resistance is negligible in comparison to that of the CuTi samples for T < 3K. Therefore our Cu-electrode system is reliable at least down to 15mK.

The residual resistance of a Cu/K/Cu sandwich is the order of $20-30\mathrm{n}\Omega$, which is negligible compared to the typical $10\mu\Omega$ resistance of the CuTi sample. The resistance of a Cu/K/Cu sandwich has three sources: the Cu electrodes, the K layers, and their boundaries. To estimate the three contributions for the sample KCu-7, let us first calculate the resistance due to the Cu electrodes. Since the total thickness of the

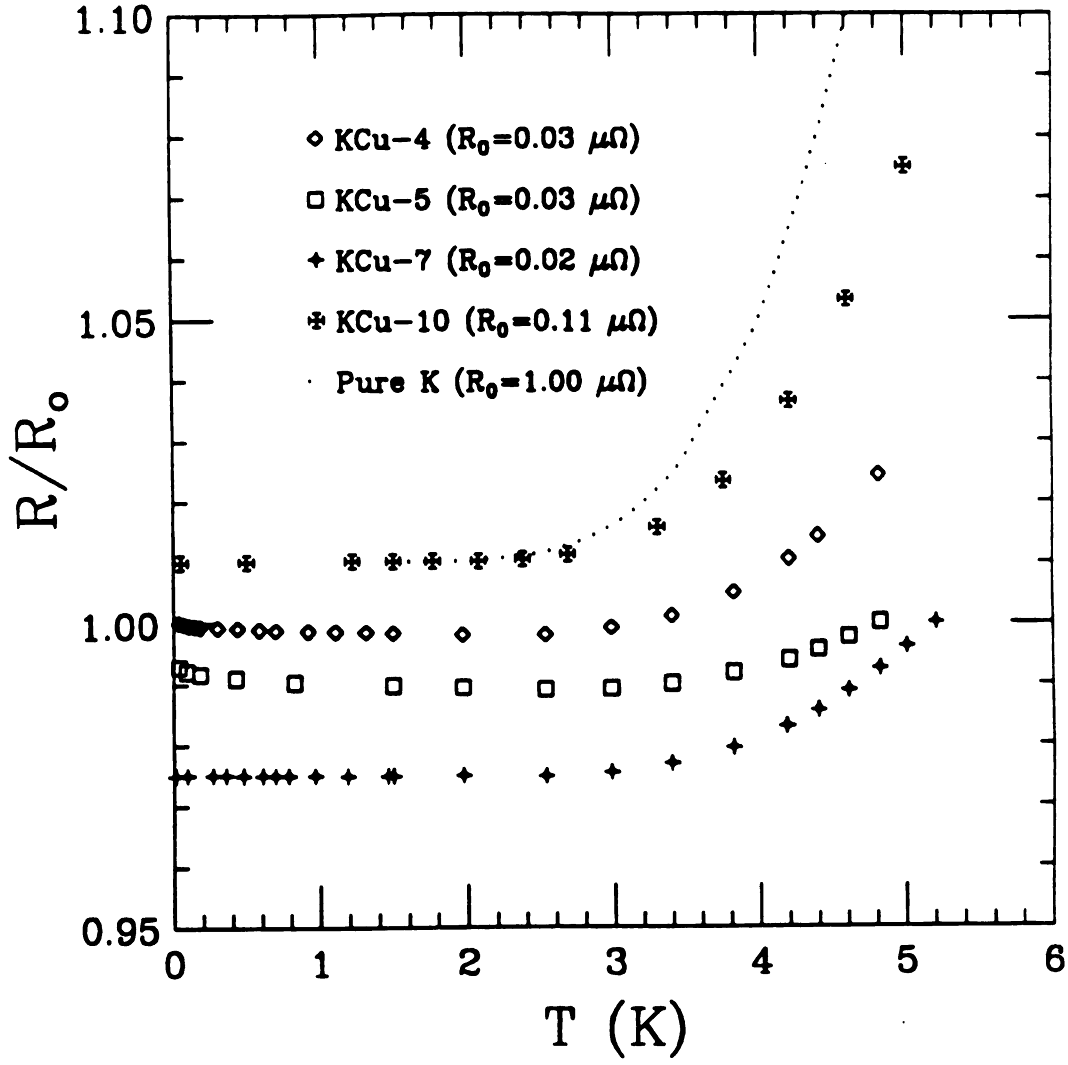

Figure 4.2: Normalized resistances of the Cu/K/Cu sandwiches and the pure K for $T < 6$K. The data have been displaced along ordinate for clarity.

Cu electrodes that contributes to the resistance is about 0.03cm, the area is 0.08cm^2, and the resistivity of the Cu electrode at 4.2K is about 5nΩcm, the total resistances due to the Cu electrodes is the order of 2nΩ, which is very small compared to the total resistance of the sandwich (20nΩ). The contribution from the K layer can be calculated in the same way. The thickness of the K layers varies from sample to sample and is not exactly known. It is estimated the thickness is of the order of 0.03cm. Since the resistivity of our K at 4.2K is the order of 4nΩcm and its area is same as that of Cu electrodes, the resistance from the K layers is about 1.5nΩ. Thus the total boundary resistance between Cu and K is estimated to be <17nΩ depending the quality of the contacts between Cu and K on the boundaries.

The most interesting resistances in our Cu/K/Cu measurements are the temperature dependent resistances, which also have three sources: Cu, K, and their boundaries. To estimate these, we redraw the Figure 4.2 in the manner shown in Figure 4.3. From Equation 4.1, we know that if K dominates the temperature dependent part of the sandwich resistances, we should see linear dependences for $\ln(\Delta\rho/T)$ vs $1/T$ in Figure 4.3. Indeed we see that all the data follow straight lines of negative slope that are parallel to that of the pure K sample (dotted line). We also fitted the data to Equation 4.1 and 4.2 using a least-squares fit, and we we got much better fit with Equation 4.1. Therefore we know that the Cu does not contribute significantly to the temperature dependent resistance. However, at this point we do not know if the temperature dependence is dominated by the d = 0.03cm-thick K or a "K-like" K/Cu boundary resistance. To resolve this uncertainty, we scaled the pure-K data (dotted line) in Figure 4.3 to conform to the case of a K layer with d = 0.03cm and A = 0.08cm^2 (dashed line). Since the dashed line agrees reasonably well with the KCu-5 and KCu-7 data, we conclude for these samples that the K-layer dominates. Note, however, that the KCu-4 sandwich exhibits a temperature dependence that is about 2.5 times larger than for the K layer. Thus this sample appears to have a signif-

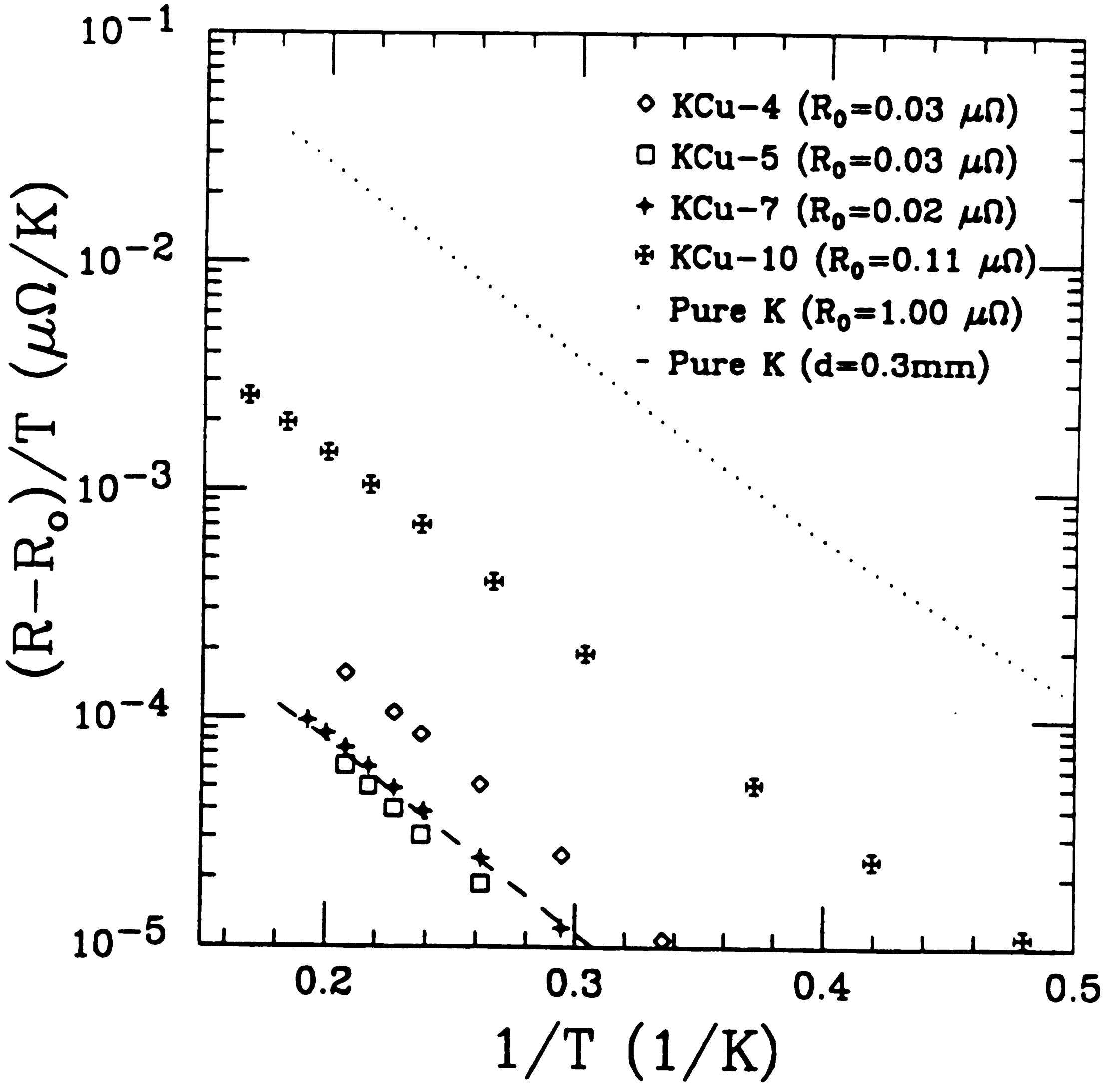

Figure 4.3: Temperature dependent resistances of the Cu/K/Cu sandwiches.

icant K/Cu boundary contribution, perhaps due to a severely reduced effective area of contact between the K and Cu. Hence, there remains some uncertainty about the relative importance of the "bulk" and " boundary" contribution for K. Fortunately, it is really of no consequence because, as we show later in Figure 4.6 and 4.9, the temperature dependence of the Cu/K/Cu-sandwich total resistance is negligible in comparison to that of our CuTi ribbons for $T \leq 3$K.

However, at this point, we do not know if the temperature dependence of the resistance between K and CuTi or between Cu and CuTi is also negligible. To estimate this resistance, we measured the resistances of the CuTi sandwiches with different CuTi ribbon thicknesses. Because the sandwiches with different CuTi ribbon thicknesses have the same number and kinds of boundaries, the resistances due to these boundaries should be very similar. If these boundary resistances have large enough temperature dependences, the temperature dependence of total relative resistance of the sandwich will depend upon the thickness of the CuTi ribbon.

Figure 4.4 and 4.5 show that temperature dependences of relative resistances for the $KCu_{50}Ti_{50}Cu$ and $KCu_{60}Ti_{40}Cu$ sandwiches with various CuTi ribbon thicknesses.

For the $KCu_{50}Ti_{50}Cu$ sandwiches shown in the Figure 4.4, with $T < 3$K, the behaviors of the data for the sandwiches $KCu_{50}Ti_{50}Cu$-12 and 13, which have CuTi ribbon thicknesses of about 38μm and 18μm, respectively, are almost the same. With the same CuTi ribbon thickness, the Cu coated sandwich $KCu_{50}Ti_{50}Cu$-12 shows the same relative resistance behavior as the non Cu coated sample $KCu_{50}Ti_{50}Cu$-11. Although the thicknesses of K layers in these sandwiches may differ, from Figure 4.2 we know that the K layers contribute only very small constant resistances for $T < 3$K and thus will not affect the behaviors of the data for the CuTi sandwiches. Since we plot $\Delta R/R_o$ vs $\sqrt{T}$, the absolute resistances due to the boundaries must also be very small in comparison to that of CuTi ribbons, otherwise the shapes of the curves in the Figure 4.5 will be changed.

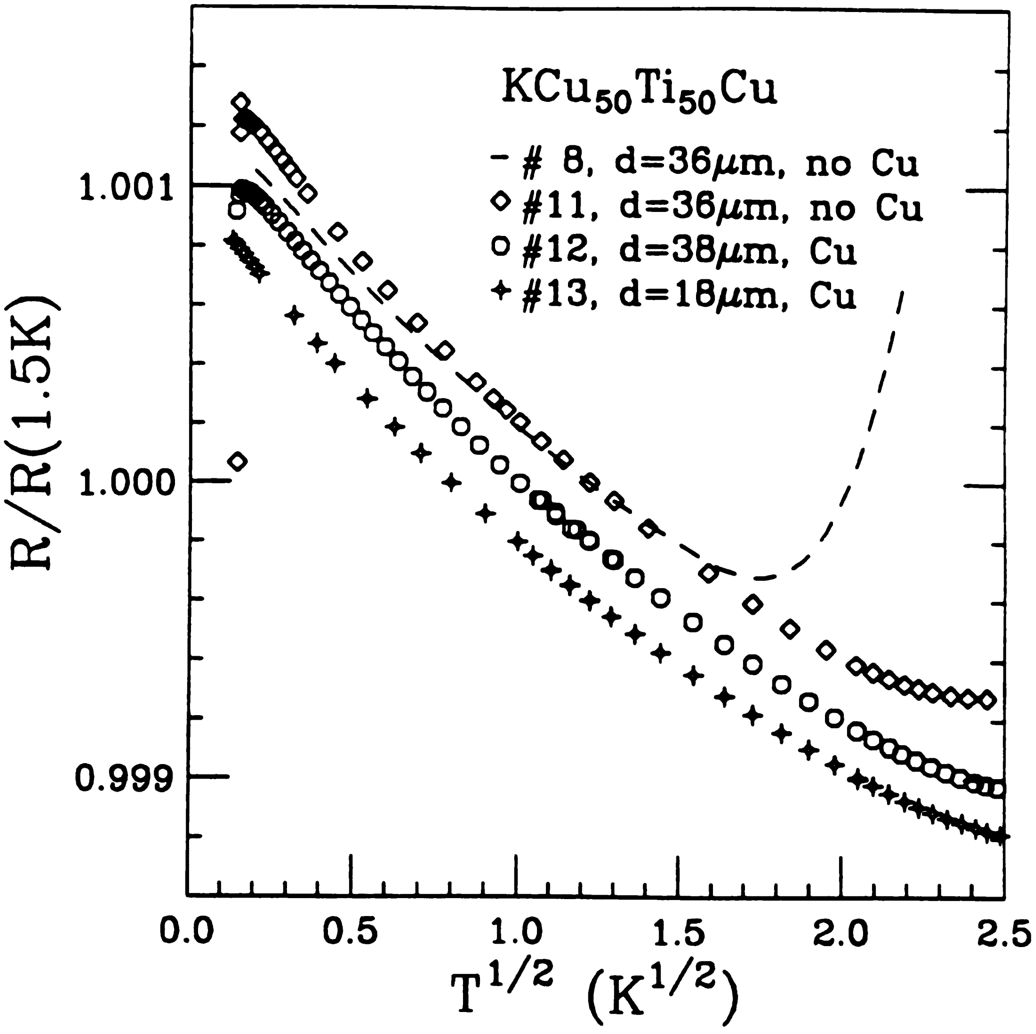

Figure 4.4: The relative resistances vs $\sqrt{T}$ for $KCu_{50}Ti_{50}Cu$ sandwiches with different CuTi ribbon thicknesses. For the clarity of presentation, the ordinates have been displaced.

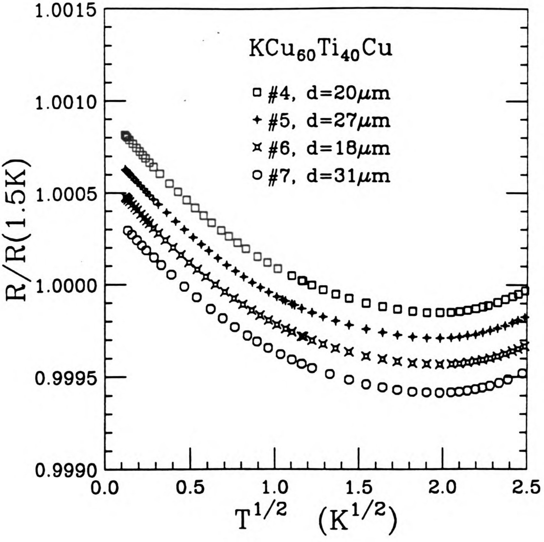

Figure 4.5: The relative resistances vs $\sqrt{T}$ for KCu$_{60}$Ti$_{40}$Cu sandwiches with different CuTi ribbon thickness. The ordinates have been displaced for clarity

However at the temperature near 20mK, the behavior of the data are a little different for sandwiches with different CuTi ribbon thicknesses. We believe this is related to the onset of superconductivity of the $Cu_{50}Ti_{50}$ ribbons. It is found that the sample with thinner CuTi ribbon shows a lower T_c than that of the thicker sample. The origin of this T_c dependence upon thickness is not understood.

Therefore we can conclude that the boundary resistances do not give any appreciable temperature dependent contributions at $T < 3$K for the samples with different preparation conditions, and that they are very small in comparison to that of CuTi ribbons.

For $T > 3$K, the temperature dependence of the resistances is mostly due to the electron phonon interaction in K. Its magnitude will depend on the thickness of K, as expected, but it also seems to depend on the quality of the contacts at K/Cu or K/CuTi interfaces. For samples $KCu_{50}Ti_{50}Cu$-11, 12, and 13, the data show very similar temperature dependences over the entire temperature region, for which we say that the K-contact is "good". However for sample $KCu_{50}Ti_{50} - 8$ (dashed curve in Figure 4.4), we say that the high temperature dependence of the resistance for $T > 2.9$K is related to having "poor" contacts between K and CuTi since this kind of problem rarely happens for the Cu-coated CuTi samples. As you will see later, whenever we have this poor contact problem at zero magnetic field, the magnetoresistivity also shows strong background contributions.

For the $KCu_{60}Ti_{40}Cu$ sandwiches, which are all Cu coated, the relative resistances are shown in Figure 4.5. We see that the temperature dependence of the resistance for the sandwiches with different CuTi ribbon thicknesses are almost the same over the entire temperature range. Since no onset superconductivity is seen at the lowest temperatures, we conclude that $Cu_{60}Ti_{40}$ alloy has a much lower T_c. Small positive temperature dependences at higher temperatures are due to the electron phonon interactions in K. Poor contacts rarely happen for these sandwiches.

4.2.2 Fitting Formula and Parameters

At zero magnetic field, the corrections to the resistivities of the amorphous CuTi alloys due to the weak localization and electron-electron interaction were given in Equation (2.30). Let us assume that our samples contain no spin impurities, then $1/\tau_s \sim 0$. If we also assume $\tau_i = \tau_{io} T^{-p}$, then the corrections to the resistivity for $\ln(T/T_c) \gg 1$ are

$$\begin{aligned}\frac{\Delta\rho}{\rho^2} &= -\frac{1.3e^2}{4\sqrt{2}\pi^2\hbar}\left[\frac{4}{3}+\frac{3}{2}(\lambda_{ep}-\tilde{F}_\sigma)+\frac{2}{\ln(T/T_c)}\right]\left(\frac{k_BT}{\hbar D}\right)^{1/2} \\ &+\frac{e^2}{2\pi^2\hbar\sqrt{D}}\left(\sqrt{\frac{T^p}{4\tau_{io}}}-3\sqrt{\frac{T^p}{4\tau_{io}}+\frac{1}{\tau_{so}}}\right) \ , \qquad (4.3)\end{aligned}$$

where the electron phonon coupling constant λ_{ep} is related to superconducting transition temperature and Debye temperature by MacMillan's expression [Mac 68, Sam 82]

$$\lambda_{ep} = \frac{1.04+\mu^*\ln(\Theta/1.45T_c)}{(1-0.62\mu^*)\ln(\Theta/1.45T_c)-1.04} \ , \qquad (4.4)$$

where μ^* is the effective Coulomb coupling constant, which is usually set to $\mu^* = 0.13$; and Θ is the Debye temperature, which is about 300K for both $Cu_{50}Ti_{50}$ and $Cu_{60}Ti_{40}$ alloys [Miz 83]. Since λ_{ep} is insensitive to T_c, we estimate that $\lambda_{ep} = 0.26 - 0.29$ for $Cu_{50}Ti_{50}$ with $T_c = 4 - 15$mK, and $\lambda_{ep} - 0.25$ for $Cu_{50}Ti_{50}$ with $T_c = 0.5 - 4$mK. The diffusion constant D can be calculated from the Einstein relation

$$D = \frac{1}{\rho e^2 N_\gamma(E_F)} \ , \qquad (4.5)$$

where ρ is the resistivity of the CuTi alloy and $N_\gamma(E_F)$ is the phonon-enhanced density of the states. From specific heat measurement [Moo 84, How 86], the values of the enhanced densities of states ($N_\gamma(E_F)$) are 1.8 and 1.6 states/(eV atom) for $Cu_{50}Ti_{50}$ and $Cu_{60}Ti_{40}$ alloys, respectively. The residual resistivities for the $Cu_{50}Ti_{50}$ and $Cu_{60}Ti_{40}$ alloys were measured at 4.2K by the typical four probe method with current parallel to the ribbon, and they are about $214\mu\Omega$ and $193\mu\Omega$, respectively.

So the diffusion constants D are found to be 0.24cm^2/s and 0.28cm^2/s, respectively. Therefore, in all of the following analysis, λ_{ep}, ρ, and D are fixed at the values shown in the Table 4.3. The fitting parameters are $\tilde{F}_\sigma, T_c, \tau_{io}, \tau_{so}$, and p.

Table 4.3: The Fixed Parameters

sample	ρ(4.2K) ($\mu\Omega$)	D (cm^2/s)	λ_{ep}	Θ_D (K)
$Cu_{50}Ti_{50}$	214	0.24	0.25 – 0.29	326
$Cu_{60}Ti_{40}$	193	0.28	0.25	326

At the temperature close to T_c, we have to consider the paraconductivity due to Aslamazov-Larkin and Maki-Thompson superconducting fluctuations as discussed in Section 2.3.5. Due to the previously-mentioned short wavelength cutoff and strong pair breaking effect, both the Aslamazov-Larkin and the Maki-Thompson contributions to the resistivity are less than about 1ppm in comparison to the residual resistivity for $T/T_c > 5$. To avoid these superconducting contributions, we have conservatively chosen to fit our data by Equation 4.3 for $T/T_c > 5$. Please also note that the Equation 4.3 is only strictly accurate for $\ln(T/T_c) \gg 1$.

4.2.3 $\rho(T)$ for $Cu_{50}Ti_{50}$ and $Cu_{60}Ti_{40}$ Alloys

In this study, the resistances for different CuTi sandwiches were measured at the temperature between 15mK and 6K. Figure 4.6 shows the resistance of the sandwich $KCu_{50}Ti_{50}Cu$-11. The lowest temperature for this sample is about 15mK. This is the first time that any measurements have been made on for $Cu_{50}Ti_{50}$ alloys to these low temperatures.

First, our data show that the resistance decreases with increasing temperature, which is generally true for the amorphous metals at low temperature due to weak localization and electron-electron interaction. The interaction term, which is propor-

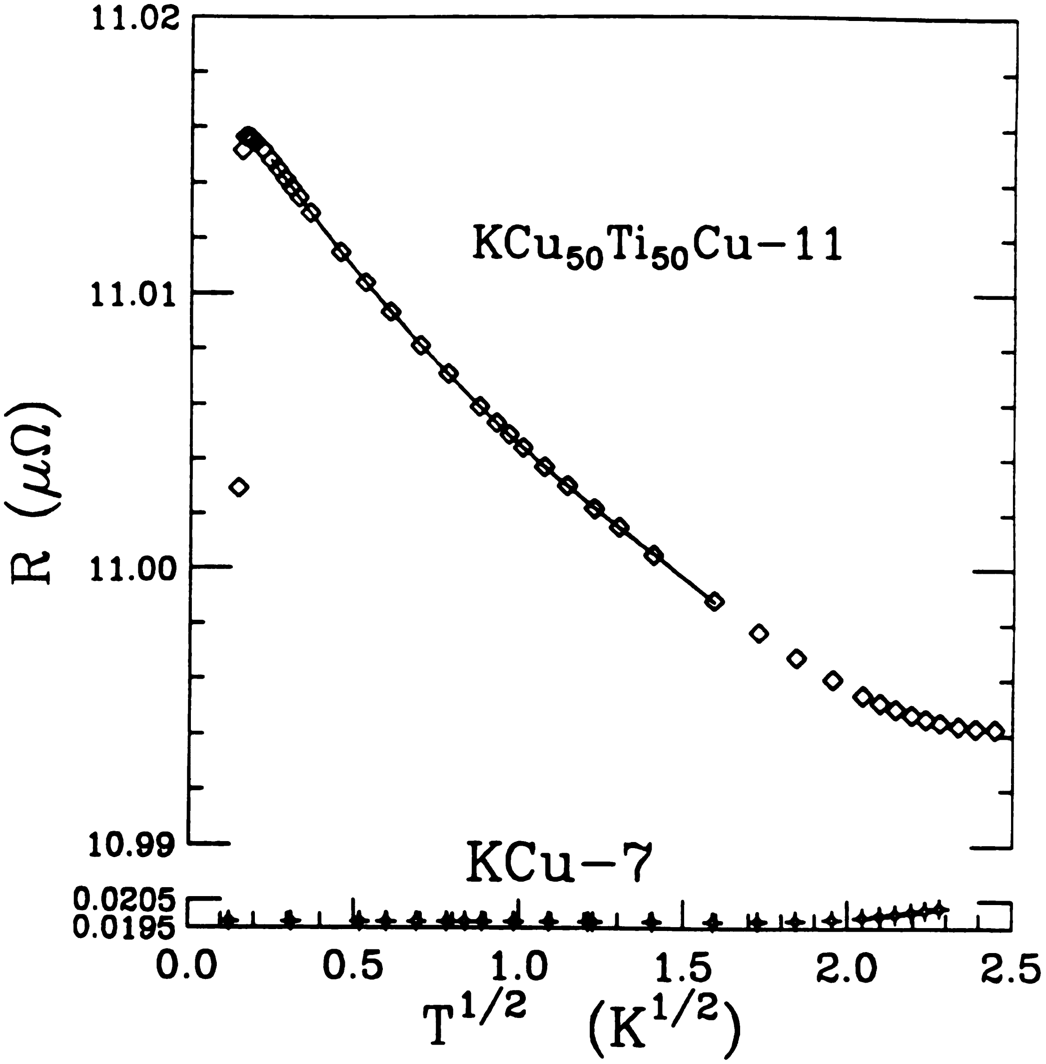

Figure 4.6: The resistances vs $\sqrt{T}$ for the $KCu_{50}Ti_{50}Cu$-11 and KCu-7 sandwiches.

tional to $-\sqrt{T}$, dominates the temperature dependence of the resistance at the lowest temperatures.

Secondly, for $T \sim 22$mK, the resistance of the sandwich starts falling, which indicates that the sample is becoming superconducting. The drop in the resistivity at 17mK is only about 2%, so the transition temperature must be lower than 17mK. The downturn, which starts at about 22mK, is due primarily to the superconducting fluctuations although the attractive electron-electron interaction in the Cooper channel also contributes a significant negative curvature as $T \rightarrow T_c$.

Thirdly, the data have a positive curvature for $T > 0.2$K. Since the electron-electron interaction contribution is proportional to $-\sqrt{T}$ and the weak localization term goes as $+T^n$ with $n > 0.8$ for $T < 10$K [Lin 88], the positive curvature of the data vs $\sqrt{T}$ indicates that weak localization makes a non trivial contribution. For $T > 3$K, the background contribution due to the electron phonon interaction in K also contribute to the positive curvature. For a comparison, the bottom data show the typical resistance of a Cu/K/Cu sandwich. Its magnitude is very small compared to that of the CuTi sample and its temperature dependence is negligible for $T < 3$K.

Table 4.4: The Fitting Parameters for $KCu_{50}Ti_{50}Cu$-11

p	τ_{io} (psK^p)	τ_{so} (ps)	T_c (mK)	$\tilde{F}_\sigma$	χ^2
1.4	4.3 ± 0.3	0.01 ± 0.0	7.9 ± 0.4	-0.64 ± 0.03	72
1.6	10.6 ± 6.3	0.06 ± 0.08	7.0 ± 0.9	-0.27 ± 0.19	66
1.8	21.1 ± 1.0	0.18 ± 0.03	5.9 ± 0.4	-0.08 ± 0.01	74
1.9	28.1 ± 1.4	0.27 ± 0.04	5.3 ± 0.4	-0.02 ± 0.01	85
2.0	36.5 ± 1.8	0.39 ± 0.06	4.6 ± 0.5	0.03 ± 0.01	100
2.1	46.5 ± 2.5	0.54 ± 0.09	3.9 ± 0.6	0.08 ± 0.01	122
2.2	58.2 ± 3.3	0.72 ± 0.13	3.2 ± 0.7	0.11 ± 0.01	150
2.3	71.7 ± 4.2	0.92 ± 0.17	2.3 ± 0.9	0.14 ± 0.0	185
2.5	100 ± 3.9	1.40 ± 0.20	0.5 ± 2.5	0.16 ± 0.06	284

The solid curve in the figure is the best fit of the Equation 4.3 to the data. The fit was done only between 52mK and 2.7K in order to avoid the electron-phonon contributions at the high temperatures and superconducting fluctuations at the low temperatures. In the fit, λ_{ep}, D, ρ are fixed as in Table 4.3, and p is set at some discrete values such as 1.4, 1.6, 1.8 $\cdots$ etc. The fits are done for each p, and the best fitting parameters are obtained as shown in Table 4.4. However the fits for $p < 1.9$ are not good because $\tilde{F}_\sigma < 0$ (the physical meaningful values: $0 < \tilde{F}_\sigma < 0.93$). If we chose the fits with $\chi^2/\chi^2_{min} < 2$ as acceptable fits, the best parameters are: $1.9 < p < 2.3$, 28psK^p < τ_{io} <72psK^p, 0.3ps< τ_{so} <0.9ps, 2.3mK< T_c <5.3mK, and $0 < \tilde{F}_\sigma < 0.14$. These parameters systematically change as p varies from 1.9 to 2.3. The best-fit curve is shown in Figure 4.6, and it fits the data very well and is unaffected for $1.9 < p < 2.3$. Note that the χ^2 of these fits is based on our estimates of the random uncertainties for our resistance measurements.

To check in part the reproducibility of our samples, we studied a number of $Cu_{50}Ti_{50}$ and $Cu_{60}Ti_{40}$ ribbons, which were made under conditions and with thicknesses as listed in Table 4.1. The temperature dependences of relative resistances for the $KCu_{50}Ti_{50}Cu$ sandwiches are shown in Figure 4.7. The ordinates of each data set have been displaced by a constant for clarity. For the earlier samples $KCu_{50}Ti_{50}Cu$-7, 8 and 9, the data were taken between 40mK and 5K. For samples $KCu_{50}Ti_{50}Cu$-11 to 16, the measurements were carried out from 15mK to 6K.

At temperatures between .1K and 3K, the data for all the sandwiches agree with each other pretty well. At temperatures below about 30mK, the differences in resistivities among the sandwiches are probably due to variations of T_c. It is found that the T_c is lower for the sandwich $KCu_{50}Ti_{50}Cu$-13, whose CuTi ribbon thickness is just about half of the other samples. Note that the resistance of $KCu_{50}Ti_{50}Cu$-16 increases somewhat faster than the other samples with decreasing temperature and has a lower T_c. We believe the data for this sample were not taken at zero magnetic

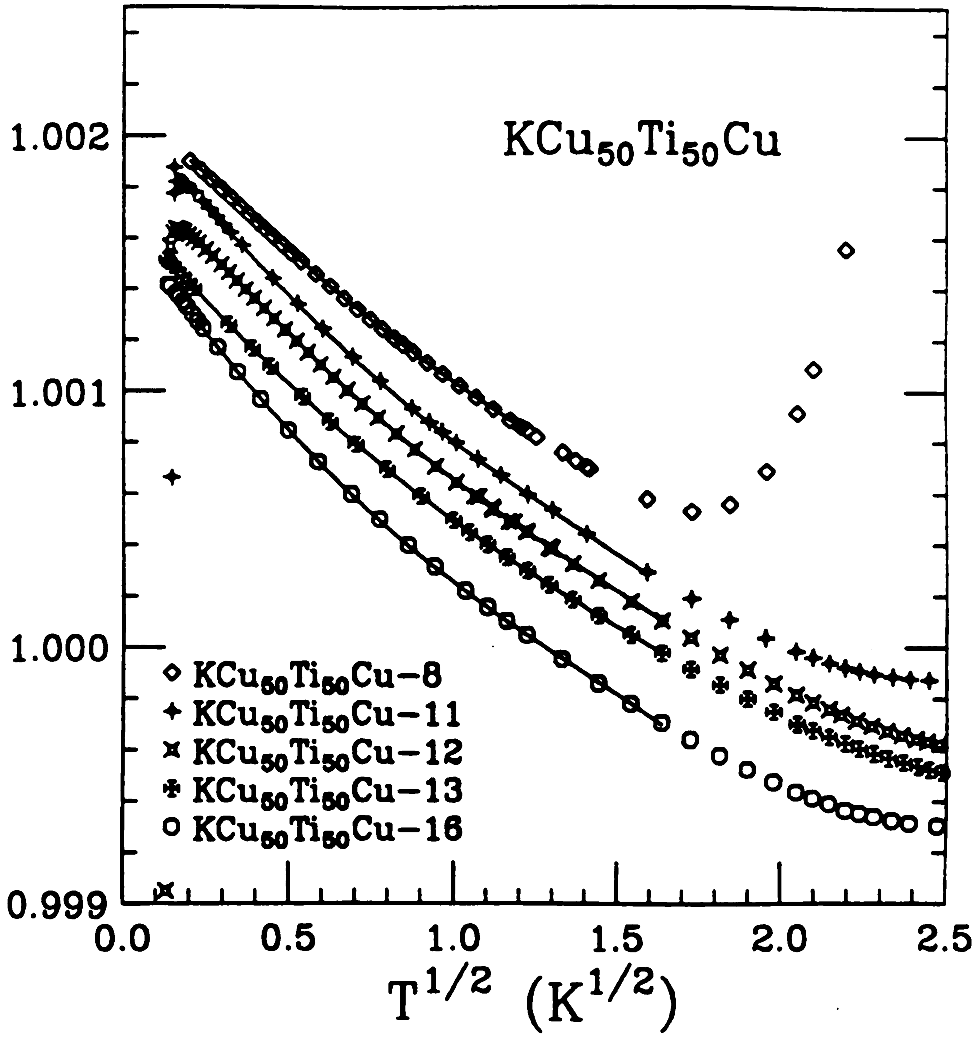

Figure 4.7: The relative resistances vs $\sqrt{T}$ for the $KCu_{50}Ti_{50}Cu$ sandwiches. The ordinates have been displaced for clarity.

field. Further details will be presented at the end of this section. The differences in behaviors of the resistances for the $T > 3$K are due to the electron-phonon interaction in K. For the poor-contact sample KCu$_{50}$Ti$_{50}$Cu-8, the resistance increases rapidly with increasing temperature.

The solid curves are the best fits using the same method as in KCu$_{50}$Ti$_{50}$Cu-11 for 52mK< T < 2.7K. The best-fit parameters are listed in Table 4.5.

Table 4.5: The Fitting Parameters for the KCu$_{50}$Ti$_{50}$Cu and KCu$_{60}$Ti$_{40}$Cu Sandwiches

Sample	p	τ_{io} (psK^p)	τ_{so} (ps)	T_c (mK)	$\tilde{F}_\sigma$
KCu$_{50}$Ti$_{50}$Cu-8 [a]	1.6 – 2.5	40 – 172	0 – 3.1	6.8 – 5.7	0.14 – 0.35
KCu$_{50}$Ti$_{50}$Cu-11	1.9 – 2.3	28 – 72	0.3 – 0.9	5.3 – 2.3	0.0 – 0.14
KCu$_{50}$Ti$_{50}$Cu-12 [b]	2.0 – 3.2	60 – 441	0.28 – 3.8	8.7 – 4.1	0.12 – 0.32
KCu$_{50}$Ti$_{50}$Cu-13	1.6 – 2.5	24 – 187	0.03 – 1.4	4.2 – 0.3	0.0 – 0.28
KCu$_{50}$Ti$_{50}$Cu-16	2.3	50	0.57	0.3	0.0
KCu$_{60}$Ti$_{40}$Cu-2 [b]	2.2 – 3.1	61 – 160	0.08 – 1.2	3.3 – 2.3	0.27 – 0.39
KCu$_{60}$Ti$_{40}$Cu-4	1.8 – 2.4	29 – 77	0.0 – 0.34	2.0 – 0.3	0.15 – 0.31
KCu$_{60}$Ti$_{40}$Cu-5	2.0 – 2.5	41 – 89	0.06 – 0.47	2.1 – 0.9	0.26 – 0.37
KCu$_{60}$Ti$_{40}$Cu-6	1.7 – 2.2	21 – 51	0 – 0.20	1.8 – 0.5	0.110.28
KCu$_{60}$Ti$_{40}$Cu-7	1.7 – 2.6	22 – 105	0 – 0.63	2.8 – 0.2	0.14 – 0.39
Cu$_{65}$Ti$_{35}$ from Lindqvist	2.0 – 2.5		0.08 – 0.25	0.0	0.0 – 0.32

[a]) Temperature fitting range: 50mK< T <1.5K.
[b]) χ^2 is large and insensitive to p.

From the Table 4.5, we see that the parameters for all the KCu$_{50}$Ti$_{50}$Cu sandwiches are in the similar ranges even if the samples were made under different conditions. The best fits are obtained for p between 1.7 and 2.5. τ_{io} changes from about 30 to 200psK^p, depending on the choice of p. Similarly, the spin orbit scattering time τ_{so} has values between 0 and 3ps, which is rather small. The screening parameter $\tilde{F}_\sigma$ is in the range of 0 to 0.3, which is consistent with Lindqvist [Lin 88]. T_c decreases substantially with increasing p. As Equation 4.3 shows, the resistance is weakly dependent upon T_c via the $\ln(T/T_c)$ term. Also note that Equation 4.3 is only accurate for $\ln(T/T_c) \gg 1$. Thus it is difficult to obtain an accurate value of T_c from the data with $T/T_c > 5$. The sample $KCu_{50}Ti_{50}Cu$-16 behaves a little differently from the other samples and was more difficult to fit. For $p < 2.2$, we could get a very good fit, but only with $\tilde{F}_\sigma < 0$, which is unphysical. For $p \geq 2.3$, the χ^2 of fit is larger than other samples and diverges rapidly as p increases. It is possibly that Equation 4.3 is invalid at nonzero magnetic field. It is remarkable that τ_{io} and τ_{so} are so similar for all the samples at the same value of p.

For $T <$ 50mK, we must consider the paraconductivity due to the Aslamazov-Larkin and Maki-Thompson superconducting fluctuation discussed in Section 2.3.5. Since the theoretical formula for the Maki-Thompson contribution to the conductivity is not exactly known in this temperature range, we will omit this analysis for these temperatures.

Figure 4.8 shows the relative resistances vs temperature for the $KCu_{60}Ti_{40}Cu$ sandwiches in zero field. The data were taken between about 16mK and 6K. Although all the samples are Cu coated, the poor contact occurred occasionally, as shown by the $KCu_{60}Ti_{40}Cu$-8 sandwich, whose residual resistance is five times bigger than other samples. In comparison to Figure 4.7, these data behave similarly to the $KCu_{50}Ti_{50}Cu$ sandwiches, with the following exceptions:

(1) There is no downturn in the resistivities even at the lowest temperature, but very slight negative curvatures in the resistances are observed at temperatures below about 25mK. This feature indicates that the $Cu_{60}Ti_{40}$ alloy is a superconductor with a much lower T_c than for the $Cu_{50}Ti_{50}$ alloy.

(2) The resistivities for the different $KCu_{60}Ti_{40}Cu$ samples are much more similar over the entire temperature range in comparison to those of $KCu_{50}Ti_{50}Cu$ sandwiches, particularly at very low temperature. Note, however, that sample $KCu_{60}Ti_{40}Cu$-8

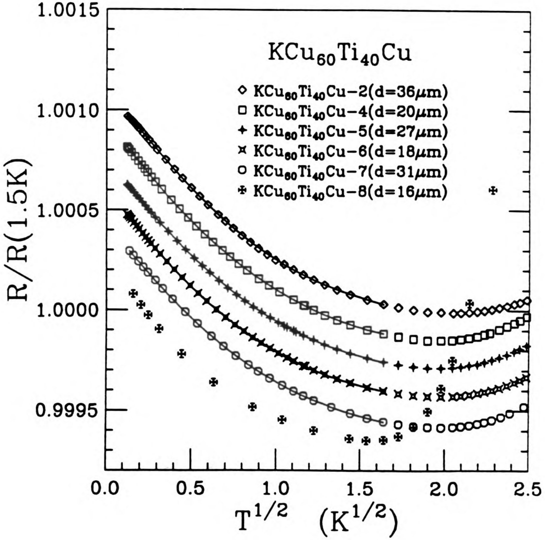

Figure 4.8: The relative resistances vs $\sqrt{T}$ for the $KCu_{60}Ti_{40}Cu$ sandwiches. The ordinates have been displaced for for clarity.

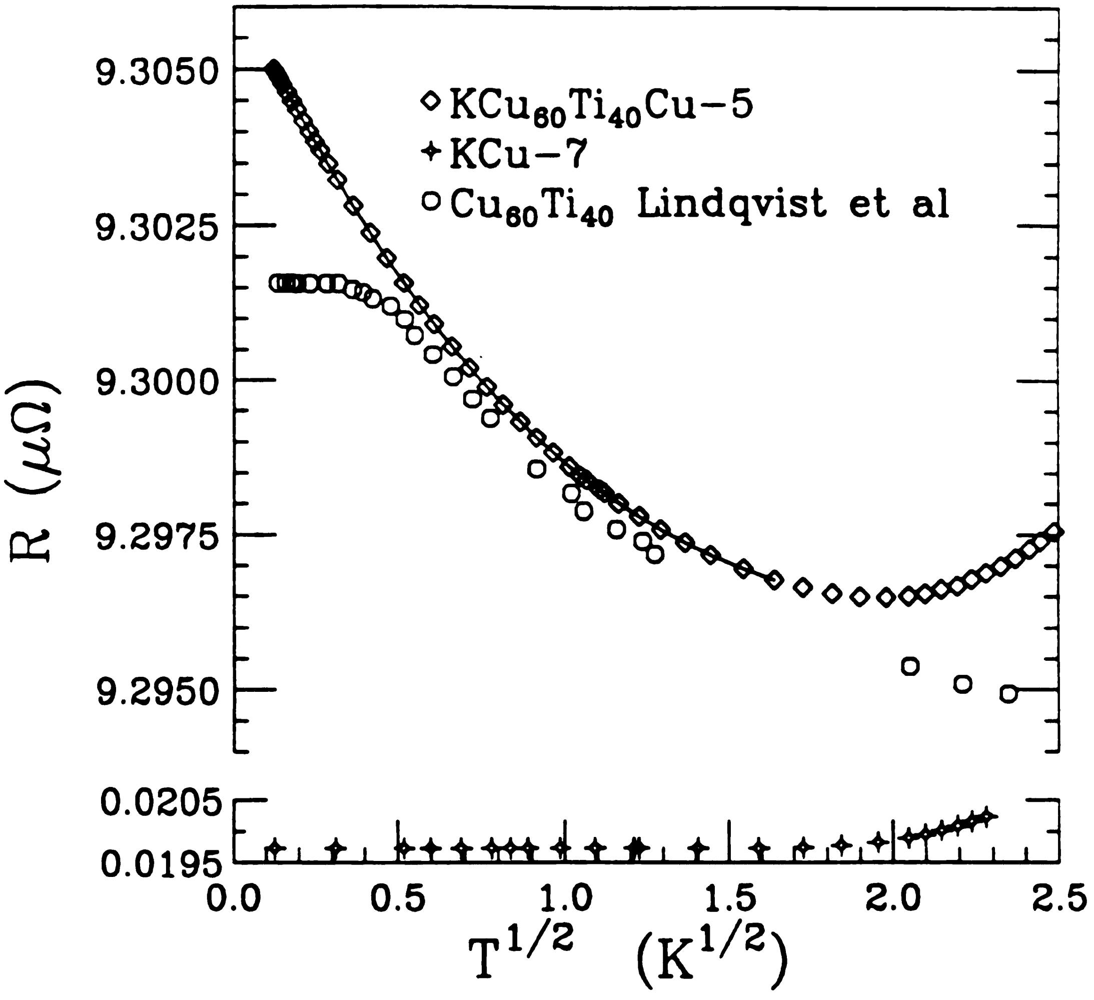

Figure 4.9: The resistances vs $\sqrt{T}$ for the $KCu_{60}Ti_{40}Cu$-5 and KCu-7 sandwiches. The ordinates have been displaced for clarity and easy comparison.

does behave somewhat differently due to its "poor" electrical contacts with K.

(3) For 20mK< T < 4K, the total change of the resistance for $KCu_{60}Ti_{40}Cu$ samples is only about half of that for $KCu_{50}Ti_{50}Cu$ samples. This is due to the differences in D, ρ, τ_i, and T_c.

In Figure 4.9, the data at the top and the bottom of the figure are for the $KCu_{60}Ti_{40}Cu$-5 sample and for the KCu-7 sandwich, respectively. The open circles represent the data of a $Cu_{60}Ti_{40}$ sample from Lindqvist *et al* [Lin 88], which were the only data for $Cu_{60}Ti_{40}$ alloys measured to these low temperatures. These data have been suitably renormalized for a comparison. Between 0.25K and 1.7K, their data agree beautifully with ours. At T > 4K, our resistances are bigger than theirs, which is mostly due to the previously-mentioned electron-phonon Umklapp contribution in the K of our samples, as shown in the bottom of the figure. At T < 0.25K, the resistance of their sample becomes a constant while the resistance of our sandwich continues to increase. We have concluded that their sample probably did not cool much below 0.25K, due to the poor thermal conducting properties of the varnish that they used as a thermal conduct agent between their sample and their cold finger with its attached thermometers. Thus Figure 4.9 clearly shows the superiority of our new method.

The solid curves in Figure 4.8 are the best fits by Equation 4.3 over a temperature range 15mK< T <2.7K, using the same method as for the $KCu_{50}Ti_{50}Cu$ samples. The best-fitting parameters are also listed in Table 4.5. From the table, we see that the parameters for the different $Cu_{60}Ti_{40}$ sandwiches have similar values. The values of $\tau_{io}, \tau_{so}, T_c$, and $\tilde{F}_\sigma$ systematically change with p. The most favorable p is about 1.8 – 2.5, which is about the same as for the $KCu_{50}Ti_{50}Cu$ sandwiches. The fitting values for $\tau_{io}, \tau_{so}, T_c$, and $\tilde{F}_\sigma$ are 30 – 100ps, 0.0 – 0.5ps, 3 – 0.2mK, and 0 – 0.37 respectively. It is clear that $T_{min}/T_c \geq 5$ is satisfied in our fits (15mK< T < 2.7K). For the same p, the values of the τ_{io}, τ_{so}, and $\tilde{F}_\sigma$ for different $Cu_{60}Ti_{40}$ sandwiches are very close. As observed for the $KCu_{50}Ti_{50}Cu$ sandwiches, T_c is lower for the sandwich with the thinner CuTi ribbon. Since Lindqvist *et al.* did not list the parameters for their $Cu_{60}Ti_{40}$ sample, we list in Table 4.5 the parameters of their $Cu_{65}Ti_{35}$ sample for a rough comparison. We see that their parameters are consistent with ours, as discussed later in Section 4.4

We know that weak localization can make a significant contribution to the resistance even at very low temperatures, but how large is this contribution? Figure 4.10 compares the data with the computed total resistivity and the Electron-Electron Interaction (EEI) contributions. The dashed and dotted lines represent the EEI contributions for the $Cu_{50}Ti_{50}$ and $Cu_{60}Ti_{40}$ samples, respectively, which are calculated from Equation 4.3 using the best fit parameters in Table 4.5. The upper and lower dashed and dotted lines correspond to the extreme values of p: 2.5 and 1.8, respectively. The differences between the data and the lines are the weak localization contributions to the resistivities. From this figure, we see that the weak localization makes a non trivial contribution ($\Delta\rho_{WL}/\Delta\rho_{ee} > 10\%$) to the resistivity even at the temperatures down to 0.15K. The total resistivity computations (solid curves) are unaffected by this range of p on the scale of this graph.

As we mentioned earlier, Figure 4.7 shows that resistivity of the $KCu_{50}Ti_{50}$-16 sandwich increases faster than any other sample with decreasing temperature below about 0.3K, which indicates that the T_c for this sample is smaller than for the other samples. The fits in the Table 4.5 also showed a much lower T_c for this sample. This difference is at least partially due to the non-zero field trapped inside the superconducting magnet. For this sample, we first measured the magnetoresistances at 4.2K, reduced the magnet current to zero, and then cooled the sample down to the lowest temperatures. Next we measured temperature dependence of the resistance, as shown in Figure 4.7. Once the superconducting solenoid is energized, there can be a nonzero magnetic field trapped inside the magnet even the current though the magnet is zero.

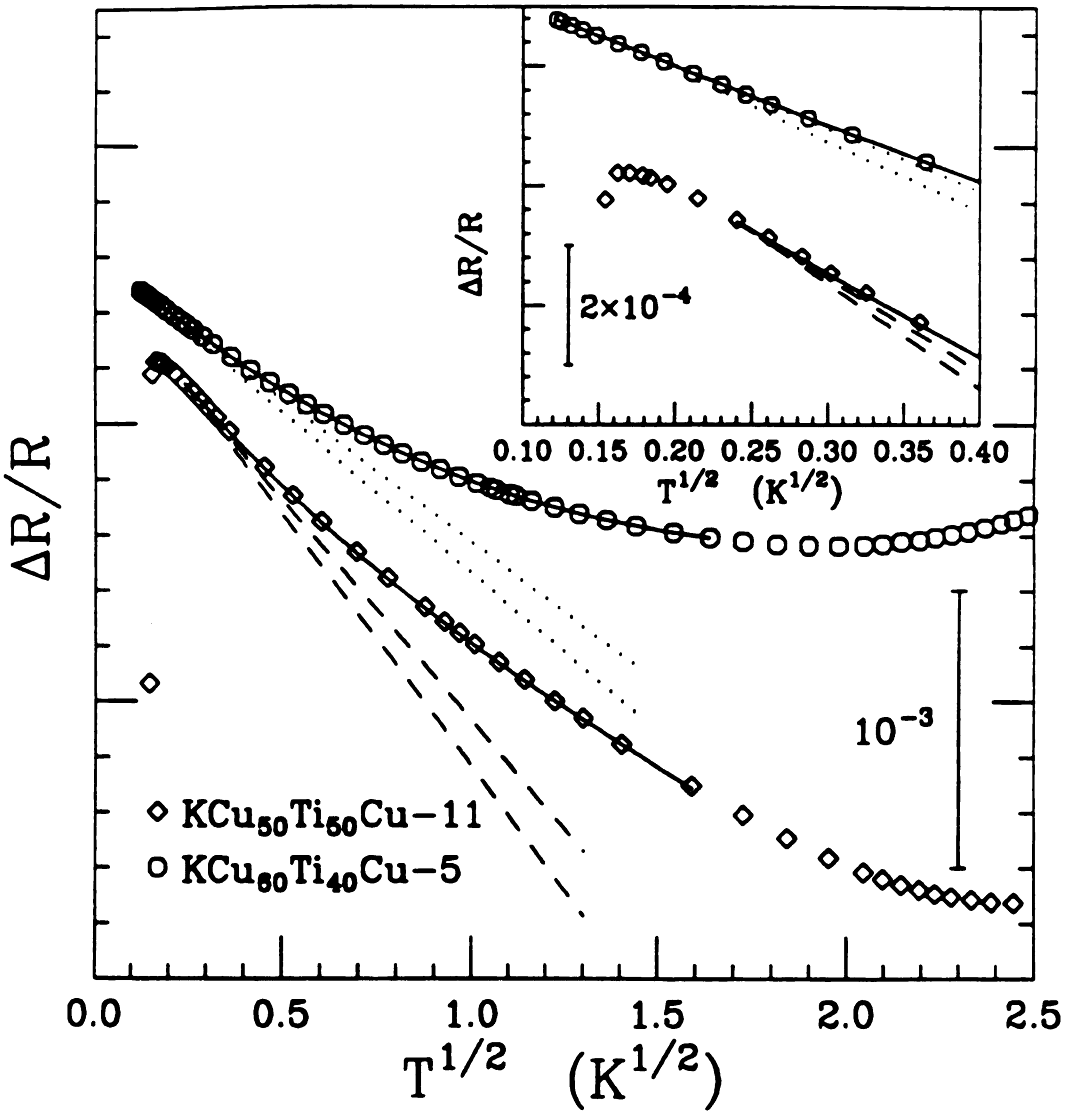

Figure 4.10: The contributions to the relative resistances due to weak localization and electron-electron interaction. The ordinates have been displaced for clarity.

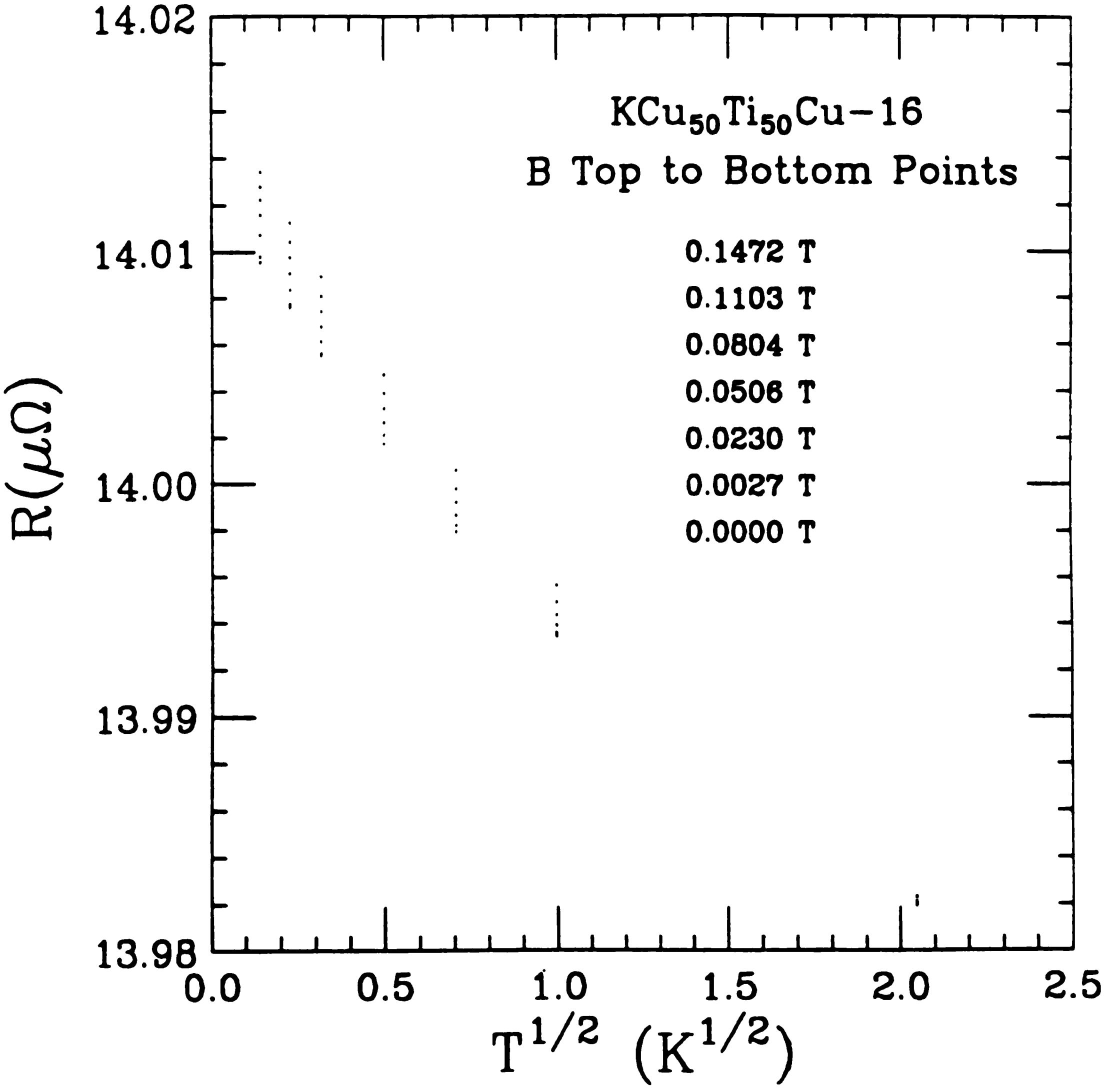

Figure 4.11: The temperature dependences of the resistances at different magnetic fields for sample $KCu_{50}Ti_{50}Cu$-16.

Based on the typical behaviors of the superconducting solenoids, we estimate that the residual field is less than about 10 Gauss. This residual field seems to suppress T_c appreciably, which will enhance the resistivity especially at temperatures close to T_c. In a future experiment, it would be useful to cool the sample first in zero field and then energize the magnet.

To observe the overall magnetoresistance, the temperature dependences of the resistances at different magnetic fields are plotted in Figure 4.11. At low temperatures, the field dependences of the resistance are significant, and these field dependences decrease with increasing temperature.

4.3 Magnetoresistivities

Magnetoresistance measurement is another important tool for studying the amorphous alloys. In this section, we will present and discuss our magnetoresistance data.

4.3.1 Background Magnetoresistivities and Fitting Formulas

Like the zero field resistances, the magnetoresistances for our sandwiches also have two parts: resistances of the CuTi ribbons and the so-called background resistances, which are due to the Cu electrodes, K layers. and the boundaries among the K layers, Cu electrodes, and CuTi ribbons.

Experiments and theories have shown that at small magnetic fields, the magnetoresistivities of pure Cu and K are proportional to B^2 [Zim 60, Pip 89]. In order to find the magnitude and field dependences of the magnetoresistances due to Cu, K and their boundaries, we measured the magnetoresistances of the Cu/K/Cu sandwiches listed in Table 4.2. Figure 4.12 shows the magnetoresistances $\Delta R(B,T) = R(B,T) - R(T)$ for the Cu/K/Cu sandwiches at $T = 0.5$K, where $R(T)$ is for $B = 0$.

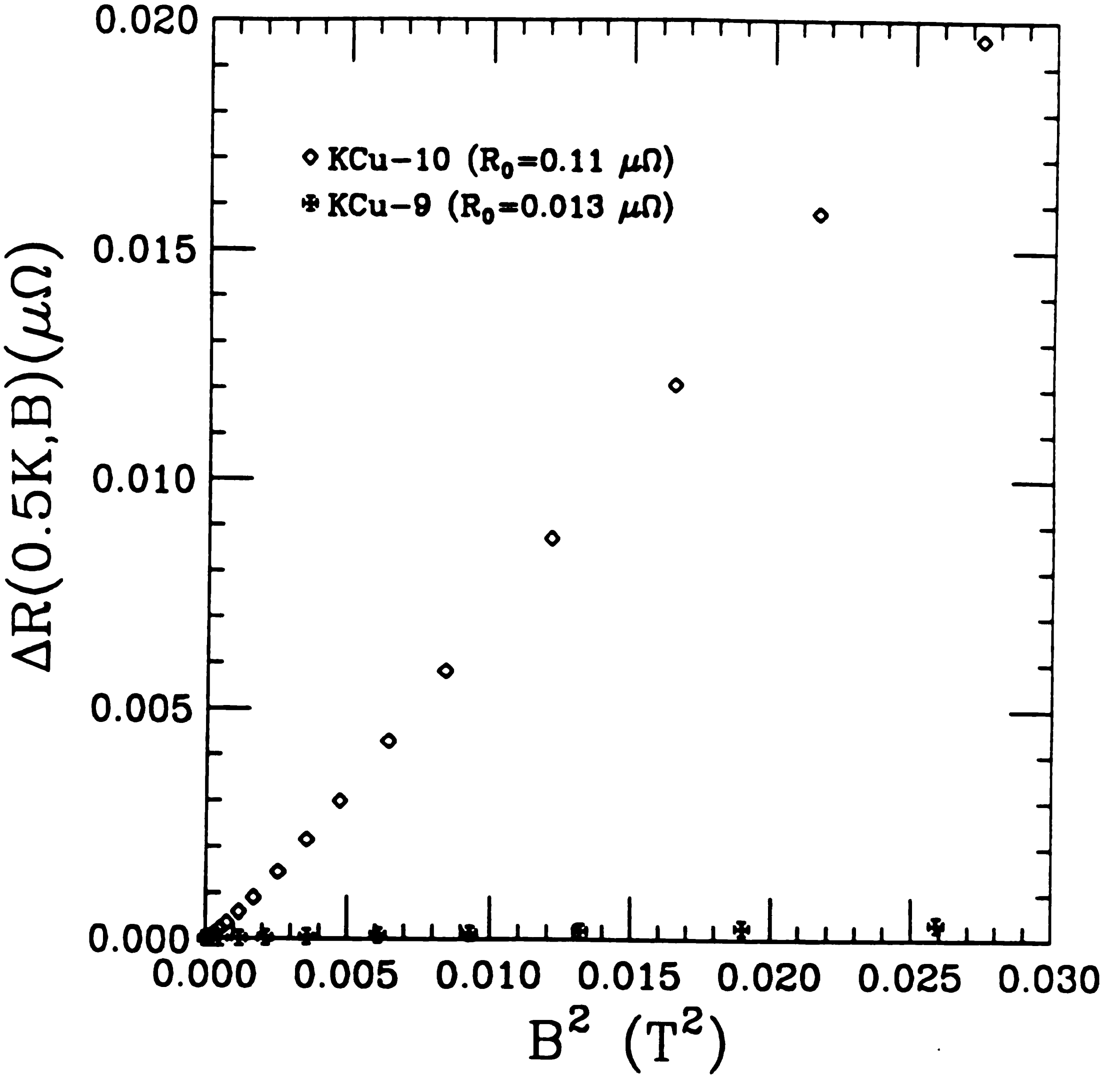

Figure 4.12: The magnetoresistances vs B^2 for the Cu/K/Cu sandwiches.

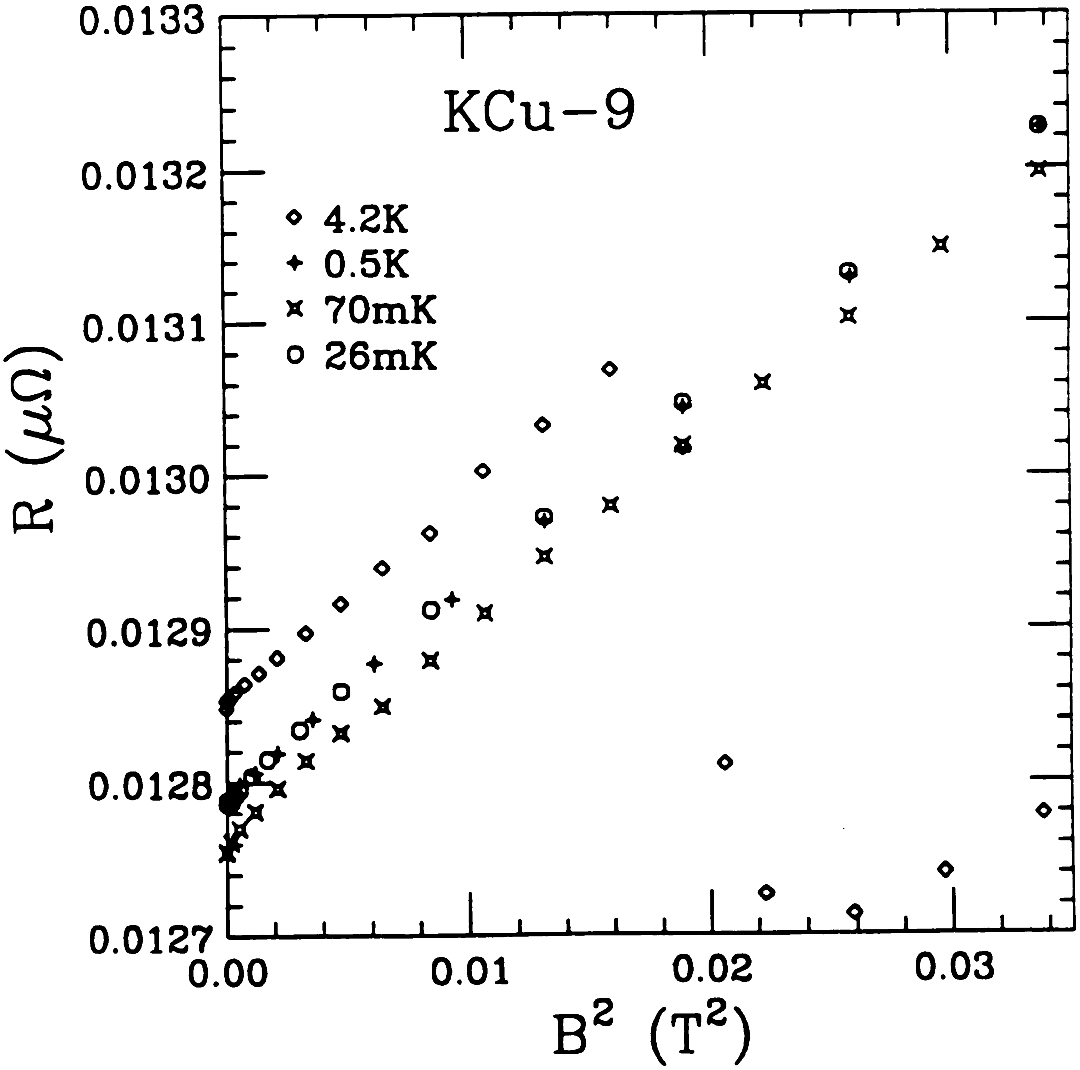

Figure 4.13: The magnetoresistances vs B^2 at different temperatures for the KCu-9 sandwich.

From the figure, we see that the magnetoresistances of the two sandwiches increase with magnetic field and obey approximately a square law, but the magnitudes are very different for the two samples. KCu-9 has a very thin layer of K, whose zero field resistance is about $0.02\mu\Omega$. Its resistance increases very slowly with magnetic field. At 0.15 Tesla, the resistance has risen only by about 3%. For sandwich KCu-10, which has a much thicker layer of K and a resistance of about $0.1\mu\Omega$, its resistance increases much more rapidly with B than that of KCu-9. Thus in order to reduce this part of the background magnetoresistances, the thickness of the K layer in the sandwich must be minimized.

To examine the temperature dependences of the background magnetoresistances, we show in Figure 4.13 the magnetoresistances of the KCu-9 sandwich vs B^2 at different temperatures. We see that all the data have almost the same slopes. That is, at most fields, the magnetoresistances at different temperatures only differ by constants. This means that the field dependent parts of the resistances of the Cu/K/Cu sandwiches are temperature independent. However for the data at 4.2K, the resistance drops suddenly for $B > 0.13$T. We believe that this is related to the presence of superconducting PbSn solder on the voltage leads of the Cu electrodes. At 4.2K, the critical field of the superconducting solder will be lower because T is closer to its T_c of about 7K. Thus it is not surprising that this resistance drop occurs at lower temperatures with $B > 0.17$T since the critical field will be higher at these lower temperatures. Similar drops in resistance are seen for the CuTi sandwiches. So in our analyses and fits, we keep $B <0.15$ Tesla.

The other background contribution to the magnetoresistance is due to the boundaries between the sputtered-Cu coatings and the CuTi ribbon, which we have not directly measured. Since we know, from Figure 4.13 and the above arguments, that the magnetoresistance ($\Delta R(T,B) = R(T,B) - R(T,B=0)$) of a Cu/K/Cu sandwich is temperature independent, we are going to assume in our analysis that the

Cu/CuTi boundary magnetoresistance has the same property. We will then see if this assumption is supported by the magnetoresistance data for CuTi sandwiches.

4.3.2 Analyses of the Magnetoresistances due to Various Scattering Mechanisms

From Chapter 2, we know that the corrections to the magnetoresistivities of an amorphous metal due to weak localization, electron-electron interaction, and superconducting fluctuations are given in Equations (2.34), (2.36), (2.38), (2.40), and (2.41). These formulas are fairly complicated, and it is very difficult to analyze the data by directly applying these formulas. In order to simplify the fitting, we will present an approximate analysis concerning the magnitude of the magnetoresistance and its temperature and field dependences for each scattering mechanism.

Figure 4.14 shows the magnetoresistivities due to weak localization (first term in Equation 2.34), Zeeman spin splitting (second term in Equation 2.34), electron electron interaction (EEI), and superconducting fluctuations at T = 52mK and 0.5K for a set of typical parameters: T_c = 5mK, D = 0.24cm^2/s, and α = 0.25, $\tilde{F}_\sigma$ = 0.3, τ_{io} = 700psK^p, τ_{so} = 15ps, p=1.7, g = 2, and β is from Table 2.1.

At both temperatures, we see that the weak localization and Zeeman spin splitting make the major contribution to the resistivity at low and high fields, respectively. The Maki-Thompson contribution is important only for $T/T_c < 20$ ($\beta > 0.1$).

The contribution from the diffusion channel (DC) in the electron-electron interaction depends on $\tilde{F}_\sigma$ and becomes important only for $T < 0.1$K and $B > 0.05$T. The Cooper channel (CC) gives a very small negative contribution at all temperatures, which can be neglected.

Another quantity which indicates the strength of the scattering at some particular temperature is the scattering field, which is defined by $B_{scat} = \hbar/(4eD\tau_{scat})$. The scat-

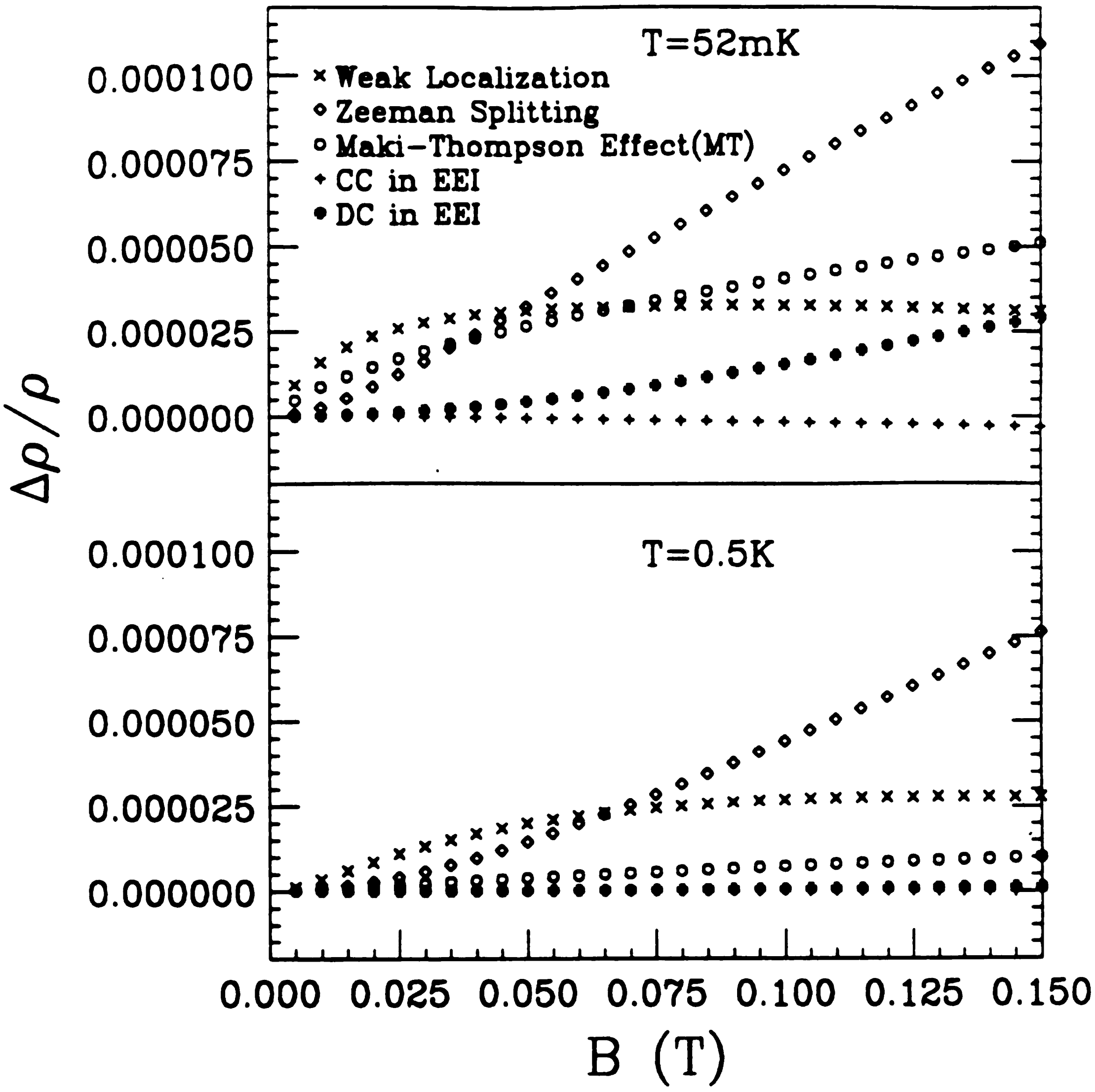

Figure 4.14: The theoretical relative magnetoresistivities due to different scattering mechanisms.

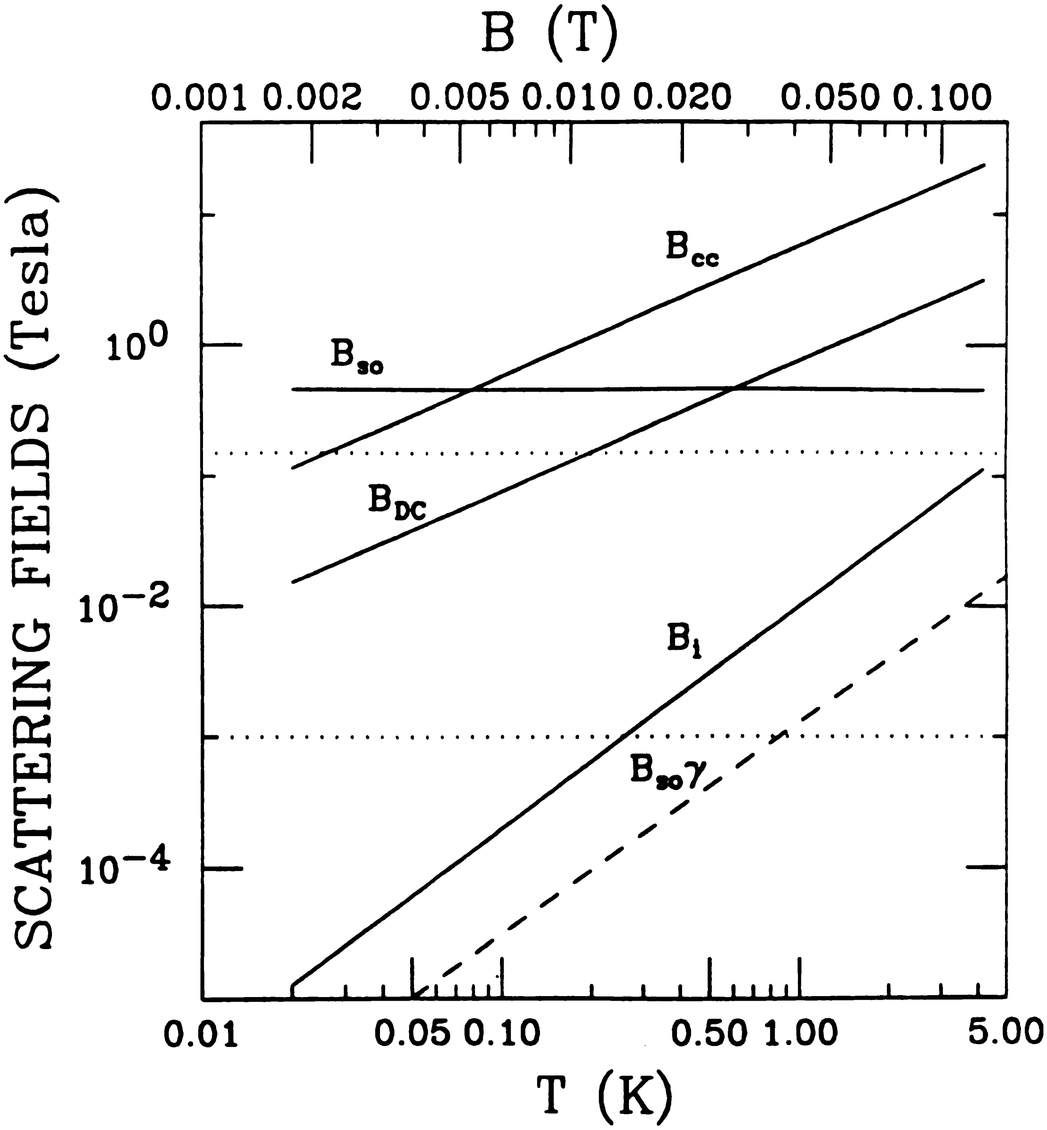

Figure 4.15: The scattering fields vs T and B for various scattering mechanisms.

tering fields for weak localization with the Zeeman splitting and the Maki-Thompson effect are B_i, B_{so}, and B_-, where we have

$$B_- \simeq B_i + \gamma B_{so} \quad , \tag{4.6}$$

and $\gamma = 7.32 \times 10^{-3} \tau_{so}^2 B^2$. For the Cooper and diffusion channels of the electron-electron interaction, the scattering fields are

$$\begin{aligned} B_{CC} &= 1.355 \frac{T}{D} \quad , && (4.7) \\ B_{DC} &= 0.745 T \quad . && (4.8) \end{aligned}$$

The ratios of these characteristic fields to the actual applied magnetic field B determine the magnitudes of functions f_3, ϕ_3, and g_3 in the weak localization, the Maki-Thompson fluctuation, and the electron-electron interaction contributions. For $B \ll B_{scat}$, the magnetoresistivity due to each scattering process is proportional to B^2 and for $B \gg B_{scat}$, it is proportional to $\sqrt{B}$. However the scattering fields for each scattering mechanism are different, and they can be temperature and field dependent as shown in Figure 4.15.

In this plot, the parameters are same as for Figure 4.14. The ordinate is the scattering field; the bottom abscissa is the temperature; and the top abscissa is the magnetic field, which applies only to γB_{so}. The region between the two horizontal dotted lines represents the range of the actual magnetic fields that we used. We see that the scattering fields B_{so} and B_{CC} are generally much larger than B, so their contributions can be evaluated in the small field limit or be neglected. For $T > 0.1$K, diffusion-channel interaction contribution can be also approximated as a small field limit. Weak localization contribution is related to B_i and $B_- = B_i + \gamma B_{so}$. The dashed line shows the field dependence of γB_{so}, and it is always much smaller than the applied magnetic field. So at $T < 0.1$K, where $B \gg B_i, B_-$, the weak localization contribution may be approximated as a large field limit, but for $T > 0.1K$ it is difficult to make any approximations.

At magnetic fields and temperatures where we can not make any approximations, we will calculate the magnetoresistivities using the approximate analytical expressions for f_3, ϕ_3, and g_3 given by Ousset and Baxter [Ous 85, Bax 89]

4.3.3 ρ(B) for $Cu_{50}Ti_{50}$ and $Cu_{60}Ti_{40}$ Alloys

Figure 4.16 shows the relative magnetoresistances of the $KCu_{50}Ti_{50}Cu$-16 at seven different temperatures. Data symbols are our results, and the solid curves are the best fits, which will be discussed later. The data sets from the top to bottom correspond to the temperatures shown in the figure. Except for 4.2K, the ratio of adjacent temperatures is about a factor of two.

First, from the figure, we see that the magnetoresistivities increase with increasing magnetic field at all the temperatures, with the exception of the 4.2K data for $B >$ 0.08T which was described in Section 4.3.1. The 20mK data increase faster at low field than at any other temperature, which is mainly due to the Maki-Thompson superconducting fluctuations.

Secondly, for $B <$ 0.03T, the curvature of the magnetoresistivities changes from negative to positive at 0.25K. We believe that this sign change is mostly likely due to the inelastic scattering. Since $B_i \sim T^p$, for $T \leq$ 0.1K we have $B/B_i \gg 1$, for which the resistivity is proportional to $\sqrt{B}$. For $T >$ 0.5K, we have $B/B_i <$ 0.6, and the resistivity is proportional to $B^{3/2}$ (see also Figure 4.15).

Thirdly, for $B >$0.05T, the resistances increase with magnetic field more or less linearly, which indicates that the contributions from weak localization, Zeeman splitting, electron-electron interaction, and the background are all competing with each other.

Since we do not know the magnitude and field dependence of the background resistivity, we can not fit our data directly to the equations given in Section 2.4. However,

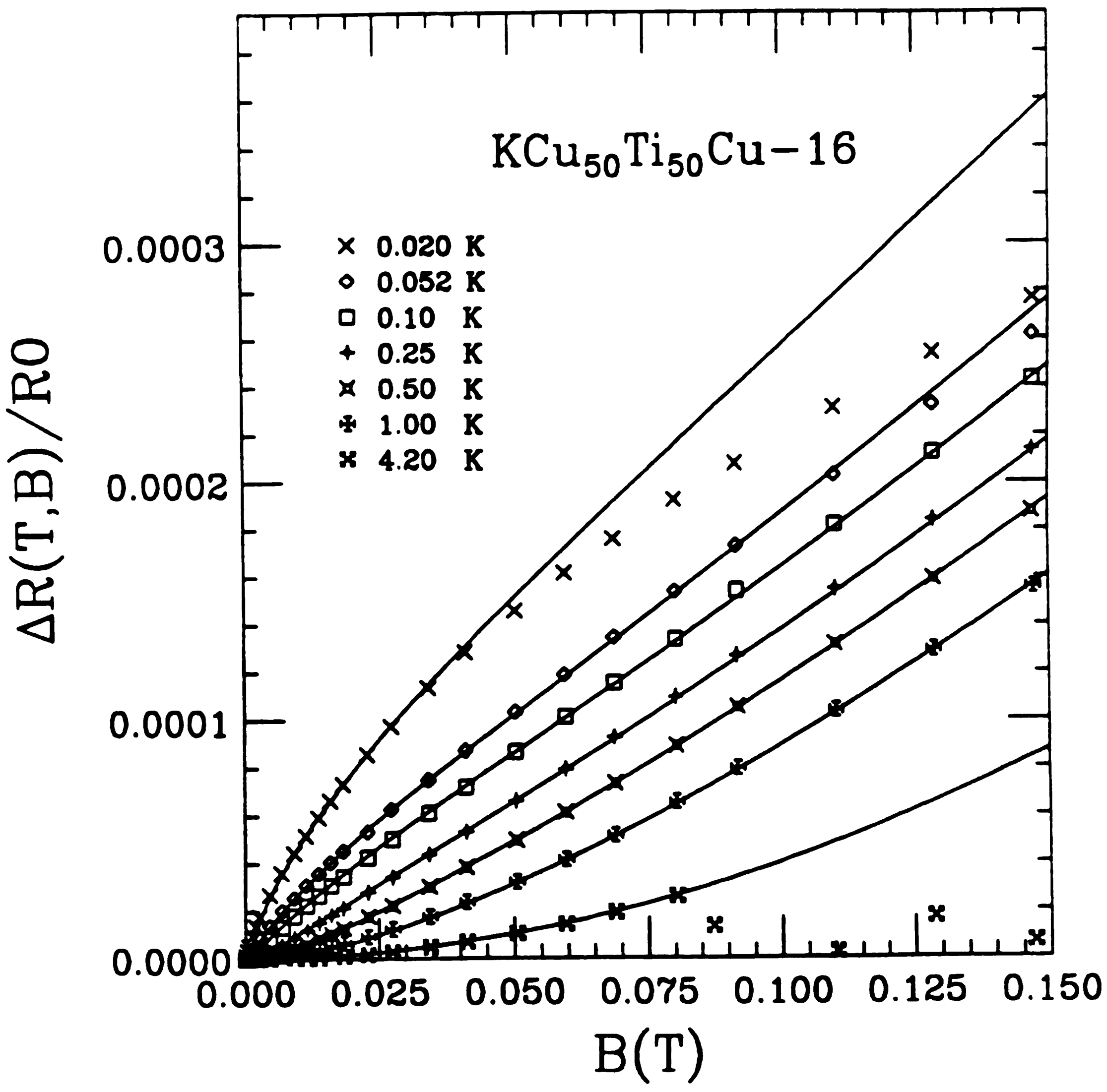

Figure 4.16: The relative magnetoresistance data and fits for the $KCu_{50}Ti_{50}Cu$-16 sandwich.

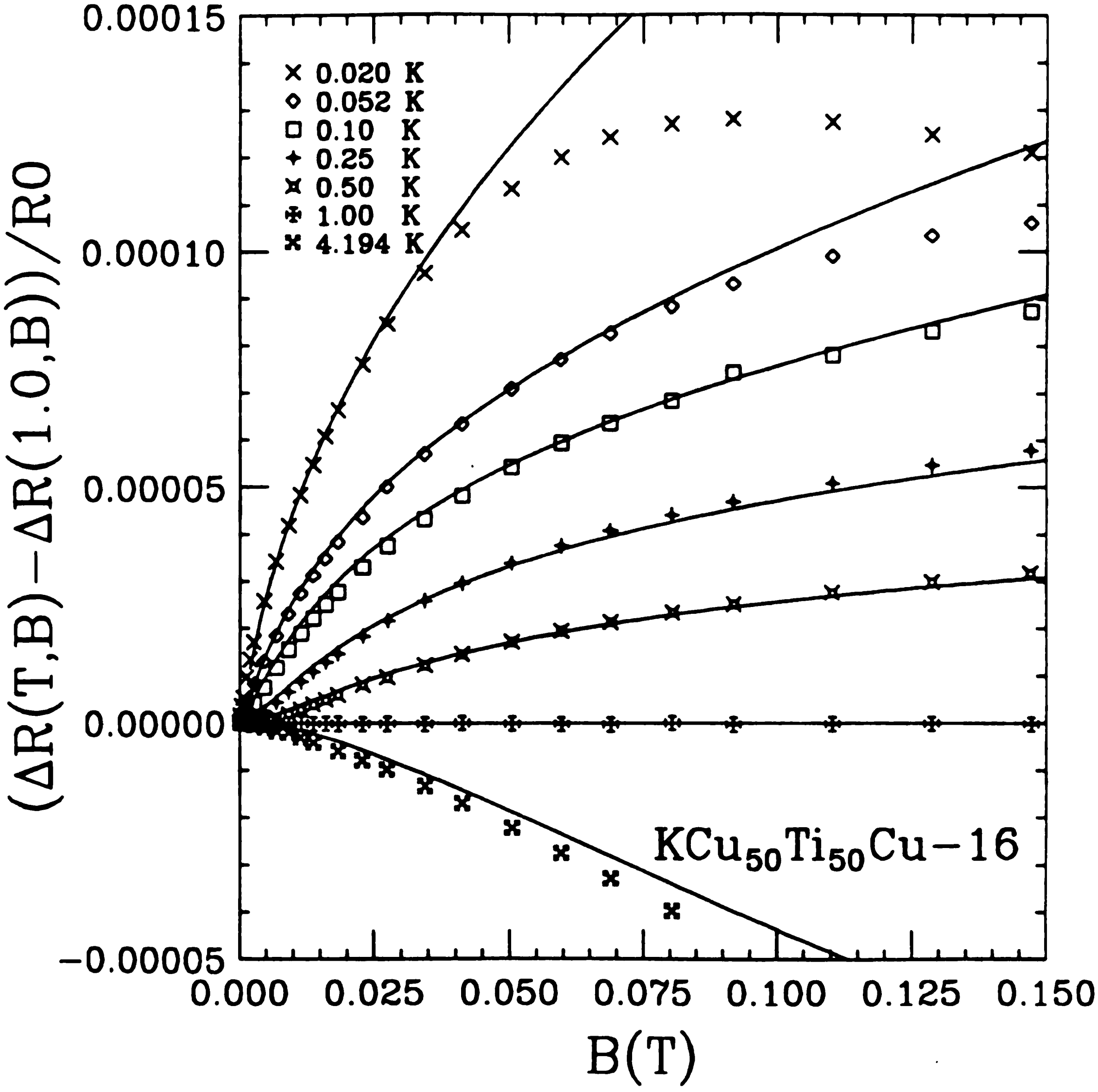

Figure 4.17: The modified magnetoresistance data and their fits for the $KCu_{50}Ti_{50}Cu$-16 sandwich.

in Section 4.2.1 and 4.3.1 we assumed that the background magnetoresistances are temperature independent. Therefore, if we take the differences of our data points between T and 1K at the same magnetic field ($\Delta R(T,B) - \Delta R(1\mathrm{K},B)$), the resulting data (called modified data) should be free of the background contributions. Thus the modified data can be fitted by the differences of the equations given in Section 2.4 between T and 1K. Figure 4.17 shows the modified data vs B, where R_o is the residual resistance.

According to Figure 4.14 and 4.15, the Cooper channel contribution is very small. In the fits we set $\alpha = 0.25$, and $g(B,T) = -1/\ln(T^*/T_c)$, T^*=max$(T, 4DeB/k_B)$ [Bax 89]. Thus there is no free parameter for the Copper channel, whose contribution to the resistance can be calculated for each temperature and field. For the diffusion channel, $\phi_3(B/B_{DC})$ can be calculated using the approximate analytical expression [Ous 85]. The only variable parameter is $\tilde{F}_\sigma$.

The other contributions to the magnetoresistivity are due to weak localization with Zeeman splitting and Maki-Thompson fluctuations. In the Maki-Thompson contribution, $\beta(B,T)$ is the function in Equation 2.42, and it depends on temperature as well as magnetic field. However in the low field limit, when $B, B_i \ll (k_BT/4De)\ln(T/T_c)$, we have $\beta(B,T) = \beta(T)$ [Ric 88], which is tabulated in Table 2.1. To simplify the computation of $\beta(B,T)$, we have used the approximation that $\beta(B,T) = \beta(T)$. In our measurements, this low field limit is satisfied except for the lowest temperature and the highest field. For the weak localization, since B_i is not exactly known and f_3 converges very slow even for $B \gg B_i$, it is inaccurate to make any simplifications. Thus B_i (or τ_i) is chosen as a fitting parameter. The approximate expression for f_3 is used for the calculation. So in our analysis, the fitting parameters are τ_i, τ_{so}, T_c, and $\tilde{F}_\sigma$, and the fixed parameters are D, λ_{ep}, and ρ (as listed in Table 4.3), the Lande g-factor $g = 2$ for electrons, and $\alpha = 0.25$ for the strong spin-orbit scattering.

Since we fit the modified data by the differences of the equations between T and

1K, we are required to know the fitting parameters at 1K. Since T_c ,τ_{so}, and $\tilde{F}_\sigma$ are temperature independent, the only parameter we are required to know is τ_i, which is equal to τ_{io} at 1K. So we preset the τ_{io} to different values until the best fit is obtained for all the data at different temperatures. Then parameters τ_i, τ_{so}, T_c , and $\tilde{F}_\sigma$ are obtained, and the best fits are shown in Figure 4.17. The fits (solid curves) are very good except for the modified data at 20mK and $B > 0.04$T (B/T >2T/K), which are almost constant for $B > 0.05$T. We tried and failed to get a good fit to this set of the modified data over the whole field range. The theoretical formulas in the Section 2.4 give values that are too large for us to obtain a good fit to the data. We now suggest some reasons for this disagreement, although at this time we can not make a definitive choice among them.

(1) Dilute spin impurities. Baxter *et al* [Bax 89] have indicated that magnetic impurities will introduce a magnetoresistance which is proportional to $-B^2$ at low fields and saturates at high fields. Since $\Delta\rho/\rho$ for CuTi alloy is typically of order of $\sim 10^{-4}$ between 0 and 0.15 Tesla, a tiny amount of magnetic impurities may reduce the magnetoresistance significantly.

(2) Since B is not much less than $(k_BT/4De)\ln(T/T_c)$for $B > 0.05$T and $T <$ 40mK, $\beta(B,T)$ will decrease with increasing magnetic field [San 85], and it is smaller than $\beta(T)$, which we used in our fits at all fields and temperatures. Therefore the actual magnetoresistances at higher fields will be lower than our fits indicate.

(3) Magnetic fields lower the T_c. With such small T_c, a small magnetic field will suppress T_c substantially [Sch 90]. This effect will make the Maki-Thompson contribution to the magnetoresistance decrease with increasing magnetic field.

However, for weak spin-orbit coupling systems (e.g. CaAl), theoretical models agree with experimental data even for $B/T = 23$T/K. [Lin 90, Sam 89]. It is unclear why there are discrepancies between theoretical predictions and experimental data for strong spin-orbit coupling systems.

The the best fitting parameters for this sample are $\tau_{io} = 680 - 750\text{psK}^p$ and $\tau_{so} = 13 - 25\text{ps}$, which are much bigger than the the values from the zero field resistances. At low temperature, τ_i shows tendency to saturate, which will be discussed later. The bigger τ_{so} is mainly due the the data at 4.2K. For $T > 1\text{K}$, the contributions from the weak localization, electron-electron interaction, and Maki-Thompson fluctuations are very small. The big difference in the magnetoresistivity between 1K and 4.2K is mainly due to Zeeman splitting, which makes the magnetoresistance increase with increasing τ_{so} for 0.1ps< τ_{so} <50ps [Lin 88]. p and $\tilde{F}_\sigma$ are similar to values obtained at zero magnetic field but with a smaller range. T_c drops by half, which may be suppressed due to the magnetic field.

For the $\text{KCu}_{60}\text{Ti}_{40}\text{Cu}$-7 sandwich, the raw data are shown in Figure 4.18. As with $\text{KCu}_{50}\text{Ti}_{50}\text{Cu}$-16 sandwich, the magnetoresistance increases with the magnetic field over the entire field range. There are some differences between the two samples:

(1) For $T \leq 0.1\text{K}$ and $B < 0.03\text{T}$, the magnetoresistivity increases much slower with B than that of the $\text{KCu}_{50}\text{Ti}_{50}\text{Cu}$-16 sandwich. Since the $\text{Cu}_{60}\text{Ti}_{40}$ alloy has a much lower T_c than $\text{Cu}_{50}\text{Ti}_{50}$, the Maki-Thompson contribution to the magnetoresistance, which is proportional to $\beta(T) \sim \ln^{-2}(T/T_c)$, is much smaller than for the $\text{Cu}_{50}\text{Ti}_{50}$ sample with $T \leq 0.1\text{K}$.

(2) The magnetoresistances for this sandwich become temperature independent for $T \leq 0.1\text{K}$ while no obvious low temperature saturation is observed for sample $\text{KCu}_{50}\text{Ti}_{50}\text{Cu}$-16. From (1), we know that the Maki-Thompson contribution is very small for sample $\text{KCu}_{60}\text{Ti}_{40}\text{Cu}$-7. Thus from Figure 4.14 we know that weak localization with Zeeman splitting will contribute a major part to the magnetoresistivity. From Figure 4.15 with $T \leq 0.1\text{K}$, we see that $B \gg B_i, B_-$, and the weak localization contribution becomes insensitive to temperature change. This insensitivity to the

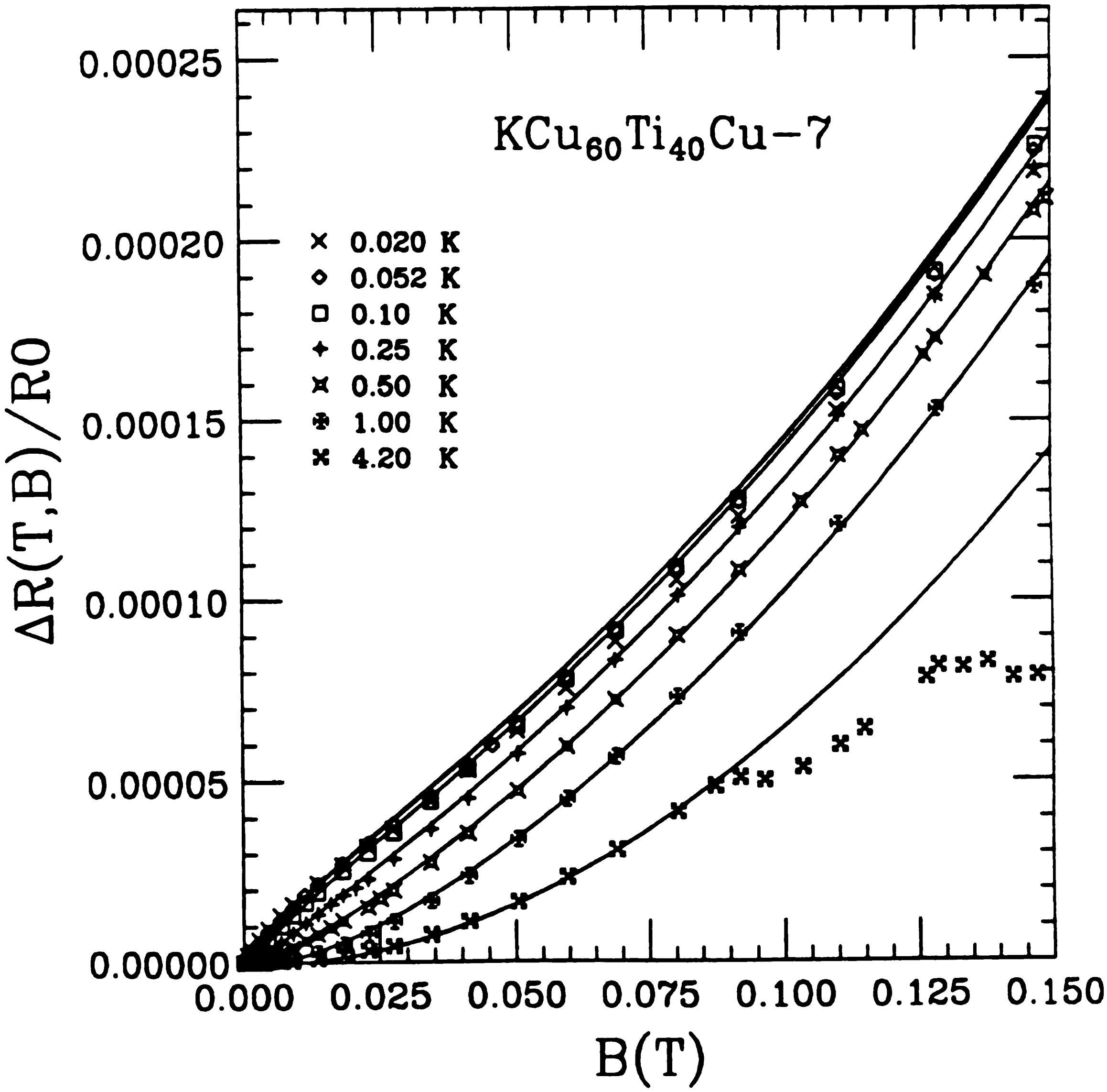

Figure 4.18: The relative magnetoresistance data and fits of the $KCu_{60}Ti_{40}Cu$-7 sandwich.

temperature accounts partially for the weak temperature dependence of the magnetoresistivity. Another possible mechanism is due to the dephasing by electron spin scattering by impurities as described by Baxter *et al* [Bax 89]. This scattering will make B_i saturate below some temperature T_s, which depends on the concentration of the spin impurities. Thus the saturation of B_i causes the function $f_3(B/B_i)$ in the weak localization and Maki-Thompson contribution terms (i.e. magnetoresistance) to become temperature independent for $T < T_s$. A rough calculation shows that amorphous alloys with a 10^{-7} relative concentration of magnetic impurities could have a spin scattering lifetime τ_s comparable to τ_i at 0.1K. Thus the effective inelastic scattering time, $1/\tau_i^* = T^p/\tau_{io} + 1/\tau_s$, may be saturated at $T < 0.1$K, as shown later in Figure 4.21.

As with the $KCu_{50}Ti_{50}Cu$-16 sandwich, background magnetoresistances also exist for the $KCu_{60}Ti_{40}Cu$-7 sandwich. Using the same procedure as with sample $KCu_{50}Ti_{50}Cu$-16, the differences of the magnetoresistances between T and 1K were taken and are shown in Figure 4.19. Based on the same arguments for sandwich $KCu_{50}Ti_{40}Cu$-16, the fixed parameters are $\alpha = 0.25$, $D = 0.28\text{cm}^2/\text{s}$, and $\rho = 193\mu\Omega$. The set of fitting parameters is same as before. The best fits are obtained as shown in Figure 4.19.

We see that the fits are pretty good for $T > 0.1$K, but once again we are unable to get good fits for $T < 0.1$K and $B > 0.25$T. Since T_c is very small, the effect of $\beta(B,T)$ on the magnetoresistances is much smaller. Thus the most probable reason for these poor fits is due to impurity-spin scattering, as discussed earlier.

From the best fits, the fitting parameters we obtained are $\tau_{io} = 870 - 950\text{psK}^p$, $\tau_{so} = 7 - 15$ps, $p = 1.6 - 1.8$, and $\tilde{F}_\sigma = 0 - 0.3$, and $T_c < 0.1$mK. As with the $Cu_{50}Ti_{50}$ alloy, τ_{io} and τ_{so} are much greater than their zero field values, and T_c is extremely small. For $T < 0.1$K, τ_i saturates, and this will be discussed in more detail in Section 4.4. We notice that, except for T_c, these parameters are very close to the

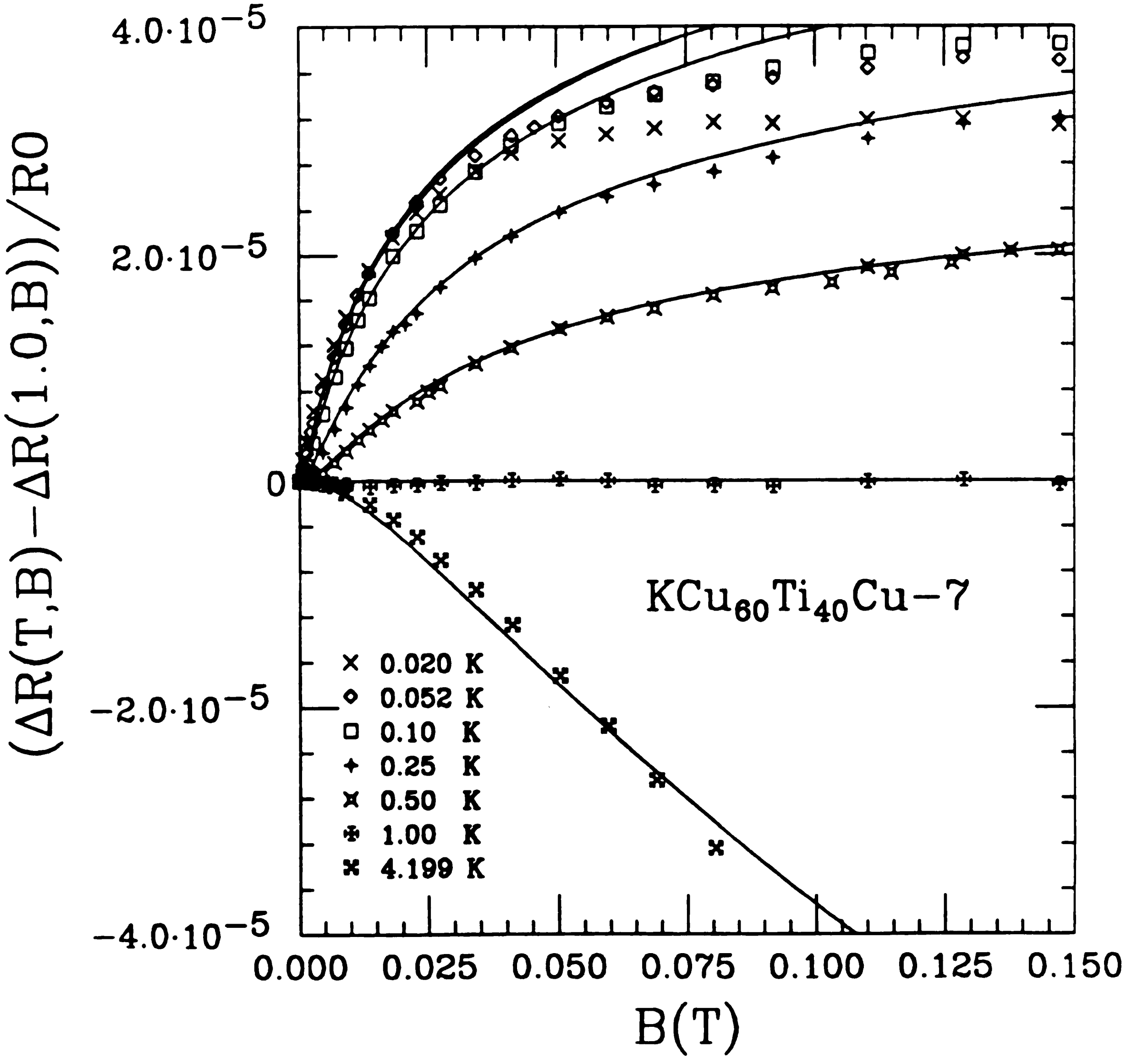

Figure 4.19: The modified magnetoresistance data and their fits for the $KCu_{60}Ti_{40}Cu$-7 sandwich.

parameters for the $KCu_{50}Ti_{50}Cu$-16 sample.

Using the best fitting parameters, the background magnetoresistances, which were removed in the modified data, can be estimated by taking the differences between the data in Figure 4.16 or 4.18 and values from the theoretical expressions at the same temperatures. The background contributions for $T = 0.5$K, which include the various boundary resistances, are shown in Figure 4.20 as a function of B. For the other temperatures, the background magnetoresistances are found to be almost the same as for $T = 0.5$K, which means that the background magnetoresistances are temperature independent, as we assumed.

For a comparison, the magnetoresistances of the KCu-9 and KCu-10 sandwiches are also plotted in the same figure. Indeed the background contributions follow rather well a B^2 dependences. The magnitude of the background resistances for $KCu_{50}Ti_{50}Cu$-16 is different from that for $KCu_{60}Ti_{40}Cu$-7, which is understandable because the K layers in these two sandwiches may have different thicknesses, and the boundary resistances maybe also be different. But they are both rather small compared to KCu-10 sample, which is the worst of the Cu/K/Cu sandwiches.

By simply adding these 0.5K background magnetoresistances to the best-fitting theoretical expressions for all temperatures, we obtained the predicted fits for the raw data, which are the solid curves in Figure 4.16 and 4.18. We see that the fits are remarkably good except at lower temperatures and higher fields, where the fits to the modified data were also not so good. Note that these good fits for $T \neq 0.5$K in Figure 4.16 and 4.18 again confirm our assumption that the background magnetoresistances are temperature independent.

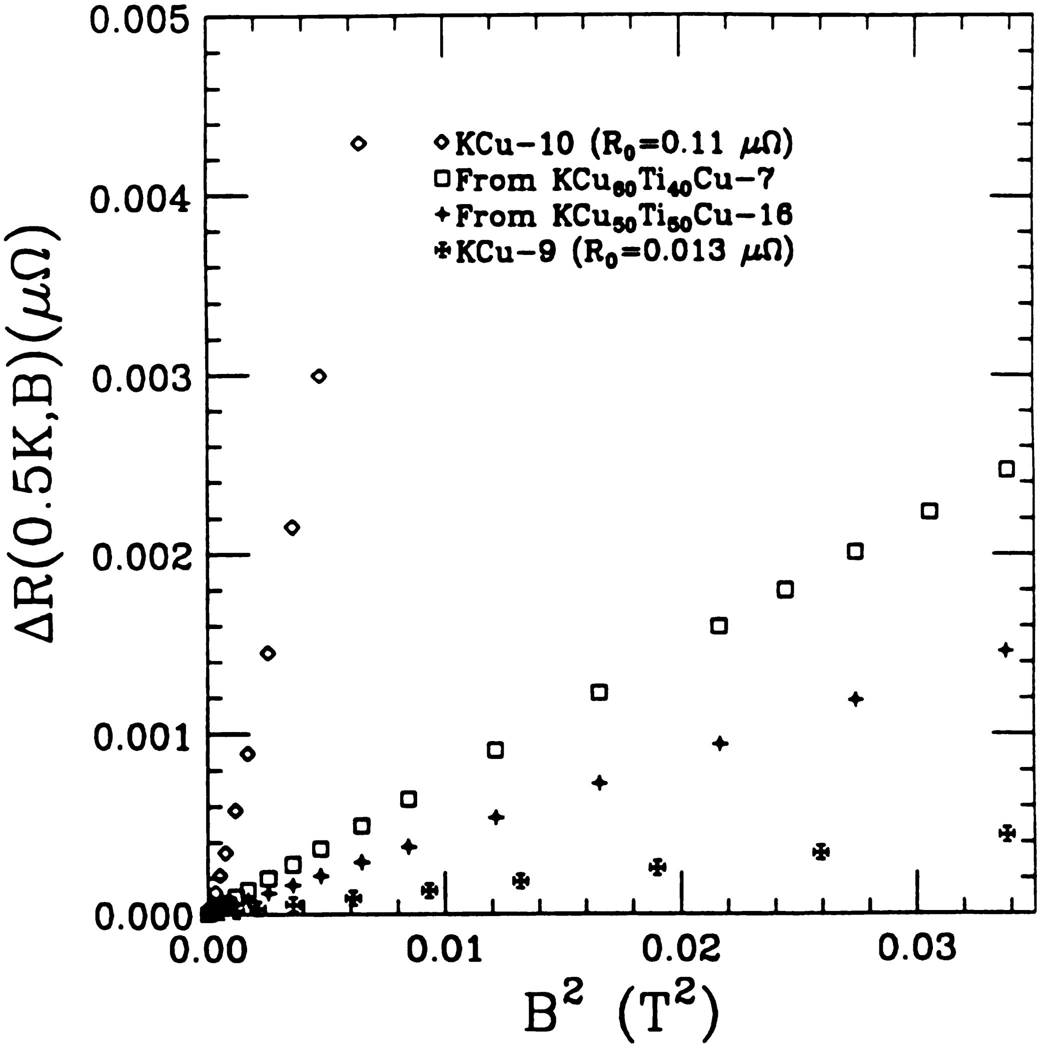

Figure 4.20: The background magnetoresistances due to K, Cu and the boundaries in the KCuTiCu sandwiches

4.4 Comparisons of the Fitting Parameters

For a comparison, the best fitting parameters obtained in the Section 4.2 and 4.3 are presented in Table 4.6. From the table, we see the following:

(1) Except for T_c, the parameters for $Cu_{50}Ti_{50}$ and $Cu_{60}Ti_{40}$ alloys are rather close either at zero or finite fields. The differences in T_c are due to the different Ti concentrations in these alloys.

(2) For the same alloy, p and $\tilde{F}_\sigma$ from both zero and finite magnetic field are about same, but τ_{io} and τ_{so} from the magnetoresistance measurements are about an order of magnitude larger than their zero field values. This is, perhaps, not very surprising because, at low temperatures, the zero field resistance and magnetoresistance are, respectively, dominated by the different scattering mechanisms—electron-electron interaction and weak localization. The big differences in T_c may be due to the suppression of the T_c at finite field. We are unable to fit magnetoresistance data for $T < 0.25$K if we use the values of T_c from the zero field fits.

Table 4.6: The Fitting Parameters from the Zero Field Resistances and Magnetoresistances

Samples	B (T)	T (K)	p	τ_{io} (psK^p)	τ_{so} (ps)	T_c (mK)	$\tilde{F}_\sigma$
$Cu_{50}Ti_{50}$	0.0	0.052−2.7	1.7−2.5	30−200	0.06−1.4	9−0.3	0−0.3
	0−0.15	0.02−4.0	1.6−1.8	680−750	13−20	5	0−0.2
$Cu_{60}Ti_{40}$	0	0.015−2.7	1.8−2.5	30−100	0.0−0.5	3−0.2	0−0.37
	0−0.15	0.02−4.2	1.6−1.8	870−950	7−15	0.1	0.0−0.3

The inelastic scattering time τ_i is one of the parameters which was not completely explained in the Table 4.6. Usually τ_i is temperature dependent, and its reciprocal is proportional to T^p. From the best fits to the magnetoresistances at each temperature in Figure 4.17 and 4.19, the values of τ_i are obtained and shown in Figure 4.21. The

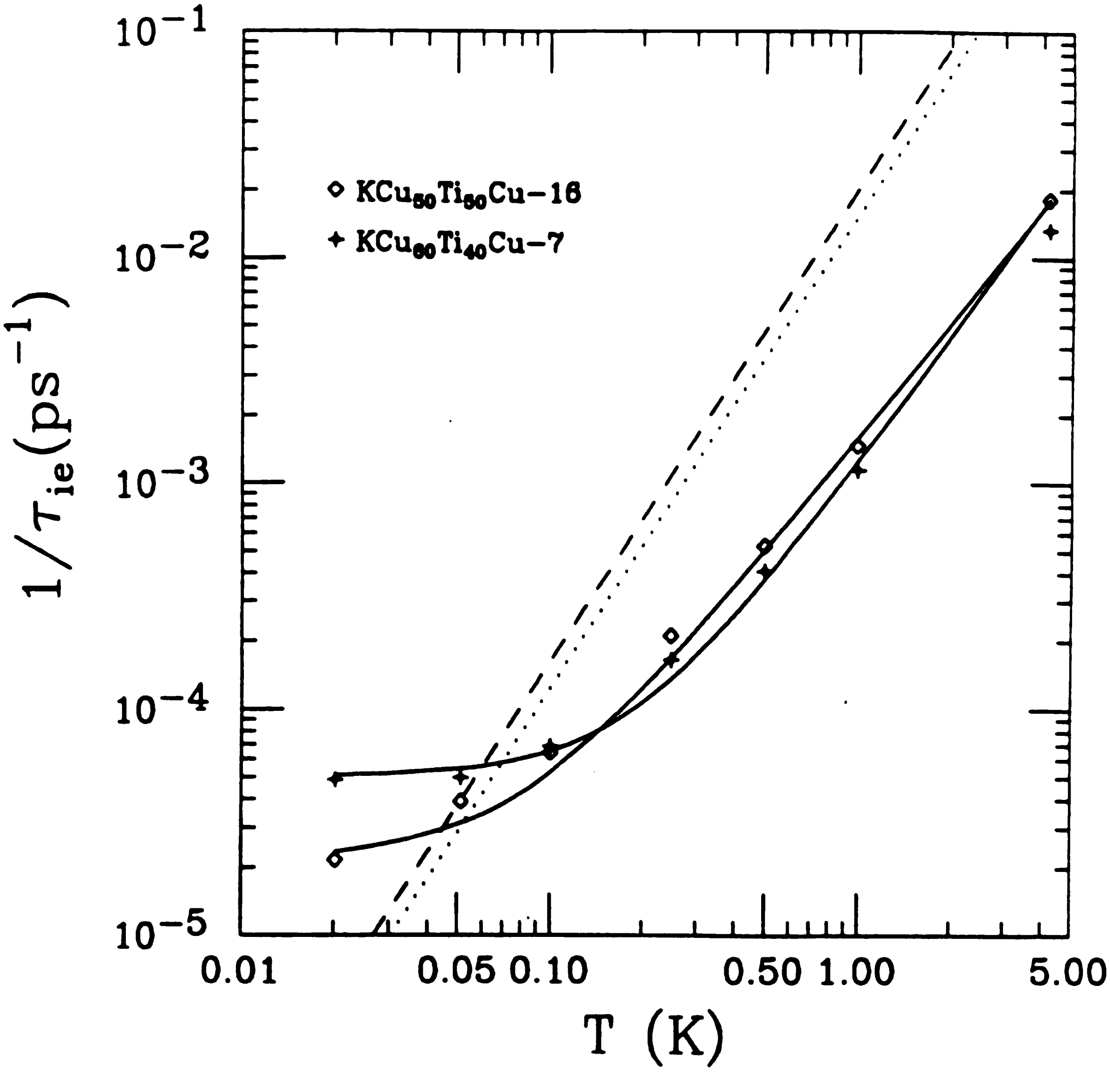

Figure 4.21: $1/\tau_i$ vs T for $Cu_{50}Ti_{50}$ and $Cu_{60}Ti_{40}$ alloys

data sets are from the magnetoresistance fits, and the solid curves are the best fits to the inelastic scattering times by

$$\frac{1}{\tau_i} = A + \frac{T^p}{\tau_{io}} \ , \tag{4.9}$$

which yield the parameters p and τ_{io} in the Table 4.6.

The dotted and dashed curves, respectively, are the corresponding τ_i values for $Cu_{50}Ti_{50}$ and $Cu_{60}Ti_{40}$ alloys from zero field resistance fits with p =2.1, and τ_{io} = 65psK^p and 50psK^p, which are mean values from Table 4.5. From the Figure, we see the following features:

(1) For $T > 0.1$K, τ_i at zero field is much smaller than at finite fields, and they cross over at about 50mK. No saturation was found in zero field for $T <$ 50mK.

(2) From the magnetoresistance measurements (symbols in Figure 4.21) and for $T > 0.1$K, τ_i for the $KCu_{50}Ti_{50}Cu$ sample are very close to those for the $KCu_{60}Ti_{40}Cu$ samples. However, for $T < 0.1$K, τ_i for the $Cu_{60}Ti_{40}$ alloy saturates while τ_i for $Cu_{50}Ti_{50}$ alloy continues to decrease and may saturate for $T <$ 20mK.

In the zero-field fits, saturation of τ_i was not considered. We will show that this is not really a problem in the zero-field fits. For $T >$ 100mK, τ_i in zero field is much smaller than its possible saturation value. Thus this possible saturation will make a negligible change in the weak localization contribution to ρ. For $T <$ 100mK, τ_i becomes comparable to its possible saturation value, but the total contribution to resistivity related to τ_i for $T <$ 100mK (weak localization) is much smaller than electron-electron interaction (see Figure 4.10). Therefore the possible saturation of τ_i in zero field will not make any appreciable contribution to resistivity.

Next we will address the question of the relative size of the sample thickness and the appropriate weak localization inelastic diffusion length L_i, which is

$$L_i = \sqrt{D\tau_i} \ . \tag{4.10}$$

In other words, are we correct in assuming that our ribbons are three dimensional for weak localization? To be correct, we require $L_i \ll d$ (size of a sample). From Figure 4.21, we know that the longest τ_i is about 5×10^4ps. using $D = 0.28\text{cm}^2/\text{s}$, we have $L_i = 2\mu\text{m}$, which is indeed much less than d ($> 20\mu\text{m}$).

Table 4.7: The Fitting Parameters for Comparisons

B_{max} (T)	Samples	T [1] (K)	p	τ_{io} (psK^p)	τ_{so} (ps)	T_c (mK)	$\tilde{F}_\sigma$	ref
0	$Cu_{50}Ti_{50}$	0.052–2.7	1.7–2.5	30–200	0.06–1.7	9–1.0	0–0.3	Our results
		1.7–20	2.78	16000	5.3		0.58	Schulte [a]
		0.1–30	2(F [2])	410	1.0		0.37	Hickey [b]
	$Cu_{60}Ti_{40}$	0.015–2.7	1.8–2.5	30–100	0.0–0.3	3–0.2	0–0.37	Our results
		1.7–20	2.99	11000	1.4		0.72	Schulte [a]
	$Cu_{65}Ti_{35}$	0.1–30	2(F [2])	190	0.18		0.45	Hickey [b]
		0.3–18	2.0–2.5		0.08–0.25		0–0.4	Lindqvist [c]
0.15	$Cu_{50}Ti_{50}$	0.02–4.0	1.6–1.8	680–750	13–20	5	0–0.2	Our results
6		4.2–20	3–4		4.4		0.37(F)	Howson [e]
0.15	$Cu_{60}Ti_{40}$	0.02–4.2	1.6–1.8	870–950	7–15	0.1	0.0–0.3	Our results
4		0.12–4.2			11		0.6	Lindqvist [d]
4	$Cu_{65}Ti_{35}$	0.045–9.2	2.0		5.5		0.4	Lindqvist [c]

[1] The fitting temperature range.
[2] The fixed parameters.
[a] from reference [Sch 86].
[b] from reference [Hic 86].
[c] from reference [Lin 88].
[d] from reference [Lin 89].
[e] from reference [How 86].

Finally we want to compare our parameters with those of other people. Table 4.7 lists the fitting parameters obtained by other researchers at both zero and finite fields. In theoretical expressions given in Chapter 2, the phase-breaking time τ_ϕ is commonly defined by

$$\frac{1}{\tau_\phi} = \frac{1}{\tau_i} + \frac{X}{\tau_{so}} \ , \tag{4.11}$$

where different researchers use different values of X: 4/3, 2, or 4. Unfortunately the τ_{so} value will depend upon the values of X. In our fitting, we used $X = 4$. For other

X values, the equivalent values of τ_{so} to that of $X = 4$ is given by

$$(\tau_{so})_{equ} = \frac{4}{X}(\tau_{so})_X \quad . \tag{4.12}$$

The values of τ_{so} from other people in the Table 4.7 have been converted to our equivalent values.

From the table, first we see that our data were taken down to about 15mK and the minimum temperatures for our fits are 52mK and 15mK, respectively, for the $Cu_{50}Ti_{50}$ and $Cu_{60}Ti_{40}$ alloys. These are the lowest-temperature and highest-precision measurements ever taken and fitted to so far. We found that both $Cu_{50}Ti_{50}$ and $Cu_{60}Ti_{40}$ alloys are superconductors, so we have also considered the effects of T_c on our fits which most people have neglected.

Second, at zero magnetic field, our parameters are consistent with Hickey *et al.* and Lindqvist *et al.*, whose data were taken and fitted at very low starting temperature. In fact, Lindqvist *et al* took their data down to about 20mK, but they just fitted their data above 0.3K probably because their data were saturated below 0.3K (as shown in Figure 4.9). The parameters of Schulte *et al.*, especially τ_{io} and τ_{so}, are different from the others. The p value of from Howson *et al* is much larger than those from others. The common feature is that their data were taken above 1.7K.

Third, the τ_{io} and τ_{so} parameters from finite fields are much bigger than those from the zero field. This may be due to an inconsistency in the theoretical formulas since at the lowest temperatures zero field resistance and magnetoresistance are dominated by the electron-electron interaction and weak localization, respectively.

Chapter 5

Summaries and Conclusions

In this study, we have investigated the electrical and magneto-resistances of $Cu_{50}Ti_{50}$ and $Cu_{60}Ti_{40}$ alloys at very low temperatures and magnetic fields. The zero field resistances have been measured from 15mK to 6K and magnetoresistance measurements were carried out in fields up to 0.2T at 20mK, 52mK, 0.1K, 0.25K, 0.5K, 1.0K and 4.2K.

To measure the resistances and temperatures more accurately and reliably than ever before, we have developed a novel method: measuring the electrical resistances of the CuTi ribbons with the current perpendicular to the ribbons and using K as a non-superconducting glue to achieve excellent electrical and thermal contact between the CuTi ribbons and refrigerator with its attached thermometers. Our temperature measurements, which can be quite difficult at such low temperatures, are reliable at least down to 15mK with an error much less than 1mK. Using a SQUID null detector and a high precision current comparator, we measured the resistances to a relative precision of about $10^{-7}-10^{-8}$. Even though this method causes some complications in analyzing the resistances due to background contributions by the Cu electrodes, and the K layers, and their boundaries, these problems have been overcome. In principle, our method is applicable to any ribbon or film-like high-resistivity sample.

We observed that resistances of the CuTi alloys decrease with increasing temperatures and that magnetoresistances increases with increasing magnetic fields. At zero magnetic field and for $T < 0.15$K, the electron-electron interaction contribution dominates the total resistance, while the weak localization contribution is significant for $T > 0.15$K. On the other hand, at a finite magnetic field and at the lowest temperatures, the magnetoresistances are dominated by weak localization, Zeeman splitting, and Maki-Thompson superconducting fluctuations. We found that both $Cu_{50}Ti_{50}$ and $Cu_{60}Ti_{40}$ alloys are superconductors with the transition temperatures of less 15mK and 5mK, respectively, which have never been quantified before.

The inelastic scattering time tends to saturate at $T < 0.1$K, especially for $Cu_{60}Ti_{40}$ alloys, which is possibly due to the presence of dilute magnetic impurities. We conclude that $p = 1.8 - 2.5$, where $\tau_i = \tau_{io}T^{-p}$, and $\tilde{F}_\sigma = 0 - 0.3$ for both $Cu_{50}Ti_{50}$ and $Cu_{60}Ti_{40}$ alloys. The lifetimes τ_{so} and τ_{io} that were obtained from the zero magnetic field measurements are about a order of magnitude smaller than those obtained from finite field measurements. The exact cause of the disagreement is not known, but one possibility is that the theories are incomplete in the strong spin-orbit scattering limit for zero and low fields and at very low temperatures.

Now that this novel technique has been perfected, a number future experiments come to mind.

(1) In principle, thermoelectric power measurements could be made that would provide a first test of existing theoretical predictions [Hsu 89].

(2) The transport properties of CuTi/crystalline-metal multilayers could be studied in which the layer thickness spans the important length scales for electron-electron interaction and weak localization, respectively: L_{th} and L_i (see Equation 2.13 and 4.10).

Appendix A

Calibration of χ_{old}

As discussed in Section 3.3, for $T < 50$mK, a CMN thermometer called χ_{old} was used to measure the temperatures of the sample. χ_{old} varies linearly with $1/T$ (Curie's law). However, its slope slightly changes with time. By comparing χ_{old} with two germanium resistors R_6 and R_7, which were at the same temperature, we could correct this change as described in Section 3.3.1. The values of χ_{old}, R_6, and R_7 were measured directly and are shown in Table A.1. The temperatures in the table are calculated from R_6 and R_7. Fitting the data with Curie's law, we obtained

Table A.1: χ_{old} vs T

R_6/R_7 (Ω)	T (K)	χ_{old}
1915	4.2010	0.0443
95.2	1.5190	0.0440
540	0.2765	0.0405
2530	0.1265	0.0356
9160	0.0786	0.0300
17500	0.0636	0.0266
50600	0.0465	0.0200

$$\chi_{old} = 0.04466 - \frac{0.001148}{T} \tag{A.1}$$

For $T < 50$mK, we use this equation to calculate the temperature from the measured χ_{old}. The error is estimated to be less than 0.5%.

Appendix B

Temperature Dependence of of the Reference Resistance

As discussed in Section 3.3.2, for $T > 0.4$K, the resistance of our reference resistor (R_{ref}) slowly increases with increasing temperature. This temperature dependence, even if is is very small in magnitude, may have a significant effect on apparent temperature dependence of the resistances of our samples. To correct this effect, we measured R_{ref} vs C_{11} (indicating the reference temperature) as shown in Table B.1 and plotted in Figure 3.7. Using the Equation 3.1, the data were fitted very well as shown in Figure 3.7. The fitting parameters are shown in the following equation:

$$R_{ref} = \left\{ \begin{array}{ll} 7.263017 \,, & C_{11} \leq 1.4 \\ 7.263001 + \frac{0.00013454}{(4.0162 - C_{11})^{2.2644}} \,, & C_{11} > 1.4 \end{array} \right\} , \tag{B.1}$$

where units of C_{11} and R_{ref} are mΩ^{-1} and $\mu\Omega$, respectively. Once C_{11} is measured, the value of R_{ref} can be corrected according the above formula.

Table B.1: R_{ref} vs C_{11}

C_{11} (mΩ^{-1})	R_{ref} ($\mu\Omega$)	$\sigma_{R_{ref}}$ ($\mu\Omega$)
1.0720	7.263016	0.000001
1.2123	7.263017	0.000001
1.4080	7.263018	0.000001
1.6040	7.263020	0.000001
1.8030	7.263022	0.000001
1.9030	7.263023	0.000002
2.0080	7.263026	0.000001
2.1330	7.263030	0.000002
2.2050	7.263033	0.000001
2.3130	7.263038	0.000002
2.4150	7.263044	0.000002
2.5270	7.263052	0.000002
2.6360	7.263064	0.000002
2.7620	7.263082	0.000002
2.8720	7.263102	0.000002
2.9490	7.263121	0.000002
2.9700	7.263126	0.000005
3.0990	7.263173	0.000005
3.2000	7.263222	0.000005
3.2850	7.263283	0.000005
3.3550	7.263351	0.000005
3.4130	7.263430	0.000005
3.4510	7.263498	0.000007
3.4900	7.263584	0.000007
3.5250	7.263677	0.000007
3.5480	7.263753	0.000007
3.5690	7.263832	0.000004
3.5800	7.263882	0.000004
3.6085	7.264024	0.000004
3.6270	7.264140	0.000004
3.6540	7.264336	0.000004
3.6720	7.264507	0.000004
3.6910	7.264712	0.000004
3.7035	7.264873	0.000005
3.7175	7.265081	0.000005
3.7290	7.265270	0.000005
3.7385	7.265453	0.000005

Bibliography

[Abr 79] E Abrhams, P. W. Anderson, D. C. Licciardello, and T. V. Ramakrishnan, Phys. Rev. Lett. **42**, (1979)673

[Alt 81] B. L. Altshuler, A. G. Aronov, A. G. Larkin, and D. E. Khmel'nitski, Sov. Phys. JETP **54**, (1981)411

[Alt 85] B. L. Altshuler and A. G. Aronov, Electron-electron Interaction in Disordered Systems, Efros, A. L. Pollak, M. (eds). Amsterdam: North-Holland (1985)p1

[And 58] P. W. Anderson, Phys. Rev. **109**, (1958)1492

[Asl 68] L. G. Aslamazov and A. I. Larkin, Phy. Lett. **26A**, (1968)238

[Bax 89] D. V. Baxter, R. Richter, M. L. Trudeau, R. W. Cochrane, and J. O. Strom-Olsen, J. Phys. France **50**, (1989)1673

[Ber 69] G. Bergmann, Z. Phy **225**, (1969)430

[Ber 82] G. Bergamann. Solid State Communication **42**, (1982)815

[Ber 83] G. Bergmann, Phy. Rev. B **28**, (1983)2914

[Ber 84] G. Bergmann, Phys. Rep. **107**, (1984)1

[Ber 87] G. Bergmann, Phy. Rev. B **35**, (1987)4205

[Bla 68] F. J. Blatt, Physics of Electronic Conduction in Solids, (1968) [Dug 77] J. S. Dugdale, Electrical Properties of Metals and Alloys, (1977)

[Dug 87] J. S. Dugdale, Contemp. Phys. **28**, (1987)547

[Edm 80] D. Edmunds, W.pratt Jr. and J. A. Rowlands, Rev. Sci. Inst. **51**, (1980)1516

[Fuk 81] H. Fukuyama and K. Hoshino, J. of Phy. Soc. of Japan **50**, (1981)2131

[Fuk 85] H. Fukuyama, Electron-electron Interaction in Disordered Systems, Efros, A. L. Pollak, M. (eds). Amsterdam: North-Holland (1985)p155

[Hae 83] M. L. Haerle, Ph.D. Thesis, Michigan State University, (1983)

[Hei 83] V. O. Heinen, Ph.D. Thesis, Michigan State University, (1983)

[Hic 86] B. J. Hickey, D. Greig, and M. A. Howson, J. Phys. F: Met. Phys. **16**, (1986)L13

[Hic 87] B. J. Hickey, D. Greig, and M. A. Howson, Phy. Rev. B **36**, (1987)3074

[Hik 80] S. Hikame, A. I. Larkin, and Y. Nagaoka, Prog. Theor. Phys. **63**, (1980)707

[How 86] M. A. Howson and D. Greig, J. Phy. F **16**, (1986)989

[How 88] M. A. Howson and B. L. Gallagher, Phys. Rep. **170**, (1988)265

[Hsu 89] J. W. P. Hsu, A. Kapitulnik, and M. Yu. Reizer, Phys. Rev. B **40**, (1989)7513

[Ime 74] J. Imes, Ph.D thesis, Michigan state University, (1974)

[Ime 75] J. Imes, G.Neiseihel and W.Pratt Jr., J. of Low Temp. Phys. **21**, (1975)1

[Imi] Imperial Metal Industries, P.O. box 216, Witton Birmingham, B6 7ba, England

[Joh 78] W. L. Johnson, C. C. Tsuei, and P. Chaudhari, Phy. Rev. B **17**, (1978)2884

[Kaw 80a] A. Kawabada, Solid State Communication **34**, (1980)431

[Kaw 80b] A. Kawabada, J. Phys. Soc. Japan **49**, (1980)628

[Kaw 81] A. Kawabada, J. Phys. Soc. Japan **50**, (1981)2461

[Kon 64] J. Kondo, Prog. Theor. Phys. **32**, (1964)37

[Lar 80] A. I. Larkin, JETP Lett. **31**, (1980)219

[Lee 82] P. A. Lee and T. V. Ramakrishnan, Phys. Rev. B **26**, (1982)4009

[Lin 88] P. Lindqvist and Ö. Rapp, J. Phy. F **18**, (1988)1979

[Lin 89] P. Lindqvist and G. Fritsch, Phys. Rev. B **40**, (1989)5792

[Lin 90] P. Lindqvist, Ö. Rapp, A. Sahnoune, and J. O. Ström-Olsen, Phys. Rev. B **41**, (1990)3841

[Lou 74] O. Lounasmaa, Experimental Principles and Methods below 1K. Academic Press, Inc., New York (1974)

[Mac 68] W. L. MacMillan, Phys. Rev. **167**, (1968)331

[Mae 81] S. Maekawa and H. Fukuyama. J. Phys. Soc. Japan **50**, (1981)2516

[Mak 68a] K. Maki, Prog. Theor. Phys. **39**, (1968)897

[Mak 68b] K. Maki, Prog. Theor. Phys. **40**, (1968)193

[Mcl 84] W. L. Mclean and T. Tsuzuki, Phy. Rev. B **29**, (1984)503

[Miz 83] U. Mizutani, N. Akutsu and T. Mizoguchi, J. Phys. F: Metal Phys. **13**, (1983)2127

[Moo 84] D. E. Moody and T. K. Ng, Proc. 17th Int. Conf. on Low Temperature Physics, (1984)371

[Mot 89] A. C. Mota, P. Visani, and A. Pollini, J. Low Temp. Phys. **76**, (1989)465

[Ous 85] J. C. Ousset, S. A. Askenazy, H. Rakoto and J. M. Broto, J. Physique **46**, (1985)2145

[Pat 74] B. R. Patton, Proceeding of 13th International Confer. on Low Temp. Phys., Boulder, 172 (Plenum, New York, 1974) Vol. III.

[Pip 89] A. B. Pippard, Magnetoresistance in Metals, (1989)

[Ric 88] R. Richter, D. V. Baxter, and J. O. Strom-olsen, Phy. Rev. B **38**, (1988)10421

[Ros 65] H. M. Rosenberg, Low Temerature Solid State Physics, (1965)

[Sam 89] A. Sahnoune and J. O. Ström-Olsen, Phys. Rev. B **39**, (1989)7561

[Sam 82] K. Samwer and H. V. Löhneysen, Phys. Rev. B **26**, (1982)107

[San 85] J. M. B. Lopes dos Santos and E. Abrahams, Phy. Rev. B **31**, (1985)172

[Sch 86] A. Schulte and G. Fritch, J. Phy. F **16**, (1986)L55

[Sch 90] A. Schulte and G. Fritch, and E. Lüscher, Z. Phys. B–Condensed Matter **78**, (1990)457

[Sko 75] W. J. Skocpol and M. Tinkham, Rep. Prog. Phys. **38**, (1975)1049

[Ste 81] S. D. Steenwyk, J. A. Rowland, and P. A. Schroeder, J. Phys. F: Metal Phys. **11**, (1981)1623

[Tho 70] R. S. Thompson, Phys. Rev. B **1**, (1970)327

[Toy 84] N. Toyota, A. Inoue, K. Matsuzaki, T. Fukase, and T. Masumoto, J. Phys. Soc. Japan **53**, (1984)924

[Usa 69] K. D. Usadel, Z. Phy. **227**, (1969)260

[Yin 87] Shi Yin, Ph.D. Thesis, Michigan State University, (1987)

[Zim 60] J. M. Ziman, Electrons and Phonons, (1960)